

Faculty of Science and Engineering

**The Synthesis and Evaluation of Novel Core-Shell
Nanostructured Metal Oxides for Cancer Targeting**

Kunal Kamleshkumar Patel

**This thesis is presented for the Degree of
Doctor of Philosophy
of
Curtin University**

December 2016

DECLARATION

To the best of my knowledge and belief this thesis contains no material previously published by any other person except where due acknowledgment has been made.

This thesis contains no material which has been accepted for the award of any other degree or diploma in any university.

A handwritten signature in black ink, appearing to read 'Kunal Patel', written in a cursive style.

Kunal Patel

December 14th 2016

ABSTRACT

This thesis reports on the synthesis and characterisation of novel, nanocomposite architectures and elucidates their potential for applications in the target-specific treatment of cancer. A core-shell approach was utilised for the design of the nanoparticles (NPs), where the shell was outfitted to provide stability, biocompatibility and cell specificity and the core provided the therapeutic entity.

A hollow silica shell was first developed and its ability to function as a delivery system for small molecule drugs was investigated. Zinc oxide (ZnO) template NPs with controllable size were prepared via hydrolysis reaction and condensation of an alkoxy silane allowed coating of these templates with a silica shell. The shell was further modified to incorporate surface bound folic acid (FA) targeting ligands, tasked to provide cell specificity. To incorporate a therapeutic agent within the core, the ZnO templates were removed via acid leaching, leaving a cavity for the inclusion of small molecule therapeutic agents. The size, size distribution and morphology of the resulting NP system was characterised using dynamic light scattering as well as scanning and transmission electron microscopy. Various spectroscopic techniques such as Fourier transform infra-red, UV-visible absorption, fluorescence and nuclear magnetic resonance were used to confirm successful surface functionalisation. Thermogravimetric analysis allowed quantification of the surface bound FA. This physiochemical characterisation scheme was used as a staple in future NP analysis.

The ability of the hollow silica shell to function as a drug carrier was scrutinised using doxorubicin hydrochloride (DOX) as a model drug. Drug loading and release kinetics revealed discharge of DOX via a Fickian diffusion mechanism. The effectiveness of the system as a viable, functioning, targeted drug delivery agent was evaluated through in vitro cell cytotoxicity studies using mouse embryonic fibroblast (3T3) cells and human epithelial

colorectal adenocarcinoma (Caco-2) cells. The hollow shells displayed a toxic response, specific to the Caco-2 cell line even without the conjugated FA cell targeting ligand. The inclusion of FA enhanced cell specificity, but was also found to increase the viability of both cell lines. Encapsulation of DOX saw enhanced cell specific toxicity towards Caco-2 when compared to the free drug alone.

The developed silica shell system was then applied to a photoactive iron oxide-zinc oxide ($\text{Fe}_3\text{O}_4\text{-ZnO}$) core, with investigations focussing on the system's ability to function as a novel photosensitiser for use in photodynamic therapy (PDT). Based on our previously published work, the ZnO core NPs were modified via hybridisation with iron oxide to form a heterogeneous semiconductor material; the photoactive core now acting as the therapeutic entity in the core-shell NP system. As before, a silica shell, decorated with FA ligands was employed and the core-shell NP system was subjected to the developed characterisation scheme.

While surface modification of the $\text{Fe}_3\text{O}_4\text{-ZnO}$ core did mitigate its photophysical properties, the novel core-shell system still outperformed a pure ZnO analogue in photodegradation studies using methylene blue (MB) as a model organic compound. In vitro cytotoxicity studies with Caco-2 cells showed a time and dose dependant toxicity in the absence of UV-radiation. The UV-irradiated NPs demonstrated a significant photokilling effect with a drastic reduction in caco-2 cell viability. FA conjugation served to enhance the photokilling effect.

The versatility of the developed synthetic method was highlighted through further surface modification of the silica coated hybrid $\text{Fe}_3\text{O}_4\text{-ZnO}$ core-shell NPs. Polyethylene glycol (PEG), with and without terminal FA groups, was conjugated to the surface of the silica shell in varying quantities, to impart steric stability and stealth properties. Furthermore, to illustrate that the developed NP system could function in applications for imaging and image enhancement for possible diagnostic applications, dansyl chloride, a fluorescent molecule, was also attached to the NP surfaces, both with and without a PEG spacer. Characterisation of the synthetic products was once again carried out using the established scheme to confirm successful chemical modification. Fluorescence microscopy highlighted the capability of the dansylated NPs as a functioning fluorescent marker, while photodegradation using MB under various pH conditions demonstrated the continuing photoefficiency of the core-shell system.

Importantly, the methodology and results presented herein should provide practitioners of cancer therapeutic research an additional understanding of NP design as well as a synthetic scheme for the surface modification of metal oxide nanostructures, facilitating their transition towards biological applications, focussing particularly on targeted cancer treatment.

ACKNOWLEDGEMENTS

Over the years of my PhD candidature I have been privileged to have had the guidance and support of many colleagues, friends and family members. Whilst I shall try my best to acknowledge all of these people for their assistance, I apologise sincerely for any omissions I may have made. Nonetheless, all of your efforts have been most welcome and greatly appreciated.

First I would like to thank the Australian Government for providing me with an Australian Postgraduate Award. Curtin University, and the department of chemical engineering are also acknowledged, not only for providing me with a top up scholarship and a chemical engineering interim scholarship respectively, but for providing me with the support and facilities to carry out my research. The department of chemistry is also acknowledged for providing me with the laboratory and office space where most of my work was carried out.

I am sincerely grateful towards my project supervisor Professor Xia Lou for the countless hours she has spent in guiding, supporting and motivating me. Xia has had the difficult task of keeping me focussed, but has worked tirelessly to ensure my years of doctoral candidature have come to fruition. Her wealth of knowledge has been invaluable and has provided me with a solid base upon which I can grow my career. Xia's passion for research and unbelievably diligent work ethic are qualities I can only aspire towards.

Whilst there have been many people that have provided me with scientific and technical advice over the years for which I am grateful, I would like to thank Xiaohui Feng in particular. Her assistance with laboratory work as well as her company and friendship made things seem a great deal easier. I would also like to thank Behin Sundara Raj for

Acknowledgements

conducting all of the cell culture and cytotoxicity experiments used in this thesis. Behin's efficiency in the lab was unparalleled and it was a pleasure working with him.

To my friends in "The D", I could not possibly forget to thank each and every one of you for the many antics and great times we've shared. You have all provided me with great respite from the stress of research when I've needed it the most.

It is difficult to describe just how much help and support my partner, Nicole, has provided me with during the last few years. Although she may not realise it, she has carried me through the most difficult times of my life. The many sacrifices Nicole has made for me over the time we have shared together are not forgotten and I shall remain forever grateful. I will always be appreciative for her continued support and ineffable love.

I would like to thank my sister Keshal, and my dear grandmother, Ba, for always believing in me. You have both helped shape me to become the person I am and I consider myself privileged to have learnt all that I have from you both.

Finally, with all my heart I would like to thank my parents, Kamlesh and Usha. They have both done everything in their power to provide us with the means to flourish, not only academically, but in life. We have most certainly been showered with all of the love and support we could have ever asked for and more. I truly hope that I have done my best to make them proud.

Kunal Patel

December 2016

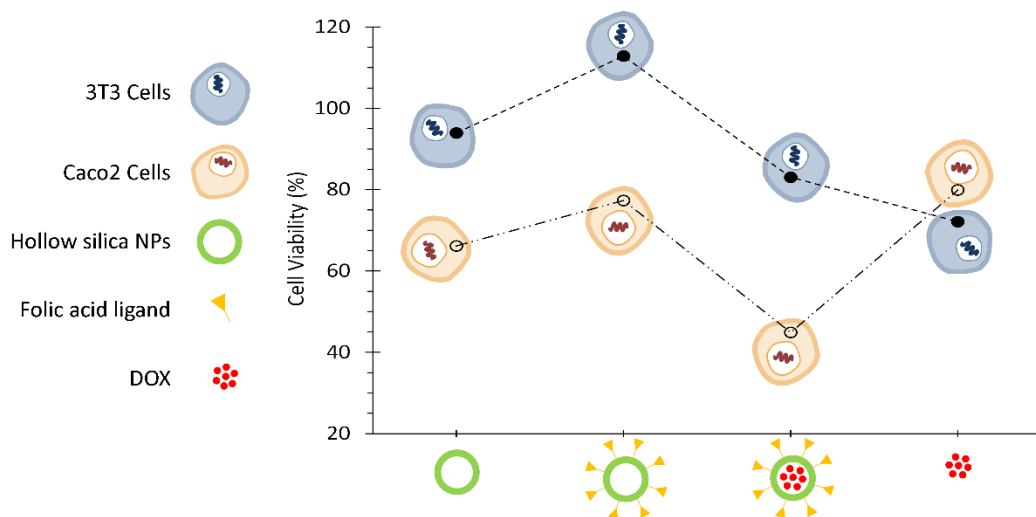
PUBLICATIONS

Primary Publications

Chapter 2

Patel, K., Sundara Raj, B., Chen, Y., & Lou, X. (2016). Cytotoxicity of folic acid conjugated hollow silica nanoparticles toward Caco2 and 3T3 cells, with and without encapsulated DOX. *Colloids and Surfaces B: Biointerfaces*, 140, 213-222. doi: <http://dx.doi.org/10.1016/j.colsurfb.2015.12.046>.

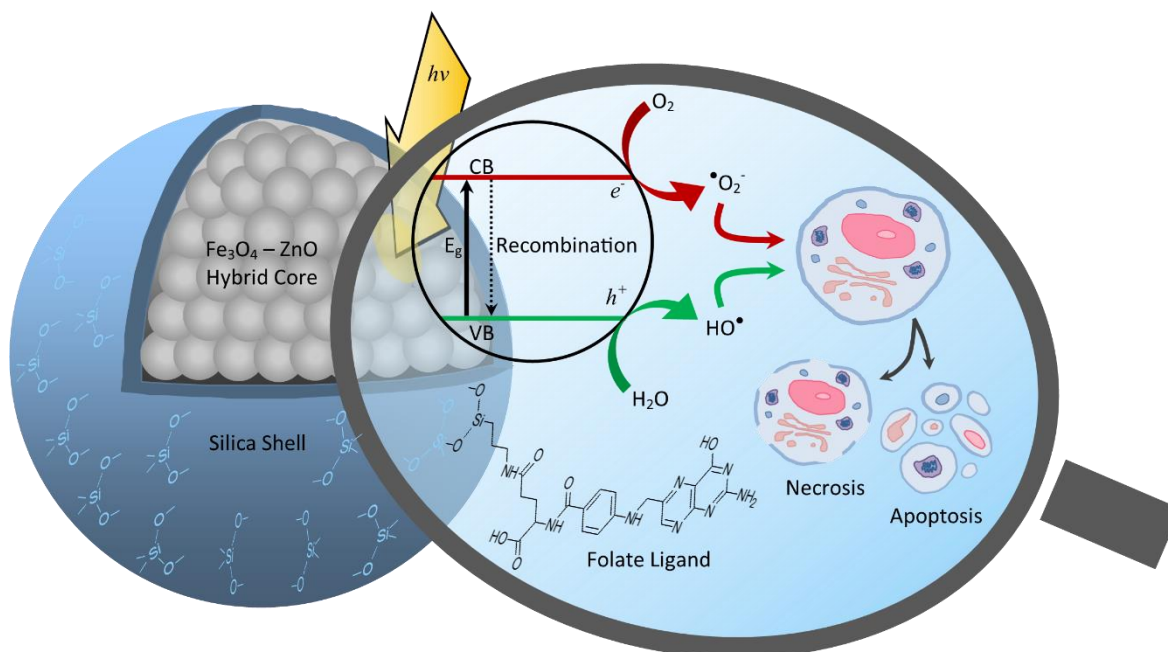
Graphical abstract



Chapter 3

Patel, K., Raj, B. S., Chen, Y., & Lou, X. (2016). Novel folic acid conjugated Fe₃O₄-ZnO hybrid nanoparticles for targeted photodynamic therapy. *Colloids and Surfaces B: Biointerfaces*. doi: <http://dx.doi.org/10.1016/j.colsurfb.2016.10.045>

Graphical abstract



Secondary Publications

Feng, X., Guo, H., Patel, K., Zhou, H., & Lou, X. (2014). High performance, recoverable Fe₃O₄-ZnO nanoparticles for enhanced photocatalytic degradation of phenol. *Chemical Engineering Journal*, 244(0), 327-334. doi: <http://dx.doi.org/10.1016/j.cej.2014.01.075>

Manuscripts in Preparation

Chapter 4

Patel, K., Lou, X. (2017). A multimodal photosensitizer prepared via surface modification of hybrid Fe₃O₄-ZnO nanoparticles

CONTRIBUTIONS

The research and work conducted in this thesis was primarily designed, executed, interpreted and written by the author, with guidance from Professor Xia Lou, the thesis supervisor. Cell culture and cytotoxicity experimental work carried out in Chapters 2 and 3 was conducted by Behin Sundara Raj.

TABLE OF CONTENTS

Title Page	i
Declaration	iii
Abstract	v
Acknowledgements	ix
Publications	xi
Contributions	xiii
Table of Contents	xv
List of Figures	xix

Chapter 1

1 Introduction and overview	1
1.1 Background	1
1.2 Nanoparticles for cancer theragnostics	5
1.2.1 Distinguishing features of nanoparticles for cancer therapy	7
1.2.1.1 Nanoparticle size	7
1.2.1.2 Nanoparticle shape.....	8
1.2.1.3 Controllable biodistribution	9
1.2.1.4 Cell specificity	10
1.2.2 Core-shell nanoparticles	11
1.3 Thesis overview	13
1.3.1 Aims and objectives	13

1.3.2 Research methodology	14
1.3.3 Expected outcomes and significance	17
1.4 References	18
Chapter 2	
2 Drug release characteristics and selective cytotoxicity of hollow silica nanoparticles.	23
2.1 Introduction.....	23
2.2 Materials and Methods	26
2.2.1 Materials	26
2.2.2 Synthesis of ZnO template and hS NPs.....	26
2.2.3 Synthesis of hSFA NPs	28
2.2.4 Nanoparticle Characterisation	29
2.2.5 Drug loading and Release	29
2.2.6 Cell Culture.....	30
2.2.7 Cell Viability.....	30
2.2.8 Statistical Analysis.....	31
2.3 Results and Discussion	31
2.3.1 Characterisation of NHS-FA	31
2.3.2 Characterisation of synthesised NPs.....	34
2.3.3 Drug loading and release studies.....	39
2.3.4 Cell viability study	40
2.4 Conclusions.....	43
2.5 References	44

Chapter 3

3 Novel, folic acid conjugated, Fe₃O₄-ZnO hybrid nanoparticles for cancer targeted

photodynamic therapy	47
3.1 Introduction	47
3.2 Materials and Methods	50
3.2.1 Materials.....	50
3.2.2 Chemical Synthesis.....	50
3.2.3 Nanoparticle characterisation.....	52
3.2.4 Adsorption and photoreactivity study.....	53
3.2.5 Cell culture and MTT cell viability assay.....	54
3.2.6 Photokilling effect.....	54
3.2.7 Statistical analysis.....	55
3.3 Results and Discussion	55
3.3.1 Nanoparticle synthesis and characterisation.....	55
3.3.2 Adsorption and photocatalytic properties of FZ, FZ-S and FZ-S-FA NPs.....	60
3.3.3 Effect of pH on adsorption and photodegradation.....	62
3.3.4 Cell toxicity and photokilling effect.....	64
3.4 Conclusion	67
3.5 References	67

Chapter 4

4 Surface modification of Fe₃O₄-ZnO hybrid nanoparticles to produce a multimodal

photosensitiser	71
4.1 Introduction	71
4.2 Materials and methods	74
4.2.1 Materials.....	74
4.2.2 Chemical synthesis.....	74

Table of Contents

4.2.2.1 Synthesis of core-shell hybrid FZ-S NH ₂ 50 and FZ-S-GPS NPs	74
4.2.2.2 Synthesis of FZ-S DnS50 NPs	75
4.2.2.3 Synthesis of FZ-S PEG and FZ-S-PEG-DnS NPs.....	75
4.2.2.4 Synthesis of FZ-S PEG-FA NPs	75
4.2.3 Nanoparticle characterisation	79
4.2.4 Adsorption and photoreactivity study	80
4.3 Results and discussion.....	80
4.3.1 Synthesis and characterisation of FZ-S-PEG, FZ-S-PEG-FA and FZ-S-PEG-DnS	80
4.3.2 Adsorption and photodegradation of MB	87
4.5 Conclusion	92
4.6 References	93
Chapter 5	
5 Conclusions and future considerations	97
Bibliography	100
Appendix 1	119
Reproducibility of photodegradation experiments	119
Appendix 2	121
Copyright agreement for Figure 1-1 in Chapter 1.....	122
Copyright agreement for Chapter 2.....	123
Copyright agreement for Chapter 3.....	124

LIST OF FIGURES

Chapter 1

- Figure 1-1. Illustrates passive targeting of NPs to tumours through the EPR effect. NPs preferentially accumulate within the tumour interstitium through poorly constructed vessels containing large fenestrae and impaired lymphatic drainage. Post-extravasation, intracellular uptake of ligand functionalised NPs can be facilitated through receptor mediated endocytosis.6
- Figure 1-2. A flow chart detailing the research methodology employed in this dissertation.15
- Figure 1-3. A schematic diagram detailing the photocatalytic reaction apparatus16

Chapter 2

- Figure 2-1. A schematic illustration of the synthetic process used to fabricate hollow silica (hS) and folic acid conjugated hollow silica (hSFA) NPs.27
- Figure 2-2. (a) FTIR and (b) ¹H NMR spectra, both detailing the activation of FA to NHS-FA. The γ isomer of NHS-FA is shown in (b).33
- Figure 2-3. (a) SEM micrographs of Z(215) (left), Z(430) (centre), ZSFA(430) (right) and (b) TEM micrographs of hSFA(215) (left) and hSFA(430) (right).35
- Figure 2-4. (a) FTIR spectra, (b) TGA curves (left) and UV-Vis spectra (right) for various NPs.38
- Figure 2-5. (a) Release profiles of DOX, and (b) the corresponding linear fitting using Equation 2-1.39
- Figure 2-6. Viability of 3T3 and Caco-2 cells at $t = 6$ h and $t = 24$ h. All data are represented as mean \pm SEM with $n = 3$. Inserts in (c) and (d) show concentration

dependence of cell viability for hS(215) and hS(430) NPs. * and ● denote $P < 0.05$	41
Figure 2-7. (a) Viability of 3T3 and Caco-2 cells at $t = 24$ h upon treatment with hS(215) at various concentrations. (b) The influence of free and encapsulated DOX ($0.5 \mu\text{g.mL}^{-1}$) on 3T3 and Caco-2 cell viability at $t = 24$ h. NP concentration was $50 \mu\text{g.mL}^{-1}$. All data are represented as mean \pm SEM with $n = 3$. Note: dotted lines are used for visual emphasis of cell specificity and do not signify any correlation between NPs.	42
Chapter 3	
Figure 3-1. Synthetic scheme outlining preparation of FZ-S and FS-SFA NPs.	51
Figure 3-2. TEM micrographs of (a) FZ and b) FZ-SFA NPS. Black arrows in (b) indicate the silica layer.	56
Figure 3-3. XRD diffraction patterns for Fe_3O_4 (a), FZ (b) and Zn (c) NPs.	56
Figure 3-4. FTIR spectra (a, left), UV-Vis DRS spectra (a, right), TGA curves (b, left), fluorescence emission spectra using an excitation wavelength of 277 nm (b, centre) and 283 nm (b, right).	58
Figure 3-5. Change in MB concentration over time for adsorption (left) and photodegradation (centre) studies at pH 7.4. The linear fit as per Eq. 2 of the first 90 min of degradation data is shown on the right.	62
Figure 3-6. Effect of pH on adsorption (a) and photodegradation (b) of MB. Open circles designate the zeta potential of the corresponding samples, at the given pH.	63
Figure 3-7. Viability of Caco-2 cells upon exposure to various NPs for 6 h (left) and 24 h (centre) at various concentrations. Photo-induced reduction in Caco-2 cell viability is shown on the right, where shaded portions of the columns represent the level to which cell viability was reduced after exposure to UV radiation.	64
Chapter 4	
Figure 4-1. An illustration of the brush and mushroom conformations of PEG chains	72
Figure 4-2. Synthetic scheme detailing the preparation of (a) dansylated hybrid NPs FZ-S-DnS, (b) PEGylation to produce FZ-S-PEG and subsequently (c) FZ-S-PEG-DnS and (d) FZ-S-PEG-FA.	77

Figure 4-3. TEM micrographs (above) and DLS size distributions (below) of (a) FZ, (b) FZ-S-FA and (c) FZ-S-PEG-FA nanoparticles. Where (d) is a lower magnification TEM micrograph of FZ-S-PEG-FA NPs.	81
Figure 4-4. FTIR spectra detailing (a) GPS functionalisation, PEGylation and conjugation of FA and the dansyl fluorophore to include the PEG spacer. (b) amination and dansylation without a PEG spacer and (c) free FA, DnCl and PEG molecules used in the synthesis.	82
Figure 4-5. Mass loss percentage curves for (a) FZ-S-PEG-FA25 and (b) FZ-S-DnS and their constituent NPs as obtained via thermogravimetric analysis.	84
Figure 4-6. Fluorescence emission spectra using an excitation wavelength of (a) 327 nm and (b) 277 nm. The chemical scheme inserts in a) represent variations in electronic charge transfer resulting from changes in bond type and are colour coded to match respective spectra.	85
Figure 4-7. Fluorescence micrographs of FZ-S-PEG-DnS NPs at (a) 25 $\mu\text{g.mL}^{-1}$ and (b) 100 $\mu\text{g.mL}^{-1}$. With (c) FZ-S-PEG at 100 $\mu\text{g.mL}^{-1}$. A magnification of 240x was used for all images.	86
Figure 4-8. Effect of PEG on adsorption (a) and photodegradation (b) of MB. Open circles designate the zeta potential of the corresponding samples, at the given pH, in the absence of MB.	87
Figure 4-9. Effect of dansylation on adsorption (a) and photodegradation (b) of MB. Open circles designate the zeta potential of the corresponding samples, at the given pH, in the absence of MB.	90
Figure 4-10. ICP-OES analysis of (a) zinc content and (b) iron content at pH 9.3 over the adsorption (dark) and photodegradation periods.	91

Appendix 1

Figure A1-1 Photodegradation experimental trials highlighting the reproducibility of the employed method. Experiments were conducted 3 times with a MB concentration of 10 mg.L^{-1} and a FZ NP concentration of 0.00 mg.L^{-1} (Left) and 325 mg.L^{-1} (right).	119
--	-----

CHAPTER 1

1 Introduction and overview

1.1 Background

After more than twenty years of rapid advances, an abundant and multifaceted knowledge base has been engendered through cancer research. The disease has thus been revealed to be multifarious, comprising dynamic changes in the genome that have added complexity and difficulty in its treatment. As such, the morbidity and mortality associated with the disease are of definite concern on a global level. The most current cancer statistics according to the World Health Organisation showed that in 2012 alone, 14.1 million new cases of cancer were accrued worldwide, with the disease accounting for 8.2 million deaths; a staggering thirteen percent of all deaths [1]. The most recent data from the Australian Institute of Health and Welfare suggested that in the same year an estimated 120,000 Australians were treated for the disease with 43,039 deaths, accounting for about 30% of total deaths in the country. The disease resulted in an economic burden in Australia of approximately \$4.7 billion in 2012. The number of new cancer cases diagnosed in Australia in 2016 was estimated to increase to 130,466 with 46,880 deaths predicted (2016 estimations are based on extrapolations from 2002-2011 data)[2]. In light of these

figures, the development of novel therapeutic and diagnostic materials and strategies for their implementation has become a significant part of cancer research.

Excluding the confines of clinical trials, the mainstay of cancer treatment over the past two decades has largely rested on surgery, radiation therapy and systemic treatment with chemotherapeutics, small molecules and hormone therapy [3]. The modality of conventional treatment is based largely on the type of cancer, the developmental stage of the disease and a variety of personal conditions inherent to the patient. These factors are such that treatment of the disease is highly personalised, and can vary considerably from patient to patient.

From the first oncologic surgery in 1809 for the removal of an ovarian tumour [4], through to more recent emerging robotics and natural orifice transluminal endoscopy surgery in colorectal cancer, surgery has become a key component of cancer treatment, whether it is used for prevention, diagnosis, staging, curative therapy or palliation [3]. Over 60% of all cancers are treated with some form of surgery and this modality is used in approximately 90% of cases from a diagnosis and staging perspective [5]. Curative surgery is normally undertaken only when the malignancy is localised and can be removed in completion, such as with melanoma in its primary stages [6]. The need for removal of healthy tissue surrounding diseased tissue to ensure an adequate margin for successful resection is a disadvantage of cancer surgery. Furthermore, patients are required to have exceptional cardiac and pulmonary performance to undergo anaesthesia for major surgical procedures. Notably, the postoperative risk of tumour recurrence remains high and in many cases combination and or alternative therapies are required for further treatment [7].

Almost 66% of cancer patients undergo radiation therapy during the course of their disease treatment, this form of therapy, along with surgery is considered a primary treatment mode for cancer patients [8]. Essentially two types of ionising radiation therapy can be administered; either electromagnetic radiation such as x-rays or photons or that which produces particulate radiation such as alpha or beta particles, electrons, protons and neutrons [8]. Irrespective of the source, the radiation induces a cellular response in one of two ways; directly or indirectly. Direct cellular responses occur through the damage of DNA molecules within the nucleus of cells resulting in impaired function and eventually cell death [9]. Indirect cellular

responses occur through interaction of radiation with the media surrounding the molecular structures within the cell (primarily intracellular water). Radiation absorbed by water molecules results in the formation of free radicals that in turn are believed to generate reactive oxygen species (ROS) causing toxicity to the cell [8, 9]. As with surgery, radiation therapy can be used in a curative, through to palliative form of treatment and is often used in combination with other treatment modalities. Despite commonality in its use, radiation toxicities in many tissues including skin, lung and brain have been described [10]. Skin tissue is particularly sensitive to adverse reactions resulting in radiation dermatitis [11] and is known to compromise the patient's quality of life due to pain, as well as the untimely interruption of radiation treatment, further compromising control of the disease [12, 13].

Whilst surgery and radiotherapy are commonly used for the treatment of primary solid tumours, many patient cases involve malignancies at more advanced stages. The use of chemotherapeutic agents and other small molecule drugs via systemic therapy, either in combination with each other or alone, has formed the basis of treatment for advanced tumours and metastatic malignancies [14]. Chemotherapeutic agents are termed cytotoxic as they impair proliferating cells, primarily through interference with mitosis. However, mitosis being common to both non-malignant and malignant cells, engenders the risk of damage to both cell populations via chemotherapy. Nevertheless, some selectivity is seen towards cancer cells due to comparatively high cellular proliferation of tumour cells relative to normal cells [14]. Unfortunately, the rapidly dividing cells of the bone marrow, gastrointestinal mucosa and hair follicles remain highly susceptible to adverse effects resulting in acute side effects including myelosuppression, nausea and hair loss [15]. Furthermore, a major drawback to chemotherapy is acquired drug resistance, intrinsic to a wide variety of tumour cells upon exposure to the drug itself. Biological resistance mechanisms are well recognised and include increased drug efflux, up-regulation of DNA repair systems, reduced drug uptake and enhanced intracellular detoxification [16]. Whilst chemotherapy and its use in combination with surgery and or radiation therapy has shown promise in cancer treatment, these treatment options are not entirely satisfactory, for both patients and clinicians. More particularly, in advanced forms of the disease such as with metastatic malignant

melanoma, chemotherapy has resulted in low response rates with little survival benefit [17], begging for the rise of more effective treatment modalities.

In contrast to the empirical approach used to develop chemotherapeutics, more recent research has allowed for the formation of a conceptual framework, established on a more substantial understanding of the cellular based mechanistic properties inherent to cancer as a disease. For instance, research over the past decades has uncovered a small number of molecular, biochemical and cellular traits – all acquired capabilities – shared by most, if not all types of human cancer [18-20]. It has been postulated that the vast catalogue of cancer cell genotypes is a manifestation of six essential alterations in cell physiology that collectively dictate cancerous growth: self-sufficiency in growth signals, insensitivity to growth-inhibitory signals, evasion of programmed cell death (apoptosis), limitless replicative potential, sustained angiogenesis and finally, tissue invasion via spreading (metastasis) [19-21]. These alterations in cell physiology have generated specific molecular targets, believed to play a critical role in tumour growth and disease progression [22]. Practitioners of experimental cancer therapeutics have thus been able to apply the term ‘targeted therapy’ to a new generation of treatment modality, designed to interfere with these specific molecular targets. Nanotechnology has shown tremendous promise in the target-specific delivery of various therapeutic, imaging and diagnostic agents within the human body; so much so, that this expanding field may well have even coined the term “nano-theragnostics”. Among the vast plethora of scientific research being undertaken in the field, a significant contribution has, and is continually being applied to cancer research in the way of nano-theragnostic systems; the common goal of which is to increase the theragnostic efficacy and concomitantly reduce undesirable side effects to a manageable level. Nanoparticulate systems offer several attractions in the way of achieving this goal. These attractions, the key properties of nanoparticles (NPs), and how they differ from other cancer drugs shall be discussed herein. Particular attention shall be devoted to silica based core-shell nanocomposite systems, building a case for their application in the treatment and diagnosis of cancer.

1.2 Nanoparticles for cancer theragnostics

There are a wide variety of NP systems currently being probed for cancer therapies. These include Silica NPs [23], polymeric nanoparticles [24], liposomes [25], as well as ceramic [26], magnetic [27], and metallic [28] NPs. Despite the large variation of choice in available nanoparticulate delivery vehicles, each of these systems is developed such that enhanced delivery to the tumour forms a common; the properties allowing such enhancement shall be elaborated on in subsequent sections. The mode of distribution within the body is subject to considerable variation; administrative methods include systemic, local; via subcutaneous or intratumoral administration, and topical administration to name just a few. Although certain modes of delivery are dependent on the type of cancer being targeted – for example, tumour targeting within the brain via systemic administration has proven to be a difficult task [29] – systemic delivery via parenteral routes has grown to be of the more popular, with several excellent reviews [23, 25, 29-31] focussing on studies that have opted for such a delivery method. Passive and active tumour targeting form the basis of NP delivery via systemic administration.

The characteristics of tumour growth are exploited when using the passive form of targeting. Tumours become diffusion limited at volumes of 2 mm³ and above [32]. Diffusion limitation has an impact on oxygen delivery, nutrition intake and waste excretion. To overcome diffusion limitation, vasculature surrounding the tumour is increased through a process termed angiogenesis. Abnormalities in the connective tissue and the basement membrane that line endothelial cells are a characteristic of angiogenesis [33]. Consequently, the incomplete tumour vasculature results in leaky vessels with gap sizes ranging from 100 nm up to 2 µm depending on the type of tumour [34], whereas the fenestrations in vasculature of healthy tissue have dimensions of only 1 to 2 nm [35]. Furthermore, the lack of a well-defined lymphatic system within tumours results in an interstitial pressure gradient. As such, NPs that gain interstitial access to tumours attain comparatively higher retention times than when within normal tissues [32]. The coupling of leaky vasculature and poor lymphatic drainage is termed the enhanced permeability and retention (EPR) effect (Figure 1-1). NPs that are able circulating within the blood for long enough to diffuse

through the leaky tumour vasculature, are in effect, able to enter the interstitium and become entrapped within the tumour for extended periods of time [31, 32, 34]. This is the basis of passive targeting and thus provides a simplistic method for the preferential localisation of nano-scaled delivery systems within tumour tissue.

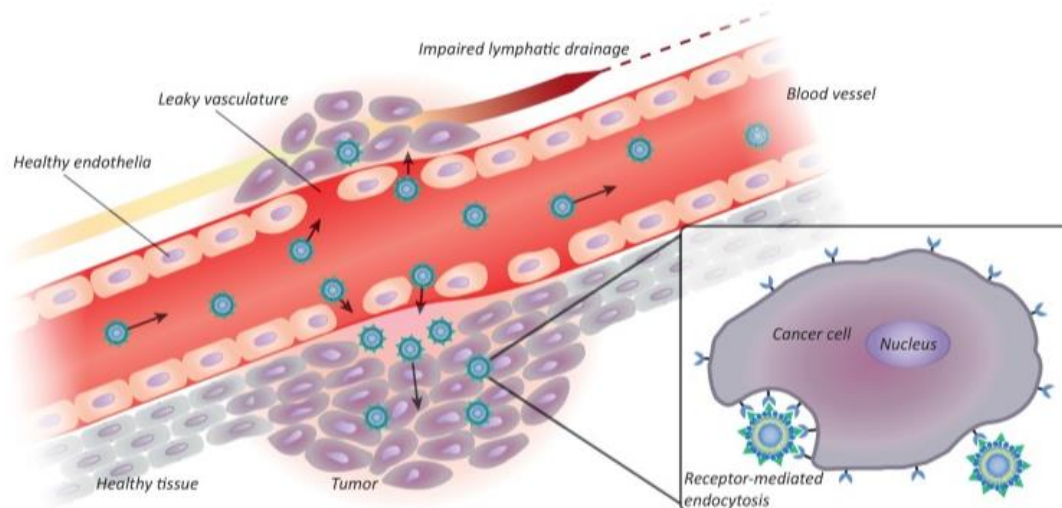


Figure 1-1. Illustrates passive targeting of NPs to tumours through the EPR effect. NPs preferentially accumulate within the tumour interstitium through poorly constructed vessels containing large fenestrae and impaired lymphatic drainage. Post-extravasation, intracellular uptake of ligand functionalised NPs can be facilitated through receptor mediated endocytosis (obtained with permission from [36]).

Active targeting requires the use of peripherally conjugated targeting moieties such as small molecules, peptides, proteins or antibodies [37]. The binding of a ligand molecule with its cell surface receptor is a common process through which numerous intracellular signalling processes occur, allowing for regulation of cellular functions [38]. NPs coated with these small molecules could hypothetically mimic multivalent ligands that are capable of binding with cell surface receptors, allowing them to enter cells via receptor-mediated endocytosis [39] (Figure 1-1). While the size and shape of the NPs can influence cell internalisation, notably, the physical properties of the ligands themselves have also been shown to be an influencing factor; where ligand length, rigidity and density of coverage can strongly affect the final fate of the particle [39].

1.2.1 Distinguishing features of nanoparticles for cancer therapy

The highly tuneable nature of NPs allows them to be designed to specifically improve upon the shortfalls of conventional treatment modalities. However, to meet the criteria required for their effective and safe application as theragnostic agents, a judicious approach in their synthesis is required and, biocompatibility becomes the primary and governing factor in NP design. In therapeutic settings, the biocompatibility of a material is generally measured through parameters such as cell cytotoxicity, in vivo biodistribution, haemocompatibility, and clearance. A number of distinguishing features, inherent to NP design govern their biocompatibility and hence therapeutic fate.

1.2.1.1 *Nanoparticle Size*

The biocompatibility of a nanoparticulate system is dependent on its surface characteristics [40]. Due to their small size NPs have high surface-to-volume ratios, and so control of their size has a great influence on surface characteristics, which play a crucial role in regulating their behaviour in vitro and in vivo. The size of the NP itself can affect cell internalisation, biodistribution and clearance, making it a distinguishing feature for NP based cancer treatment. For example, upon intravenous administration of gold NPs in rats, De Jong et al. showed that 10 nm gold NPs were found to localise in various organs including the liver, spleen, kidney, blood, heart, lung, brain, testes and thymus, whereas larger NPs (50, 100 and 250 nm) were only detected in the blood, liver and spleen [41]. Careful consideration of NP size is therefore a must, to minimise unwanted agglomeration within non-targeted organs and associated toxicity. As mentioned previously, passive targeting of tumours via the EPR effect is dependent on localisation of the NPs within the tumour via fenestrations in poorly formed vasculature. The cut-off size for extravasation from tumour vasculature in animal models has been shown to be slightly narrower at 200 nm to 1.2 μm depending on the tumour type [42]. Therefore, further consideration of NP size must also be taken if a passive targeting method is to be employed in the delivery of theragnostic agents. Active targeting of cancer cells via ligand to cell surface receptor interactions can also be affected by NP size. As

illustrated by Suen and Chau [43], the size of their folate decorated polymeric NPs was found to affect the rate of endocytosis in human retinal pigment epithelium cells, as well as the endocytic pathway. The cellular uptake rate increased with decreasing NP size (50 nm > 120 nm > 250 nm). Furthermore, the 50 and 120 nm particles were observed to undergo both clathrin and caveolae-mediated endocytosis, whereas uptake of the 250 nm was dominated by the caveolae-mediated pathway only. These examples illustrate that significance must be placed on size when considering the design of a nanoparticulate system.

1.2.1.2 *Nanoparticle shape*

The geometry of a NP has been established as a distinguishing feature when considering its biological fate [44]. While spherical NPs currently form the mainstay in shape design for this field of research, numerous fabrication methods have yielded a variety of non-spherical NP shapes. For the successful delivery of a NP to its biological target, it must first be able to circulate in the bloodstream while evading uptake by the mononuclear phagocyte system (MPS; described in the proceeding section). Biodistribution studies with macrophages have demonstrated that the uptake of spherical particles is favoured over NPs with higher aspect ratios. For example, the liver uptake of 100 nm diameter spherical particles was significantly greater than that of 100 nm long nanochains [45]. Furthermore, it was demonstrated that the lower liver uptake of the nanochains correlated to extended blood residence and as a result they outperformed the spherical nanoparticles with regards to tumour extravasation. In another example, a biodistribution study demonstrated that mesoporous silica nanorods with an aspect ratio of 5 (length 720 nm) had half the liver uptake rate of those with an aspect ratio of 1.5 (length 185 nm). Additionally, uptake was found to be organ specific for the different geometries, where the nanorods with an aspect ratio of 1.5 were subject to nearly 3 times higher uptake in the spleen after two hours. The binding avidity of a NP decorated with targeting ligands can also be influenced by NP shape. Kolhar et al. showed using microfluidics, static cell cultures, mathematical modelling and in vivo studies in mice, that rod shaped NPs exhibited greater avidity and selectivity towards endothelium when

compared to their spherical counterparts [46]. These studies demonstrate that consideration of NP shape is necessary when designing theragnostic entities for cancer treatment.

1.2.1.3 *Controllable biodistribution*

The MPS consists of tissue-resident macrophages, dendritic cells and blood monocytes in the spleen, lymph nodes and liver that are responsible for processing and clearing foreign materials from circulation [47]. The adsorption of plasma proteins such as immunoglobulin and its fragments, to the surface of NPs that are circulating within the body, label them as foreign materials (this process is termed opsonisation), affording recognition to phagocytic type cells for clearance [48]. Opsonisation of NPs is a complex process, heavily dependent on the type of adsorbing protein, its spatial arrangement, as well as the physical and chemical state of the NP surface itself. NPs can be modified to protect them from opsonisation, a distinguishing feature when compared to conventional drug molecules used in cancer therapy. PEGylation is the most commonly used method for imparting “stealth” characteristics to NPs for evasion from the MPS, and has been reviewed extensively [48-51]. It involves the grafting of polyethylene glycol (PEG) molecules to the surface of NPs bound for systemic delivery. The hydrophilic nature of PEG has been shown to render the adsorption of biomacromolecules onto NP surfaces thermodynamically unfavourable [52] while concomitantly increasing steric stability through a reduction of surface charge. While having the ability to evade the MPS is a distinguishing feature of PEGylated NPs, use of PEG to this end has also been shown to reduce non-specific NP uptake by cultured cells in vitro [53, 54]. While this outcome mitigates the loss of NPs to non-targeted cells, it is also counterintuitive as cell uptake to target cells is hindered, if further modification is not employed. As Dai et al. have shown, the combination of PEG with a targeting ligand allows specific cell uptake, while concomitantly mitigating serum protein adsorption [55]. Careful control of NP surface chemistry can thus allow for regulation of the therapeutic entity’s biodistribution, enhancing tumour localisation and avoiding clearance due to the body’s immune response.

1.2.1.4 *Cell specificity*

The circumvention of conventional chemotherapy is most widely perpetrated by a phenomenon known as multidrug resistance (MDR). The mechanisms giving rise to MDR can broadly be categorised as cellular and physiological both of which have been reviewed elsewhere [56]. In short, chemotherapeutic agents target rapidly proliferating cells (malignant and non-malignant), the non-malignant cells are destroyed (resulting in undesirable side effects) and malignant cells enacting MDR are spared. This results in large populations of drug resistant malignant cells, requiring higher doses of chemotherapeutic agents, which demonstrate systemic toxicity. The use of NPs functionalised with targeting moieties that promote receptor mediated endocytosis, not only direct the therapeutic entity towards malignant cells overexpressing target receptors (sparing non-malignant cells), but are able to bypass drug efflux transporters, the over-expression of which, forms the most widely encountered MDR phenomenon [57]. Folic acid (FA) is one of the most commonly used targeting moieties in nanoparticulate mediated cancer research. FA is a small molecule vitamin (441 Da) that is essential in eukaryotic cells for the biosynthesis of pyrimidines and purines [58]. The uptake of folates by various cells is enabled by either the low affinity reduced folate carrier, found in most cells of the body, or through the high affinity folate receptor. While the reduced folate carrier enables transport of reduced forms of FA, the folate receptor is capable of transporting FA as well as non-physiologic forms of the vitamin and folate-linked nanoconjugates [59]. The cell surface receptor for FA forms a viable target for tumour cell specific drug delivery for three major reasons. Firstly, it is over-expressed with upregulation nearing two orders of magnitude in many human cancers, including breast, ovary, kidney, brain, lung and myeloid cells [60]. Secondly, access to the folate receptor in non-malignant tissues is compromised due to its location on the outward-facing membrane of polarised epithelia and finally, the density of the folate receptor seems to increase as the disease stage progresses [61]. While FA is the most commonly used ligand based active targeting scheme, many other ligands have been used to such an end, of which transferrin is notable. Transferrin is an iron transporting serum glycoprotein allowing the receptor mediated endocytosis of iron from the blood into

cells via cell surface transferrin receptors [32]. Over expression of transferrin receptors on drug resistant malignant cells, the extracellular status of transferrin in the body and its internalisation by cells, make transferrin a suitable cell targeting agent in cancer therapy [58]. The use of targeting ligands has been demonstrated to not only impart cell specificity [62], but to also enhance cellular uptake [63]. In a clinical setting, such properties would show great promise in mitigating the effects of MDR while concomitantly reducing undesirable side effects.

1.2.2 Core-shell nanoparticles

NPs offer many positive attributes towards the design of a cancer treatment modality geared towards clinical use. The core-shell NP concept, as the name implies, refers to a composite NP system comprising an inner core material, enveloped by an outer casing of another material that forms the shell. It is important to note that all of the distinguishing features discussed in preceding sections must still be considered when applying the core-shell concept to the design and preparation of a NP system geared towards clinical deployment. In fact, the core-shell design offers flexibility as well as many advantages over homogeneous single particle systems when it comes employing these features. For instance, controlling the size and shape of the core material would ultimately decide the size and shape of the core-shell composite. Furthermore, a core material need not necessarily be biocompatible as the use of a biocompatible outer shell may shield from any negative impact inflicted within a biological setting. The composite nature of such NPs gives rise to a plethora of core-shell based systems, with various combinations of core and shell material types ranging from organic-organic, organic-inorganic and vice versa, as well as inorganic-inorganic materials. Furthermore, the core or shell or both may also be composites of inorganic and organic materials themselves; the combination depending on the intended application and fate of the NP. The numerous possible arrangements give rise to a huge variety of core-shell systems many of which have been extensively reviewed elsewhere for the readers reference [64, 65]. In most instances, for cancer therapy, the core material generally comprises the theragnostic entity, while the shell component serves either to enhance the biocompatibility of the core material, increase the stability of the system in biological settings, and or provide a surface for

functionalisation that will allow for these to be carried out. For example, the TiO₂-SiO₂ photosensitiser developed by a previous member of our research group, Feng et al. [66] comprises a photoactive titanium dioxide core utilised as a therapeutic agent for the destruction of human nasopharyngeal epidermoid cancer cells via photodynamic therapy (PDT). A silica shell was used to improve the dispersion of the core material while providing a site to anchor folic acid targeting ligands. In another example [67], Tan and co-workers developed a double shelled system with a hollow core for the delivery of the antineoplastic drug mitoxantrone (mito). The mesoporous silica shell allowed diffusion of the drug in and out of the hollow cores. Their double shell design allowed the storage of over twice the amount of mito within the hollow core and void space between shells, when compared to just the hollow core of a corresponding single shelled system. Lin et al. demonstrated that their PEGylated silica based core-shell NPs were able to act as a positive contrast agent for neurovascular magnetic resonance (MR) imaging due to the gadolinium (Gd) core material [68]. They reported that the PEG coating and microporous silica shell allowed water exchange while keeping the toxic Gd core from leaching out. These examples clearly indicate the versatility of design options available through the use of the core-shell concept, also highlighting the ease with which NP systems can be designed to incorporate the features that distinguish them from conventional cancer treatment modalities.

Whilst core-shell NPs can be synthesised using any combination of organic and or inorganic material for either core or shell component, inorganic materials such as metals and metal oxides are more commonly used for the core [64]. Metals such as gold, silver and copper have been used as core materials for their surface plasmon resonance (SPR) based theragnostic properties. Strong electromagnetic fields on the surface of the metal NPs are generated due to coherent oscillation of free surface electrons upon interaction with the oscillating electric fields of incident light. These electromagnetic fields enhance both the absorption and scattering properties of the metal [69]. Smaller gold and silver NPs are preferentially used for photo-thermal therapy, where irradiated light is absorbed by the NPs and efficiently converted to heat resulting in hyperthermia of targeted cells and tissue. Larger NP counterparts are preferred for imaging due to their higher scattering efficiency [70]. Iron and iron

oxide based cores have been used widely as contrast agents in MRI [71], for local hyperthermia [72] and for drug delivery systems employing external magnetic fields for tumour localisation [73]. Semiconducting materials such as quantum dots (QD), titanium dioxide (TiO₂) and zinc oxide (ZnO) have shown great promise as core materials for PDT applications [74]. In the case of semiconducting cores, irradiation results in photo-excitation of electrons from the valence band to the conduction band. The electron-hole pairs are able to react with water and oxygen within the biological environment to generate reactive oxygen species (ROS) such as superoxide and hydroxyl radicals, which in turn may cause oxidative stresses that lead to necrosis and apoptosis [66].

Extensive research has been carried out in the use of heterogeneous semiconductor materials as photocatalysts and in enhancing their photocatalytic properties [75-77]. Application of the core-shell design concept to these materials may allow a transition for their use as photosensitisers with all the desirable traits for efficacious PDT. This forms the basis of this thesis and is elaborated on in the proceeding sections.

1.3 Thesis overview

1.3.1 Aims and objectives

The purpose of this dissertation was to fabricate and characterise, using a facile synthetic approach, a core-shell nanoparticulate system for applications as a dual functional photosensitiser in photodynamic therapy. The core was to comprise of a hybrid, magnetic, iron oxide-zinc oxide (Fe₃O₄-ZnO) material, enveloped by a silica shell decorated with folic acid targeting ligands, a dansyl chloride based fluorescent molecule and polyethylene glycol. The Fe₃O₄-ZnO composite was first developed by this group to improve upon the photophysical properties of pure ZnO NPs intended for the photodegradation of a water contaminant, viz. phenol [78]. The design consisted of a heterogeneous semiconductor material, synthesised via a seed mediated growth process, where Fe₃O₄ NPs were used as seeds for the growth of the ZnO semiconductor. The presence of the Fe₃O₄ served to mitigate recombination of

photoinduced electron-hole pairs thereby increasing the phenol degradation efficiency to 82%, from 52% when using pure ZnO NPs alone.

The objectives of this research include: (1) the surface modification of the Fe₃O₄-ZnO core via inclusion of a silica shell functionalised with various surface groups to impart biocompatibility, cell specificity, fluorescent capabilities for imaging and stealth properties. (2) The chemical and physical examination of the core, shell and surface bound moieties and (3) The examination of cyto- and phototoxicity of the core material, the silica shell itself, and the entire folic acid bound core-shell structure, in order to evaluate the photoefficiency of the hybrid core and the effect of surface modification on its efficacy as a photosensitiser.

1.3.2 Research methodology

A detailed flow chart of the thesis work is presented in Figure 1-2. In brief, a hollow silica shell will be fabricated with controllable size. The toxicity and specificity of this shell towards malignant and non-malignant cell lines will be evaluated. The influence of attached folic acid molecules shall be investigated and the potential for its use as a drug carrier shall be scrutinised. The developed shell system will then be applied to the Fe₃O₄-ZnO core. The photocatalytic properties of the resultant folate bound core-shell system shall be evaluated via photodegradation of methylene blue (MB) and the influence of surface modification on photocatalytic efficiency, cyto- and phototoxicity determined. Finally, additional surface modifications shall be carried out through use of PEG and dansyl chloride. PEG chains shall be grafted to the surface of the shell component both directly and acting as a spacer for terminal folate groups. A fluorescent dansyl moiety shall be grafted to the silica shell also with and without a PEG spacer. The influence of these surface modifications on the photocatalytic properties of the hybrid core shall be evaluated via MB degradation. Viability of the fluorescent molecule for potential imaging applications shall also be investigated.

A rigorous physicochemical characterisation scheme shall be employed to scrutinise the synthetic products. Transition electron microscopy (TEM), scanning electron microscopy (SEM) and dynamic light scattering (DLS) shall be used to analyse morphology, size and size distribution. Several spectroscopic techniques including Fourier transform infra-red (FTIR), ultra violet – visible (UV-Vis) absorption,

fluorescence and nuclear magnetic resonance (NMR) shall be used to confirm conjugation of the various surface molecules. Finally, thermogravimetric analysis (TGA) shall be used to quantify these groups.

The photodegradation of methylene blue shall be carried out using a UV chamber and UV-vis absorption spectroscopy for quantification of the dye molecule, Figure 1-3 details a schematic diagram of the apparatus. Photokilling experiments will be conducted in a similar chamber type setup, with the double jacket reactor being replaced by 96 well cell culture plates; details are elaborated in chapter 3.

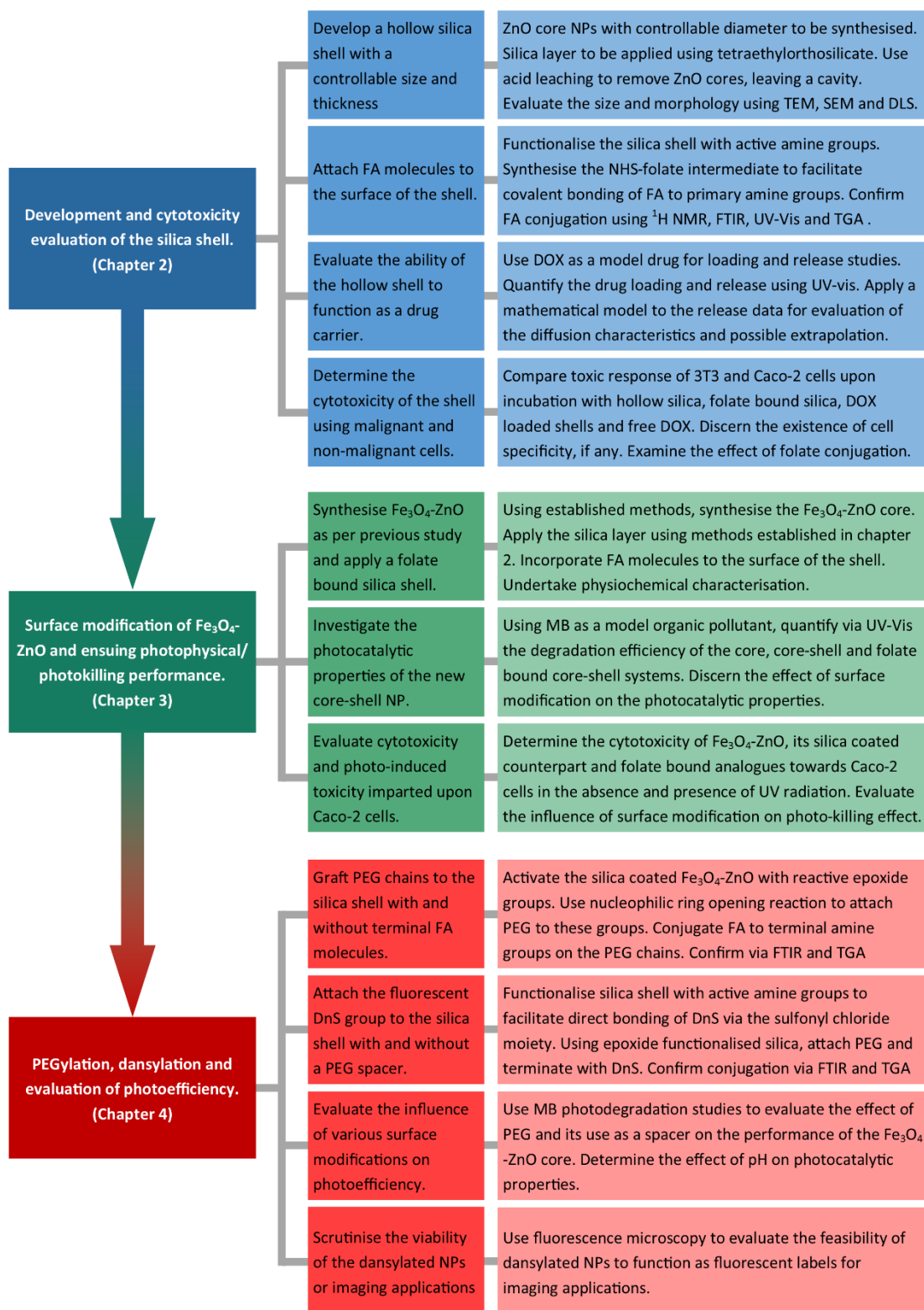


Figure 1-2. A flow chart detailing the research methodology employed in this dissertation.

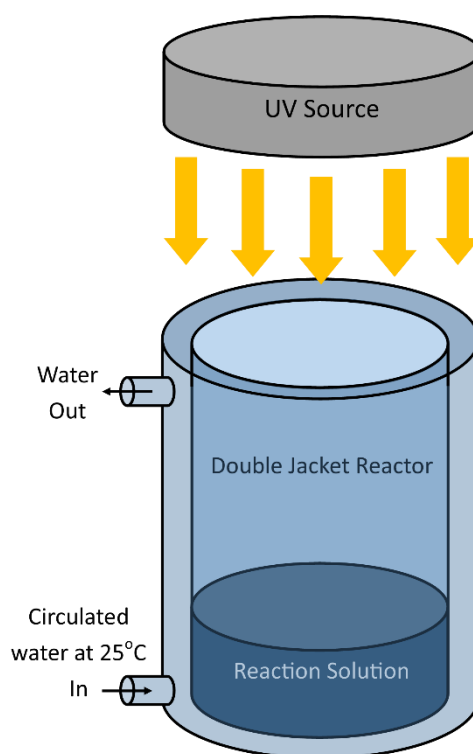


Figure 1-3. A schematic diagram detailing the photocatalytic reaction apparatus

1.3.3 Expected outcomes and significance

The background information pertaining to current cancer treatment modalities has highlighted the need for novel materials and methods to be exploited if the mortality and morbidity associated with the disease are to be reduced, thus paving the way for nanoparticulate based theragnostic systems. This dissertation hopes to develop and implement a novel synthetic route, based on a core-shell design, to enhance the biocompatibility, cell specificity and efficacy of therapeutic agents intended for cancer treatment. As chapter two will show, incorporation of such a methodology to small molecule drugs, can improve their specificity and cytotoxic effect towards malignant cells. Furthermore, application of this system to photocatalysts as per chapter 3, will provide a transition of those materials to applications in photodynamic therapy. Chapter 4 will highlight the versatility of the synthetic method by illustrating the various surface modifications possible and will demonstrate how the employed method can be used to design multifaceted theragnostic systems. Finally, chapter 5 shall summarise the major outcomes of this research and will detail future considerations.

1.4 References

- [1] J. Ferlay, I. Soerjomataram, M. Ervik, R. Dikshit, S. Eser, C. Mathers, M. Rebelo, D. Parkin, D. Forman, F. Bray, GLOBOCAN 2012 v1.0, Cancer Incidence and Mortality Worldwide: IARC CancerBase No. 11, GLOBOCAN 2012 v1.0, Cancer Incidence and Mortality Worldwide: IARC CancerBase No. 11, International Agency for Research on Cancer (IARC), Lyon, France, 2013.
- [2] A.I.o.H.a. Welfare, Australian Cancer Incidence and Mortality (ACIM) books: All cancers combined, Australian Cancer Incidence and Mortality (ACIM) books: All cancers combined, Australian Institute of Health and Welfare (AIHW), Canberra, Australia, 2015.
- [3] I.F. Tannock, Conventional cancer therapy: promise broken or promise delayed?, *The Lancet* 351, Supplement 2 (1998) SII9-SII16.
- [4] L. Horn, D.H. Johnson, Ephraim McDowell, the First Ovariectomy, and the Birth of Abdominal Surgery, *Journal of Clinical Oncology* 28(7) (2010) 1262-1268.
- [5] A.C. Society, Cancer Facts & Figures 2015, American Cancer Society, Cancer Facts and Figures 2015, Atlanta: American Cancer Society, 2015.
- [6] B. Kasper, V. D'Hondt, P. Vereecken, A. Awada, Novel treatment strategies for malignant melanoma: A new beginning?, *Critical Reviews in Oncology/Hematology* 62(1) (2007) 16-22.
- [7] C.H. Yarbro, D. Wujcik, B.H. Gobe, Cancer nursing : principles and practice, Jones and Bartlett Publishers, Sudbury, MA, USA, 2010, p. 1946.
- [8] W.P. Hogle, The State of the Art in Radiation Therapy, *Seminars in Oncology Nursing* 22(4) (2006) 212-220.
- [9] F. Ballarini, S. Altieri, S. Bortolussi, E. Giroletti, N. Protti, A Model of Radiation-Induced Cell Killing: Insights into Mechanisms and Applications for Hadron Therapy, *Radiation Research* 180(3) (2013) 307-15.
- [10] M. Perez-Aso, A. Mediero, Y.C. Low, J. Levine, B.N. Cronstein, Adenosine A2A receptor plays an important role in radiation-induced dermal injury, *The FASEB Journal* (2015).
- [11] J.L. Ryan, Ionizing Radiation: The Good, the Bad, and the Ugly, *J Invest Dermatol* 132(3) (2012) 985-993.
- [12] C. Robertson, A.G. Robertson, J.H. Hendry, S.A. Roberts, N.J. Slevin, W.B. Duncan, R.H. MacDougall, G.R. Kerr, B. O'Sullivan, T.J. Keane, Similar decreases in local tumor control are calculated for treatment protraction and for interruptions in the radiotherapy of carcinoma of the larynx in four centers, *International Journal of Radiation Oncology • Biology • Physics* 40(2) (1998) 319-329.
- [13] N. Salvo, E. Barnes, J. van Draanen, E. Stacey, G. Mitera, D. Breen, A. Giotis, G. Czarnota, J. Pang, C. De Angelis, Prophylaxis and management of acute radiation-induced skin reactions: a systematic review of the literature, *Current Oncology* 17(4) (2010) 94-112.
- [14] P.G. Corrie, Cytotoxic chemotherapy: clinical aspects, *Medicine* 39(12) (2011) 717-722.
- [15] M.J. Lind, Principles of cytotoxic chemotherapy, *Medicine* 39(12) (2011) 711-716.
- [16] G. Makin, C. Dive, Apoptosis and cancer chemotherapy, *Trends in Cell Biology* 11(11) (2001) S22-S26.
- [17] M.R. Middleton, J.J. Grob, N. Aaronson, G. Fierlbeck, W. Tilgen, S. Seiter, M. Gore, S. Aamdal, J. Cebon, A. Coates, B. Dreno, M. Henz, D. Schadendorf, A. Kapp, J. Weiss, U. Fraass, P. Statkevich, M. Muller, N. Thatcher, Randomized Phase III Study of Temozolomide Versus Dacarbazine in the Treatment of Patients With Advanced Metastatic Malignant Melanoma, *Journal of Clinical Oncology* 18(1) (2000) 158.
- [18] J. Gabriel, What is Cancer?, *The Biology of Cancer*, John Wiley & Sons Ltd 2008, pp. 3-9.
- [19] D. Hanahan, R.A. Weinberg, The Hallmarks of Cancer, *Cell* 100(1) (2000) 57-70.
- [20] D. Hanahan, Robert A. Weinberg, Hallmarks of Cancer: The Next Generation, *Cell* 144(5) (2011) 646-674.
- [21] K.J. Harrington, Biology of cancer, *Medicine* 36(1) (2008) 1-4.
- [22] C. Sawyers, Targeted cancer therapy, *Nature* 432(7015) (2004) 294-297.

- [23] Y. Yang, C. Yu, Advances in silica based nanoparticles for targeted cancer therapy, *Nanomedicine: Nanotechnology, Biology and Medicine* 12(2) (2016) 317-332.
- [24] Prabhu RH, Patravale VB, J. MD, Polymeric nanoparticles for targeted treatment in oncology: current insights, *International journal of nanomedicine* 10 (2015) 1001-1018.
- [25] B. Ozpolat, A.K. Sood, G. Lopez-Berestein, Liposomal siRNA nanocarriers for cancer therapy, *Advanced Drug Delivery Reviews* 66 (2014) 110-116.
- [26] A. Baeza, *Ceramic Nanoparticles for Cancer Treatment, Bio-Ceramics with Clinical Applications*, John Wiley & Sons, Ltd 2014, pp. 421-455.
- [27] R.A. Revia, M. Zhang, Magnetite nanoparticles for cancer diagnosis, treatment, and treatment monitoring: recent advances, *Materials Today* 19(3) (2016) 157-168.
- [28] V. Mirabello, D.G. Calatayud, R.L. Arrowsmith, H. Ge, S.I. Pascu, Metallic nanoparticles as synthetic building blocks for cancer diagnostics: from materials design to molecular imaging applications, *Journal of Materials Chemistry B* 3(28) (2015) 5657-5672.
- [29] Y. Chen, L. Liu, Modern methods for delivery of drugs across the blood-brain barrier, *Advanced Drug Delivery Reviews* 64(7) (2012) 640-665.
- [30] M.J. Sailor, J.-H. Park, Hybrid Nanoparticles for Detection and Treatment of Cancer, *Advanced Materials* 24(28) (2012) 3779-3802.
- [31] I. Brigger, C. Dubernet, P. Couvreur, Nanoparticles in cancer therapy and diagnosis, *Advanced Drug Delivery Reviews* 64, Supplement(0) (2012) 24-36.
- [32] J.D. Byrne, T. Betancourt, L. Brannon-Peppas, Active targeting schemes for nanoparticle systems in cancer therapeutics, *Advanced Drug Delivery Reviews* 60(15) (2008) 1615-1626.
- [33] D.F. Baban, L.W. Seymour, Control of tumour vascular permeability, *Advanced Drug Delivery Reviews* 34(1) (1998) 109-119.
- [34] V. Torchilin, Tumor delivery of macromolecular drugs based on the EPR effect, *Advanced Drug Delivery Reviews* 63(3) (2011) 131-135.
- [35] S.K. Hobbs, W.L. Monsky, F. Yuan, W.G. Roberts, L. Griffith, V.P. Torchilin, R.K. Jain, Regulation of transport pathways in tumor vessels: Role of tumor type and microenvironment, *Proceedings of the National Academy of Sciences* 95(8) (1998) 4607-4612.
- [36] G.T. Noble, J.F. Stefanick, J.D. Ashley, T. Kiziltepe, B. Bilgicer, Ligand-targeted liposome design: challenges and fundamental considerations, *Trends in Biotechnology* 32(1) (2014) 32-45.
- [37] N. Bertrand, J. Wu, X. Xu, N. Kamaly, O.C. Farokhzad, Cancer nanotechnology: The impact of passive and active targeting in the era of modern cancer biology, *Advanced Drug Delivery Reviews* 66 (2014) 2-25.
- [38] W. Jiang, Y.S. KimBetty, J.T. Rutka, C.W. ChanWarren, Nanoparticle-mediated cellular response is size-dependent, *Nat Nano* 3(3) (2008) 145-150.
- [39] H.-m. Ding, Y.-q. Ma, Role of physicochemical properties of coating ligands in receptor-mediated endocytosis of nanoparticles, *Biomaterials* 33(23) (2012) 5798-5802.
- [40] A.A. John, A.P. Subramanian, M.V. Vellayappan, A. Balaji, S.K. Jaganathan, H. Mohandas, T. Paramalinggam, E. Supriyanto, M. Yusof, Review: physico-chemical modification as a versatile strategy for the biocompatibility enhancement of biomaterials, *RSC Advances* 5(49) (2015) 39232-39244.
- [41] W.H. De Jong, W.I. Hagens, P. Krystek, M.C. Burger, A.J.A.M. Sips, R.E. Geertsma, Particle size-dependent organ distribution of gold nanoparticles after intravenous administration, *Biomaterials* 29(12) (2008) 1912-1919.
- [42] A.D. Wong, M. Ye, M.B. Ulmschneider, P.C. Searson, Quantitative Analysis of the Enhanced Permeation and Retention (EPR) Effect, *PLoS ONE* 10(5) (2015) e0123461.
- [43] W.-L.L. Suen, Y. Chau, Size-dependent internalisation of folate-decorated nanoparticles via the pathways of clathrin and caveolae-mediated endocytosis in ARPE-19 cells, *Journal of Pharmacy and Pharmacology* 66(4) (2014) 564-573.

- [44] R. Toy, P.M. Peiris, K.B. Ghaghada, E. Karathanasis, Shaping cancer nanomedicine: The effect of particle shape on the in vivo journey of nanoparticles, *Nanomedicine (London, England)* 9(1) (2014) 121-134.
- [45] P.M. Peiris, L. Bauer, R. Toy, E. Tran, J. Pansky, E. Doolittle, E. Schmidt, E. Hayden, A. Mayer, R.A. Keri, M.A. Griswold, E. Karathanasis, Enhanced Delivery of Chemotherapy to Tumors Using a Multi-Component Nanochain with Radiofrequency-Tunable Drug Release, *ACS Nano* 6(5) (2012) 4157-4168.
- [46] P. Kolhar, A.C. Anselmo, V. Gupta, K. Pant, B. Prabhakarpandian, E. Ruoslahti, S. Mitragotri, Using shape effects to target antibody-coated nanoparticles to lung and brain endothelium, *Proceedings of the National Academy of Sciences* 110(26) (2013) 10753-10758.
- [47] C.D. Walkey, W.C.W. Chan, Understanding and controlling the interaction of nanomaterials with proteins in a physiological environment, *Chemical Society Reviews* 41(7) (2012) 2780-2799.
- [48] S.M. Moghimi, A.C. Hunter, T.L. Andresen, Factors Controlling Nanoparticle Pharmacokinetics: An Integrated Analysis and Perspective, *Annual Review of Pharmacology and Toxicology* 52(1) (2012) 481-503.
- [49] J.V. Jokerst, T. Lobovkina, R.N. Zare, S.S. Gambhir, Nanoparticle PEGylation for imaging and therapy, *Nanomedicine (London, England)* 6(4) (2011) 715-728.
- [50] K. Knop, R. Hoogenboom, D. Fischer, U.S. Schubert, Poly(ethylene glycol) in Drug Delivery: Pros and Cons as Well as Potential Alternatives, *Angewandte Chemie International Edition* 49(36) (2010) 6288-6308.
- [51] S. Naahidi, M. Jafari, F. Edalat, K. Raymond, A. Khademhosseini, P. Chen, Biocompatibility of engineered nanoparticles for drug delivery, *Journal of Controlled Release* 166(2) (2013) 182-194.
- [52] A.J. Pertsin, M. Grunze, Computer Simulation of Water near the Surface of Oligo(ethylene glycol)-Terminated Alkanethiol Self-Assembled Monolayers, *Langmuir* 16(23) (2000) 8829-8841.
- [53] S. Hak, E. Helgesen, H.H. Hektoen, E.M. Huuse, P.A. Jarzyna, W.J.M. Mulder, O. Haraldseth, C.d.L. Davies, The Effect of Nanoparticle Polyethylene Glycol Surface Density on Ligand-Directed Tumor Targeting Studied in Vivo by Dual Modality Imaging, *ACS Nano* 6(6) (2012) 5648-5658.
- [54] B. Pelaz, P. del Pino, P. Maffre, R. Hartmann, M. Gallego, S. Rivera-Fernández, J.M. de la Fuente, G.U. Nienhaus, W.J. Parak, Surface Functionalization of Nanoparticles with Polyethylene Glycol: Effects on Protein Adsorption and Cellular Uptake, *ACS Nano* 9(7) (2015) 6996-7008.
- [55] Q. Dai, C. Walkey, W.C.W. Chan, Polyethylene Glycol Backfilling Mitigates the Negative Impact of the Protein Corona on Nanoparticle Cell Targeting, *Angewandte Chemie International Edition* 53(20) (2014) 5093-5096.
- [56] N.R. Patel, B.S. Pattni, A.H. Abouzeid, V.P. Torchilin, Nanopreparations to overcome multidrug resistance in cancer, *Advanced Drug Delivery Reviews* 65(13-14) (2013) 1748-1762.
- [57] S. Dawar, N. Singh, R.K. Kanwar, R.L. Kennedy, R.N. Veedu, S.-F. Zhou, S. Krishnakumar, S. Hazra, S. Sasidharan, W. Duan, J.R. Kanwar, Multifunctional and multitargeted nanoparticles for drug delivery to overcome barriers of drug resistance in human cancers, *Drug Discovery Today* 18(23-24) (2013) 1292-1300.
- [58] R. Bazak, M. Houry, S. El Achy, S. Kamel, T. Refaat, Cancer active targeting by nanoparticles: a comprehensive review of literature, *Journal of Cancer Research and Clinical Oncology* 141(5) (2015) 769-784.
- [59] S.R. Grobmyer, B.M. Moudgil, S.A. Kularatne, P.S. Low, Targeting of Nanoparticles: Folate Receptor, in: J.M. Walker (Ed.), *Cancer Nanotechnology*, Humana Press 2010, pp. 249-265.

- [60] J.F. Ross, P.K. Chaudhuri, M. Ratnam, Differential regulation of folate receptor isoforms in normal and malignant tissues in vivo and in established cell lines. *Physiologic and clinical implications*, *Cancer* 73(9) (1994) 2432-2443.
- [61] Y. Lu, P.S. Low, Folate-mediated delivery of macromolecular anticancer therapeutic agents, *Advanced Drug Delivery Reviews* 64, Supplement(0) (2012) 342-352.
- [62] J. Liu, W. Zhang, H. Zhang, Z. Yang, T. Li, B. Wang, X. Huo, R. Wang, H. Chen, A multifunctional nanoprobe based on Au-Fe₃O₄ nanoparticles for multimodal and ultrasensitive detection of cancer cells, *Chemical Communications* 49(43) (2013) 4938-4940.
- [63] X. Liu, F. Fu, K. Xu, R. Zou, J. Yang, Q. Wang, Q. Liu, Z. Xiao, J. Hu, Folic acid-conjugated hollow mesoporous silica/CuS nanocomposites as a difunctional nanoplatform for targeted chemo-photothermal therapy of cancer cells, *Journal of Materials Chemistry B* 2(33) (2014) 5358-5367.
- [64] R. Ghosh Chaudhuri, S. Paria, *Core/Shell Nanoparticles: Classes, Properties, Synthesis Mechanisms, Characterization, and Applications*, *Chemical Reviews* 112(4) (2012) 2373-2433.
- [65] W. Schartl, Current directions in core-shell nanoparticle design, *Nanoscale* 2(6) (2010) 829-843.
- [66] X. Feng, S. Zhang, H. Wu, X. Lou, A novel folic acid-conjugated TiO₂-SiO₂ photosensitizer for cancer targeting in photodynamic therapy, *Colloids and Surfaces B: Biointerfaces* 125(0) (2015) 197-205.
- [67] L. Tan, T. Liu, L. Li, H. Liu, X. Wu, F. Gao, X. He, X. Meng, D. Chen, F. Tang, Uniform double-shelled silica hollow spheres: acid/base selective-etching synthesis and their drug delivery application, *RSC Advances* 3(16) (2013) 5649-5655.
- [68] W.-I. Lin, C.-Y. Lin, Y.-S. Lin, S.-H. Wu, Y.-R. Huang, Y. Hung, C. Chang, C.-Y. Mou, High payload Gd(III) encapsulated in hollow silica nanospheres for high resolution magnetic resonance imaging, *Journal of Materials Chemistry B* 1(5) (2013) 639-645.
- [69] H. Sharma, P.K. Mishra, S. Talegaonkar, B. Vaidya, Metal nanoparticles: a theranostic nanotool against cancer, *Drug Discovery Today* 20(9) (2015) 1143-1151.
- [70] P.K. Jain, K.S. Lee, I.H. El-Sayed, M.A. El-Sayed, Calculated Absorption and Scattering Properties of Gold Nanoparticles of Different Size, Shape, and Composition: Applications in Biological Imaging and Biomedicine, *The Journal of Physical Chemistry B* 110(14) (2006) 7238-7248.
- [71] G. Mikhaylov, U. Mikac, A.A. Magaeva, V.I. Itin, E.P. Naiden, I. Psakhye, L. Babes, T. Reinheckel, C. Peters, R. Zeiser, M. Bogyo, V. Turk, S.G. Psakhye, B. Turk, O. Vasiljeva, Ferri-liposomes as an MRI-visible drug-delivery system for targeting tumours and their microenvironment, *Nat Nano* 6(9) (2011) 594-602.
- [72] A.E. Deatsch, B.A. Evans, Heating efficiency in magnetic nanoparticle hyperthermia, *Journal of Magnetism and Magnetic Materials* 354 (2014) 163-172.
- [73] Z. Zhou, Y. Sun, J. Shen, J. Wei, C. Yu, B. Kong, W. Liu, H. Yang, S. Yang, W. Wang, Iron/iron oxide core/shell nanoparticles for magnetic targeting MRI and near-infrared photothermal therapy, *Biomaterials* 35(26) (2014) 7470-7478.
- [74] S.S. Lucky, K.C. Soo, Y. Zhang, Nanoparticles in Photodynamic Therapy, *Chemical Reviews* 115(4) (2015) 1990-2042.
- [75] H. Wang, L. Zhang, Z. Chen, J. Hu, S. Li, Z. Wang, J. Liu, X. Wang, Semiconductor heterojunction photocatalysts: design, construction, and photocatalytic performances, *Chemical Society Reviews* 43(15) (2014) 5234-5244.
- [76] H. Kisch, *Semiconductor Photocatalysis—Mechanistic and Synthetic Aspects*, *Angewandte Chemie International Edition* 52(3) (2013) 812-847.
- [77] N. Serpone, A.V. Emeline, *Semiconductor Photocatalysis — Past, Present, and Future Outlook*, *The Journal of Physical Chemistry Letters* 3(5) (2012) 673-677.

[78] X. Feng, H. Guo, K. Patel, H. Zhou, X. Lou, High performance, recoverable Fe₃O₄-ZnO nanoparticles for enhanced photocatalytic degradation of phenol, *Chemical Engineering Journal* 244(0) (2014) 327-334.

CHAPTER 2

2 Drug release characteristics and selective cytotoxicity of hollow silica nanoparticles

2.1 Introduction

Siliceous nano-composite materials have elicited growing interest in the field of cancer treatment through drug delivery and diagnostics [1], due to their controllable physiochemical properties including size, morphology, composition, biocompatibility and ease of surface functionalisation when compared to other nanomaterials [2, 3]. The vast potential of silica nanocomposites is demonstrated by Benezra et al's work through the synthesis of FDA approved diagnostic multimodal silica nanoparticles (NPs) [4, 5]. Their dye-encapsulated particles, approved for the first-in-human clinical trial of their class, were surface functionalised with cyclic arginine-glycine-aspartic acid peptide ligands and radioiodine. This afforded effective renal clearance with concurrent tumour targeting and sensitive in vivo imaging. While notable advancements have been realised through the use of silica NPs in a diagnostic regime [6], promising results in the way of in vitro and in vivo drug delivery also have been demonstrated. In this light, encapsulation of therapeutic agents by silica shells including drugs such as paclitaxel [7], gemcitabine [8] and bortezomib [9], has allowed for suppression in the growth of malignant cell lines in vitro and tumour

shrinkage in vivo with more efficacious results than using the free drug alone. Studies have also shown greater efficacy through use of silica nanoparticle encapsulated doxorubicin hydrochloride (DOX) than when using free DOX, both in vitro [10, 11] and in vivo [11]. While these studies report the advantages of drug encapsulation, the silica NP carriers have been demonstrated to be compatible with both non-malignant and malignant cells in the absence of DOX. A recent study by Tan et al [12] concluded that double layered hollow silica nano-spheres of 260 nm diameter alone were not toxic at concentrations as high as 400 $\mu\text{g}\cdot\text{mL}^{-1}$. Another study by Zhao et al. [13] reported that hollow silica NPs of 30 nm diameter showed negligible cytotoxicity after 48 h incubation at a concentration up to 200 $\mu\text{g}\cdot\text{mL}^{-1}$. Both groups used human liver carcinoma (HepG2) cell lines, while Zhao and co-workers also used HeLa, RAW 264.7, SMMC-7721 and MCF-7 cells. A separate study [14] used 110 nm sized hollow silica particles at similar concentrations and a 48 h incubation period to find no obvious toxicity in human breast cancer (ZR75-30) cells. These results suggest hollow silica particles alone can be non-toxic to a variety of cell types.

However, studies on solid silica NPs have emerged to show contradictory results. Early studies [15, 16] on commercially available amorphous silica NPs with diameters of about 15 nm have found time and concentration dependant toxicity to human lung adenocarcinoma (A549) cells, exhibiting toxic effects at concentrations of 50 $\mu\text{g}\cdot\text{mL}^{-1}$ and greater when exposure times were 24 h and longer. A recent study [17] on 20 nm commercial silica particles found the cell viability of human gastric cancer (MGC80-3) cells was reduced to 25% (48 h) and 12% (72 h) upon incubation with the NPs at a concentration of 320 $\mu\text{g}\cdot\text{mL}^{-1}$. Reduction in viability of human cervical cancer (HeLa) cells was also observed, to a lesser degree (61% and 65%) at concentrations as low as 20 $\mu\text{g}\cdot\text{mL}^{-1}$ for the same incubation periods. Data on non-cancerous cells was not reported in the work. Aside from commercially obtained NPs, studies employing the commonly used Stöber synthetic route for silica NPs have also emerged within the last decade, suggesting particle associated toxicity in vitro. Chang et al [18] used Stöber based silica particles to find a NP concentration of 667 $\mu\text{g}\cdot\text{mL}^{-1}$ was required to reduce the viability of six different cell lines to between 60 and 80% of the control after a 48 h incubation period. More recently, Gonzalez and co-workers [19] investigated the influence of serum on cell viability, cell cycle and generation of

micronuclei by silica NPs. In serum free conditions Stöber based NPs of sizes 28, 59 and 139 nm were observed to induce at least a 50 ± 5 % reduction in cell viability at doses of $27.5 \mu\text{g}\cdot\text{mL}^{-1}$ (28 nm) and $100 \mu\text{g}\cdot\text{mL}^{-1}$ (59 and 139 nm NPs). In the presence of serum, the viability was also seen to diminish, however to a lesser extent. Kim et al. [20] reported a reduction of A549 and HepG2 cell viability to between 60 and 80% by NPs of strictly controlled sizes (20-200 nm) at concentrations of $\geq 50 \mu\text{g}\cdot\text{mL}^{-1}$ for a 24 h incubation period. They observed time and dose dependent reduction of viability between 20 % and 60 % under the same conditions for mouse embryonic fibroblast (3T3) cells, with their 60 nm particles showing exaggerated (as low as 0-10%) diminution in viability at 200 and $500 \mu\text{g}\cdot\text{mL}^{-1}$. Yu et al. [21] also reported a significant reduction in the cell viability of A549 cells upon 24 h incubation with 62 nm silica NPs. These studies have suggested that in vitro toxicity, associated with use of amorphous silica based NPs, could be induced by a myriad of complicated processes including reactive oxygen species (ROS) generation [21], changes in membrane integrity induced by cellular uptake of NPs [20], influence of serum [19], metabolic activity type of the cell line [18], as well as simply adjusting dose, size of NPs and time of exposure to cells.

This investigation reports on the synthesis of two size-different hollow silica shells, and their toxic effects to human epithelial colorectal adenocarcinoma (Caco-2) and 3T3 cells, with and without encapsulated DOX. Conjugation of folic acid (FA), a cancer cell targeting ligand, to the hollow silica nanoparticles was also explored and its effect on the cell viability was investigated. The results demonstrated that both the hollow silica nanoparticles and the FA conjugated counterparts can produce selectively enhanced cytotoxicity to Caco-2 cells over 3T3 cells, which was not seen with the free anticancer drug DOX under the same conditions. Synergistic toxicity was demonstrated when silica NP encapsulated DOX was used. To the best of our knowledge, this is the first report identifying the selective cytotoxicity of hollow silica nanoparticles towards a cancer cell line. It also was interesting to discover that the conjugated FA at the investigated concentration range encouraged the growth of both 3T3 and Caco-2 cells.

2.2 Materials and Methods

2.2.1 Materials

The following chemicals were purchased from Sigma-Aldrich Australia: zinc acetate dihydrate ($\text{Zn}(\text{Ac})_2 \cdot 2\text{H}_2\text{O}$), diethylene glycol (DEG), tetraethyl orthosilicate (99.999%, TEOS), 3-aminopropyl triethoxysilane (99%, APTES), N-hydroxysuccinimide (NHS), N,N'-Dicyclohexyl carbodiimide (DCC), reagent grade triethylamine, folic acid (97%, FA). Anhydrous ether and dimethyl sulfoxide (DMSO) were sourced from Alfa Aesar. Doxorubicin hydrochloride (>99%, DOX), was purchased from Thermo Fisher Scientific, together with laboratory grade ethanol and acetone.

2.2.2 Synthesis of ZnO template and hS NPs

The synthetic pathway of the investigated NPs is schematically displayed in Figure 2-1. ZnO template NPs were synthesised in a two stage reaction process via the hydrolysis of $\text{Zn}(\text{Ac})_2 \cdot 2\text{H}_2\text{O}$ using a reported method [22] with slight modification. Typically, 6.59 g (0.03 mol) of $\text{Zn}(\text{Ac})_2 \cdot 2\text{H}_2\text{O}$ was added to 300 mL of DEG with stirring and the temperature was raised to 90 °C to assist dissolution. Upon dissolution, the temperature was raised to 160 °C and maintained for 2 h. Upon cooling to room temperature, the product was subject to centrifugation at 7240 x g for 10 min. The polydisperse sediment was discarded and the slightly turbid supernatant was kept for use in the second stage. Stage two began in the same way as stage one: 0.03 mol $\text{Zn}(\text{Ac})_2 \cdot 2\text{H}_2\text{O}$ was added to 300 mL of DEG with stirring and the temperature was raised to 90 °C to assist dissolution. Upon dissolution the temperature was raised to 150 °C at which point a known volume of the primary supernatant was added, drop wise, to the reaction mixture. After addition, the reaction temperature was raised to 160 °C and maintained for 2 h. The reaction was allowed to cool to room temperature and the ZnO NPs were collected via centrifugation and were subject to six washes with milli-Q water in conjunction with ultra-sonication. Particles were stored as a suspension in milli-Q water. The reaction yield was 98.7%.

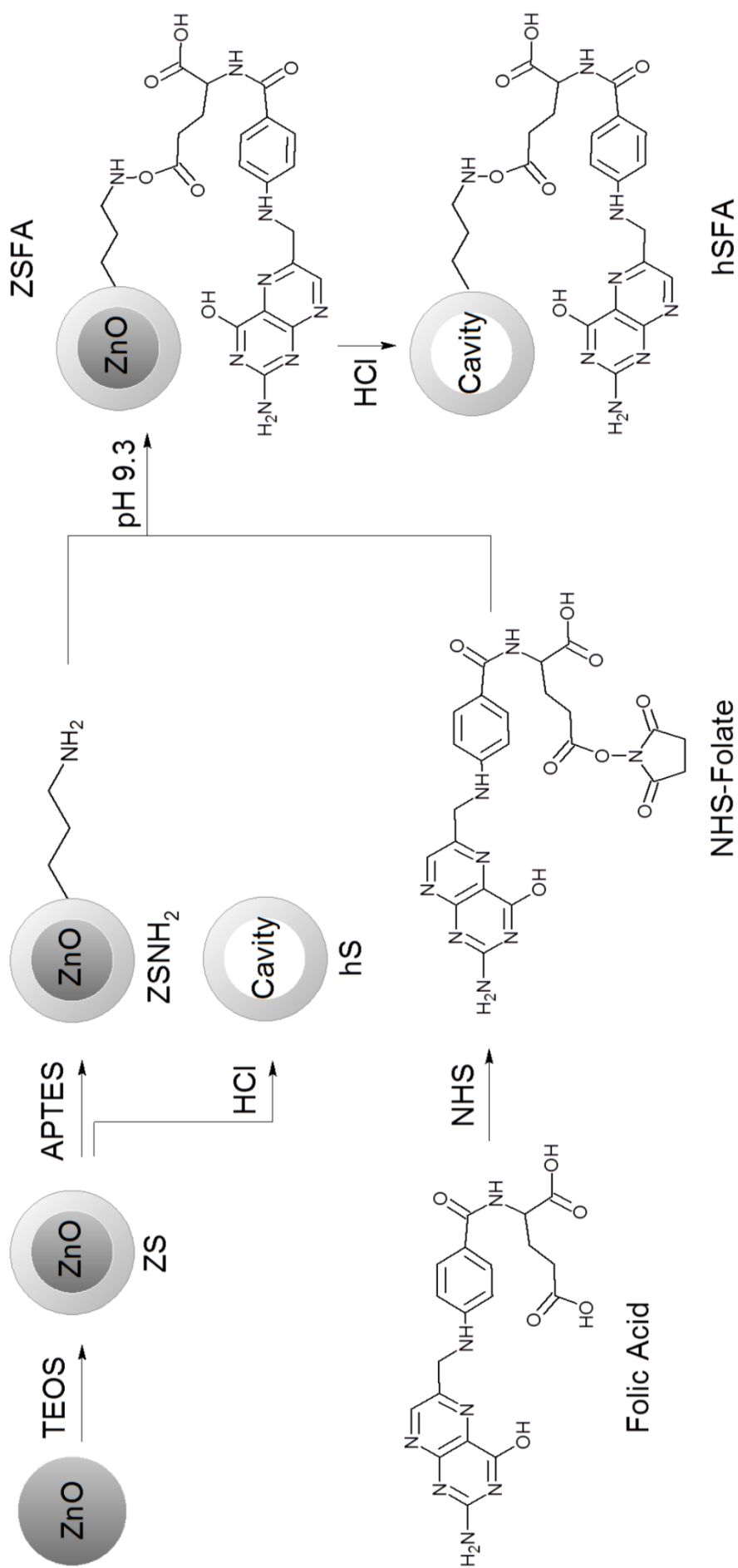


Figure 2-1. A schematic illustration of the synthetic process used to fabricate hollow silica (hS) and folic acid conjugated hollow silica (hSFA) NPs.

Silanisation of the ZnO NPs was achieved through a sol-gel process, employing TEOS [23]. Briefly, 0.5 g (6.14mmol) of ZnO NPs was suspended via ultra-sonication in a mixture of 20 mL ethanol and 20 mL milli-Q water containing 1.1 mL of ammonium hydroxide solution (25 % wt.). A solution of TEOS (0.603 mL, 2.70 mmol) in 10 mL of ethanol was added drop wise to the nanoparticle suspension. The reaction was allowed to proceed at room temperature with magnetic stirring (300 rpm) for 2 h. The produced particles were collected by centrifugation and washed sequentially in ethanol followed by milli-Q water using ultra sonication.

To produce hollow silica (hS) NPs, the above prepared ZnO-SiO₂ (ZS) core shell particles (0.1 g) were dispersed in a hydrochloric acid (HCl) solution (0.25 M, 20 mL) at room temperature with constant stirring for 1 h. The NPs were then collected through centrifugation and treated in the same manner with progressively dilute HCl solutions (0.20 M and 0.1 M) until all ZnO was leached out. The final collected hS NPs were washed with milli-Q water (5 x 50 mL) via centrifugation (20 min, 9163 x g) and stored for further analysis.

2.2.3 Synthesis of hSFA NPs

ZnO NPs were first silanised according to the procedure described above. A subsequent amine functionalisation of the obtained ZS was achieved by the drop-wise addition of APTES (1.264 mL, 5.40 mmol) in 10 mL ethanol to the ZS NP suspension, followed with 2 hours stirring at room temperature. The amine terminated ZS NPs (ZSNH₂) were collected via centrifugation (10 min, 7240 x g) and were washed three times sequentially in ethanol followed by milli-Q water.

At the same time, the NHS ester of FA (NHS-FA) was synthesised via a DCC coupling method reported previously [24]. The synthesised NHS-FA intermediate was used to react with ZSNH₂ in order to produce FA conjugated ZnO-SiO₂ core shell nanoparticles (ZSFA). To do this, 0.1 g of ZSNH₂ NPs were dispersed in 22.5 mL of Na₂CO₃/NaHCO₃ buffer (pH 9.30) using sonication for 10 min. NHS-FA (2.79 mmol) was added drop wise to the NP suspension with constant stirring. After one hour, ZSFA NPs were collected via centrifugation (10 min, 7240 x g) and were washed in conjunction with sonication five times in DMSO followed by 3 times with milli-Q

water. The FA conjugated hollow silica (hSFA) NPs were obtained by leaching of the ZnO using the same procedure discussed in section 2.2.2.

2.2.4 Nanoparticle Characterisation

Transmission and scanning electron micrographs of the produced NPs were obtained using our previously reported method [25]. Geometric particle size analysis was carried out using Gwyddion imaging software. Hydrodynamic particle size and size distribution were further assessed via dynamic light scattering (DLS) using a Zetasizer Nano-ZS from Malvern Instruments. Samples were prepared as NP dispersions in milli-Q water. Size and distribution data were analysed using the Malvern Zetasizer Nano software version 7.0. Size and polydispersity results were reported as the mean \pm standard deviation of triplicate measurements. A Thermo Scientific Nicolet is50 FT-IR spectrometer equipped with a diamond ATR sampling accessory and a Bruker Advance III NMR spectrometer (400 MHz) were used for chemical characterisation. Detailed information can be found in previously reported work [25].

Quantification of the organic moieties bound to the NP surfaces was carried out using thermogravimetric analysis (TGA) (Mettler Toledo). Samples (10 to 15 mg) were heated in air ($0.1 \text{ L}\cdot\text{min}^{-1}$) from an equilibrium temperature of $35 \text{ }^\circ\text{C}$ to $110 \text{ }^\circ\text{C}$ at a rate of $10 \text{ }^\circ\text{C}\cdot\text{min}^{-1}$. The temperature was held at $110 \text{ }^\circ\text{C}$ for 30 min and was then raised to $900 \text{ }^\circ\text{C}$ at a rate of $10 \text{ }^\circ\text{C}\cdot\text{min}^{-1}$. The FA content on the NPs was calculated from the relative mass loss shown by the TGA.

Nitrogen sorption isotherms were measured at 77K on a Micromeritics Tristar 3000 apparatus. Prior to examination NPs were freeze dried at $-65 \text{ }^\circ\text{C}$ (0.0054 mbar) for 18 hours. The specific surface area of the NPs was calculated using the Brunauer–Emmett–Teller (BET) method and the pore size distribution was derived from the adsorption branches of the isotherms based on the Barrett-Joyner-Halenda (BJH) method.

2.2.5 Drug loading and Release

Nanoparticles of hSFA (9-10 mg of) were dispersed in a PBS solution of DOX (2 % wt.) for 18 hours with constant agitation at room temperature and then

separated from the solution via centrifugation (5 min, 9163 x g) and rinsed 4 times with 0.8 mL PBS (pH 7.4) to remove excess drug molecules on the surface. Loading capacity was determined via UV-Vis spectroscopy by subtraction of the drug present in the supernatant and washing media from the total amount of drug in the loading solution. The drug-loaded particles were redispersed in 0.8 mL fresh PBS with slight agitation using an orbital shaker. At allotted periods of time the PBS solution containing released drug was collected via centrifugation and subject to UV-Vis absorbance measurement using a Jasco V-570 UV-Visible diffuse reflectance spectroscope. The particles were resuspended in 0.8 mL of fresh PBS after each sampling stage to maintain sink conditions. Cumulative release percentage was plotted against time and the first 60 % of release was modelled using Equation 2-1 as adapted from the work of Ritger and Peppas [26]:

$$\frac{M_t}{M_\infty} = kt^n \quad \text{Equation 2-1}$$

in which k is a constant, representing the characteristics of the drug and the NP shell's macromolecular network system, while the diffusional exponent n , indicates the mechanism of transport and is constrained by the morphology and geometry of the drug carrier. The value of k and n can be obtained by plotting $\ln \frac{M_t}{M_\infty}$ against $\ln(t)$.

2.2.6 Cell Culture

Caco-2 and 3T3 cells were grown in DMEM-high glucose medium supplemented with 10 % fetal bovine serum, 1 % Penicillin-Streptomycin and 1 % L-glutamine (Sigma-Aldrich). The cells were grown into 96-well plates at a density of 5×10^3 cells per well at 37 °C and under

2.2.7 Cell Viability

A modified acid phosphatase (APH) assay [27] based on quantification of cytosolic acid phosphatase activity, was employed for determining cell viability. Intracellular acid phosphatases in viable cells hydrolyse *p*-nitrophenyl phosphate to *p*-nitrophenol. The absorption of the latter at 405 nm is directly proportional to the cell number in the range of 10^3 to 10^5 monolayer cells. For this work, the investigated

nanoparticle concentrations were 50, 100 and 200 $\mu\text{g}\cdot\text{mL}^{-1}$. Free DOX was used at 0.5 $\mu\text{g}\cdot\text{mL}^{-1}$. DOX loaded hSFA(215) at a NP concentration of 50 $\mu\text{g}\cdot\text{mL}^{-1}$ was also used. The nanoparticles were suspended in growth medium using an ultrasonic bath for 15 minutes before treatment of cells. A control experiment was performed using the cells treated with complete medium containing no NPs, under identical conditions. Cells were incubated with the NPs for 6 h and 24 h, respectively, prior to the APH assessment. At testing time, the culture medium was removed, and the cells were rinsed once with PBS. Then, 100 μL of the assay buffer (0.1 M sodium acetate, 0.1% Triton-X-100, supplemented with ImmunoPure p-nitrophenyl phosphate; Sigma-Aldrich) was added to each well and incubated for 90 min at 37 °C. Following incubation, 10 μL of 1 M sodium hydroxide (NaOH) was supplemented to each well, and absorption at 405 nm was measured within 10 min on an Enspire Multimode plate reader (PerkinElmer). The relative cell viability was estimated by $A_{\text{test}}/A_{\text{control}}$, where A_{test} and A_{control} are the absorbance of the produced p-nitrophenol by samples and controls, respectively.

2.2.8 Statistical Analysis

All experiments were repeated three times under identical conditions. The results were expressed as mean \pm standard error of the mean (SEM); where $\text{SEM} = \frac{SD}{\sqrt{n}}$, and SD is the standard deviation. All data were analysed using two-way-ANOVA, via Dunnett's multiple comparisons test and Tukey's multiple comparisons test (GraphPad Prism 6). Statistical significance was considered at $P < 0.05$.

2.3 Results and Discussion

2.3.1 Characterisation of NHS-FA

The successful synthesis of NHS-FA was confirmed both by FTIR (Figure 2-2a) and by ^1H NMR (Figure 2-2b). From Figure 2-2a the peak at 1687 cm^{-1} in the FA FTIR spectrum was attributable to the C=O stretching vibration of the carboxyl group, and that at 1638 cm^{-1} , was ascribed to the carbonyl stretching vibration of the –CO–HN (amide band II) group from the L-glutamic acid moiety [25, 28]; both peaks were blue shifted to 1698 cm^{-1} and 1647 cm^{-1} respectively upon activation to form NHS-FA.

Notably new peaks at 1201 cm^{-1} and 1068 cm^{-1} in the NHS-FA spectrum were respectively ascribed to the C–O and N–O stretching vibration of the newly formed succinimidyl ester group [25, 29]. Furthermore, the strong peak at 1729 cm^{-1} was ascribed to splitting of the band associated with the carbonyl stretching vibration of the newly formed succinimidyl ester group [25, 30]. The peaks seen at 1814 and 1872 cm^{-1} were related to the C=O stretching vibration of the succinimidyl carbonyl groups also [25, 30].

For ^1H NMR analysis (Figure 2-2b), the signals at 2.50 and 3.30 ppm correspond to the DMSO- d_6 solvent and water respectively. The signals at 8.65, 7.64 and 6.65 ppm are attributed to the aromatic protons of FA, labelled **a**, **c** and **e** respectively [25, 31]. The signals at 8.13 and 7.00, labelled **b** and **d** correspond to protons of the –CO–NH– group in the glutamate moiety and the –NH– group in the p-amino benzoic acid moiety of FA respectively [25, 32]. Methylene protons of the FA glutamate moiety are labelled **f**, **h**, and **i** and appear at signals of 4.48, 2.31 and 1.99–2.10 ppm respectively, while a new peak corresponding to the methyl protons of NHS appeared at 2.80 ppm in the NHS-FA spectrum (labelled **j**) indicating successful conversion of FA to NHS-FA [25, 33]. Integration of peak **j** revealed a higher stoichiometric value of 6.40 H as compared to 4 H, most likely attributed to the presence of unreacted NHS. It must be noted that the presence of the unreacted NHS impurity was not found to interfere in progressive stages of NP synthesis. Integration of proton resonances **g** (methine proton in the glutamate portion of FA) and **h** showed a respective diminution of ~ 74 and $\sim 10\%$ respectively, this observation is consistent with NHS ester formation at the α and γ carboxylates of FA, providing further confirmation of successful activation of FA. A similar result was obtained by Alexander et al. [33]. Note that the FA molecule contains two carboxylate groups, termed α and γ at which conjugation can occur (Figure 2-2b).

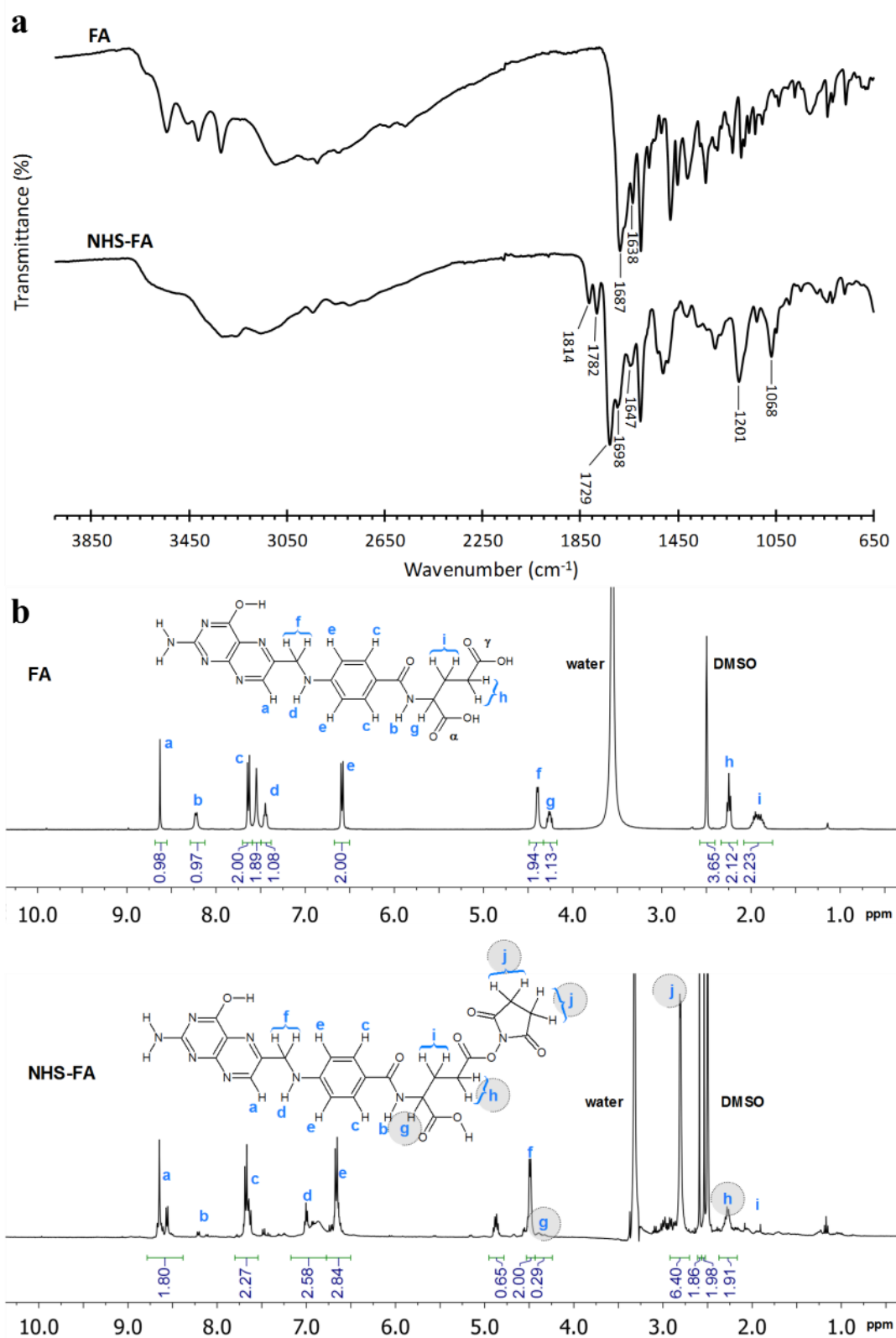


Figure 2-2. (a) FTIR and (b) ^1H NMR spectra, both detailing the activation of FA to NHS-FA. The γ isomer of NHS-FA is shown in (b).

2.3.2 Characterisation of synthesised NPs

In this study, ZnO NPs of distinct sizes (215 ± 15 nm and 430 ± 21 nm) were synthesised and were termed Z(215) and Z(430) respectively. Subsequently, the silanised ZnO core-shell structures were termed ZS(215) and ZS(430), folate conjugated particles ZSFA(215) and ZSFA(430) and the corresponding hollow counterparts hS(215), hS(430), hSFA(215) and hSFA(430). SEM and TEM micrographs of selected NPs are shown in Figure 2-3. The measured diameters of these particles are summarised in Table 2-1. The nanocrystallite structural morphology of the ZnO templates, clearly visible in Figure 2-3a (centre), is typified by their seeded growth. Particle size distribution was narrow as seen in Figure 2-3a (left) and was confirmed by obtaining polydispersity indices (PDIs) below 0.1 via DLS (Table 2-1). Silanisation and FA modification was evident as a smoothing of the particle surfaces as per Figure 2-3a (right) and also resulted in an increase in size and PDI. Shell thickness of the hSFA NPs was measured post leaching of the ZnO cores using TEM and was found to be 11.4 ± 1.2 nm and 38.6 ± 3.1 nm respectively for hSFA(215) (Figure 2-3b, left) and hSFA(430) (Figure 2-3b, right). Larger particle diameters obtained via DLS were attributed to measurement of the hydrodynamic diameter, known to be larger than the geometric diameter measured via SEM and TEM [34] as seen in our previous work also [35]. The average particle size decreased upon removal of the ZnO cores. An average reduction in diameter by 19.5 and 21.2 % respectively for the smaller and larger sets of hollow particles was observed collectively through all three methods. This could be explained by strain present in the silica shell due to presence of the core. Removal of the core leads to the relaxation of the hollow NPs therefore resulting in a reduced size. An estimation of the silica cavity volume per unit mass based on the shell thickness and radius, yielded $1.00 \text{ cm}^3.\text{g}^{-1}$ and $0.48 \text{ cm}^3.\text{g}^{-1}$ for hSFA(215) and hSFA(430) respectively.

Table 2-1. Size and size distribution of NPs

Method	Nanoparticle Size, nm							
	Z(215)	Z(430)	ZSFA(215)	ZSFA(430)	hS(215)	hS(430)	hSFA(215)	hSFA(430)
DLS ^a	243 ± 7	472 ± 4	262 ± 14	539 ± 18	214 ± 7	409 ± 11	210 ± 26	422 ± 21
PDI	0.076	0.071	0.252	0.204	0.301	0.298	0.241	0.267
SEM ^b	215 ± 15	430 ± 21	234 ± 13	494 ± 22	179 ± 16	397 ± 20	188 ± 14	391 ± 19
TEM ^c	211 ± 15	427 ± 20	230 ± 14	496 ± 22	182 ± 20	394 ± 17	186 ± 9	391 ± 16

Values represent mean ± SD where ^an = 3 measurements, ^bn = 200 particles, ^cn = 50 particles.

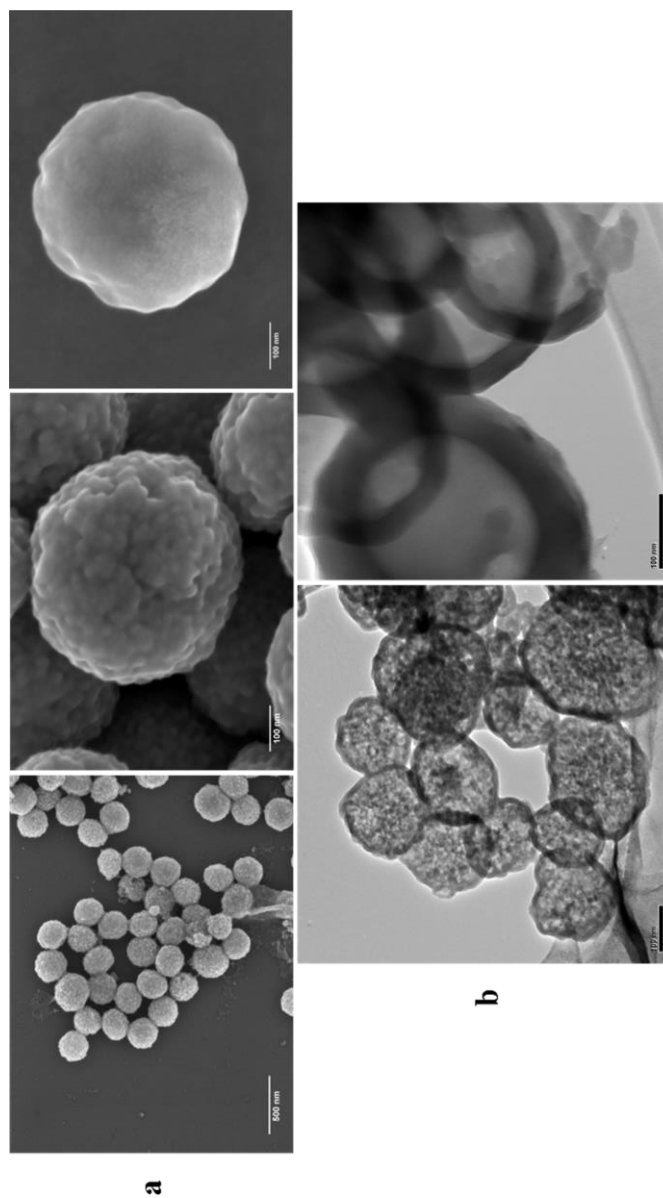


Figure 2-3. (a) SEM micrographs of Z(215) (left), Z(430) (center), ZSFA(430) (right) and (b) TEM micrographs of hSFA(215) (left) and hSFA(430) (right).

FTIR spectra of the synthesised NPs are displayed in Figure 2-4a. For ZnO, the strong characteristic absorption band at 370 cm^{-1} was attributed to the Zn–O stretching vibration and agrees well with literature [36, 37]. Silanisation of the nanoparticles was successfully confirmed via the presence of a strong absorption band between $1000\text{--}1200\text{ cm}^{-1}$ ascribed to the asymmetric bending and stretching vibration modes of siloxane groups [38]. Additionally the weak absorption band at 795 cm^{-1} was attributed to the formation of the Zn–O–Si linkage between the ZnO core and silica shell, this linkage also resulted in a blue shift of the Zn–O stretching vibration band from 370 to 410 cm^{-1} . The broad peak present in all spectra at 3350 cm^{-1} was attributed to the O–H stretching vibration due to adsorbed water and in the spectra of ZSNH₂, ZSFA and hSFA this peak saw an additional contribution from the O–H stretching vibration of surface silanol groups. Amine functionalisation of the silica shell was elucidated by the appearance of relatively weak bands at 2929 cm^{-1} and 2857 cm^{-1} assigned to the C–H stretching mode of the n-propyl chain. In addition, the weak absorption band at 1624 cm^{-1} indicated the presence of NH₂ through deformation modes of NH₂ and NH³⁺ groups [25, 39]. Furthermore, the weak band at 1468 cm^{-1} , was attributed to the symmetric deformation mode of NH³⁺ and the weak bands at 1451 and 1416 cm^{-1} assigned to the CH₂ deformation mode of the n-propyl chain for bound APTES. FA conjugation was confirmed by newly formed amide bonds in the spectra of ZSFA; highlighted by the appearance of peaks at 1576 cm^{-1} and 1538 cm^{-1} , corresponding respectively to the C–N and N–H bending modes of the amide band II as well as the appearance of a weak band at 3323 cm^{-1} corresponding to the N–H stretching vibration [25, 39]. Expansion of the region between 1300 and 1700 cm^{-1} (Figure 2-4a, right) more clearly illustrates spectral differences upon FA conjugation. The peak at 1622 cm^{-1} saw an increase in intensity due to the characteristic C=O stretching vibration of amide band I. Furthermore, the appearance of a shoulder at 1609 cm^{-1} , corresponding to the N–H bending vibration both provided further confirmation of FA conjugation. Leaching of the ZnO templates resulted in a diminution of the band corresponding to the Zn–O stretching vibration at 370 cm^{-1} and also allowed for the resolution of several shielded peaks in the spectra of hSFA below 900 cm^{-1} which were ascribed to various vibration modes of the pterin ring moiety of FA [38].

TGA of ZSFA(430) (Figure 2-4b, Left) revealed a two stage mass loss that occurred respectively between 35 and 110 °C, attributed to the release of adsorbed water molecules, and between 110 and 850 °C, owing to the decomposition of organic moieties grafted to the particle surfaces. The density of FA attached on the NP surface was determined by difference of mass loss between ZSFA and its precursor ZSNH₂ and was found to be 0.12 mmol.g⁻¹ for ZSFA(430). Similar analysis was carried out for ZSFA(215), indicating 0.20 mmol.g⁻¹ of FA incorporated on the surface of the smaller sized NPs. The average particle size was used to determine the density of FA on the surfaces of the NPs and was found to be approximately 1.16 and 1.09 FA molecules per nm² for ZSFA(215) and ZSFA(430) respectively. The similarity in FA density was expected as the amount of FA precursor used in the synthesis stage was controlled to account for variation in NP surface area.

BET and BJH methods allowed elucidation of surface area, pore size and pore volume of ZSFA(215), ZSFA(430), their hollow counterparts and DOX loaded NPs (DOX-hSFA(215)). The results are summarised in Table 2-2 below. The increase in surface area and pore volume upon hollowing of ZSFA NPs to produce hSFA particles, evident in both sized NPs, is indicative of the formation of the hollow cavity due to an increase in N₂ adsorption. No significant change was evident in the pore size upon hollowing of the NPs, further indicating that the increase in pore volume must have been due to the formation of the hollow cavity. The results for DOX loaded particles are discussed in subsequent sections.

Table 2-2. Surface area, pore volume and pore size data obtained from BET and BJH nitrogen sorption experiments.

	ZSFA(215)	ZSFA(430)	hSFA(215)	hSFA(430)	DOX-hSFA(215)
BET/BJH property					
Surface Area (m ² .g ⁻¹)	104	66	187	90	50
Pore Volume (cm ³ .g ⁻¹)	0.31	0.14	0.68	0.36	0.20
Pore Size (nm)	10.3	11.6	10.5	11.7	0.3

UV-Visible absorbance spectra are shown in Figure 2-4b (right). The absorbance peaks at 269 nm and 279 nm in the spectra of hSFA and ZSFA particles respectively, are blue shifted from the 285 nm absorbance peak of free FA. This peak is assigned to the $\pi \rightarrow \pi^*$ orbital transition associated with the pterin ring of the FA molecule and

confirms the presence of conjugated FA on the particle surfaces. The broad absorbance in the visible region of ZnO and ZSFA can be attributed to light scattering caused by the suspended NPs. The characteristic absorbance peak at wavelength 370 nm was assigned to the intrinsic band-gap absorbance of ZnO and is due to electron transitions from the valence band to the conduction band ($O_{2p} \rightarrow Zn_{3d}$). This peak is discernible in the ZSFA spectra, but is not present in the spectra of hSFA suggesting the successful leaching of ZnO templates. Furthermore, the broad absorbance in the visible range above 400 nm was seen to diminish considerably upon removal of the ZnO cores due to a reduction in the scattering of incident light, also suggesting a successful leaching process.

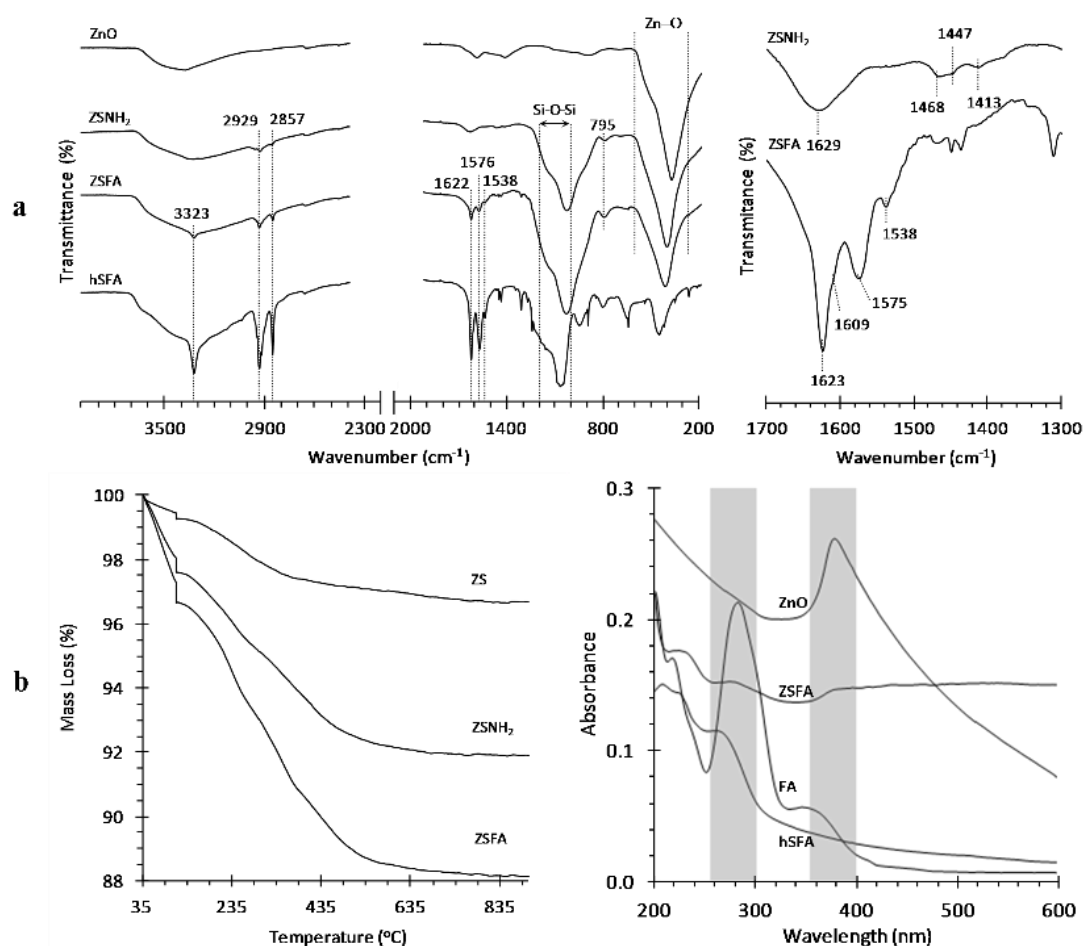


Figure 2-4. (a) FTIR spectra, (b) TGA curves (left) and UV-Vis spectra (right) for various NPs.

Removal of ZnO was confirmed through ICP-OES analysis (PerkinElmer Optima 8300 ICP-OES spectrometer). The core shell NPs were subject to a three stage leaching process with the concentration of the HCl leaching solution decreasing with

each progressive stage. Quantification of zinc content via axial and radial ICP-OES measurements of leaching solution in stage 2 was 0.001 mg.L^{-1} for hSFA(215) and 0.002 mg.L^{-1} for hSFA(430). For leaching solution at stage 3, there was no detectable amount of zinc ions. The final hollow particles were also tested for zinc content and showed $\leq 0.013 \text{ mg.L}^{-1}$ of zinc.

2.3.3 Drug loading and release studies

DOX loaded particles were also subject to BET/BJH analysis to elucidate whether the drug was adsorbed on the surface or within the hollow cavity. As per Table 2-2, DOX-hSFA(215) NPs were found to have a significantly lower specific surface area and pore volume when compared to unloaded hSFA(215) NPs. Furthermore, the pore size of the DOX loaded particles was considerably smaller than that of the unloaded counterparts. These results indicate a filling of the hollow cavity and pores by the drug molecules resulting in smaller amounts of N_2 adsorption. Such a reduction in surface area, pore volume and pore size upon drug loading of hollow silica NPs has also been reported in other studies [40].

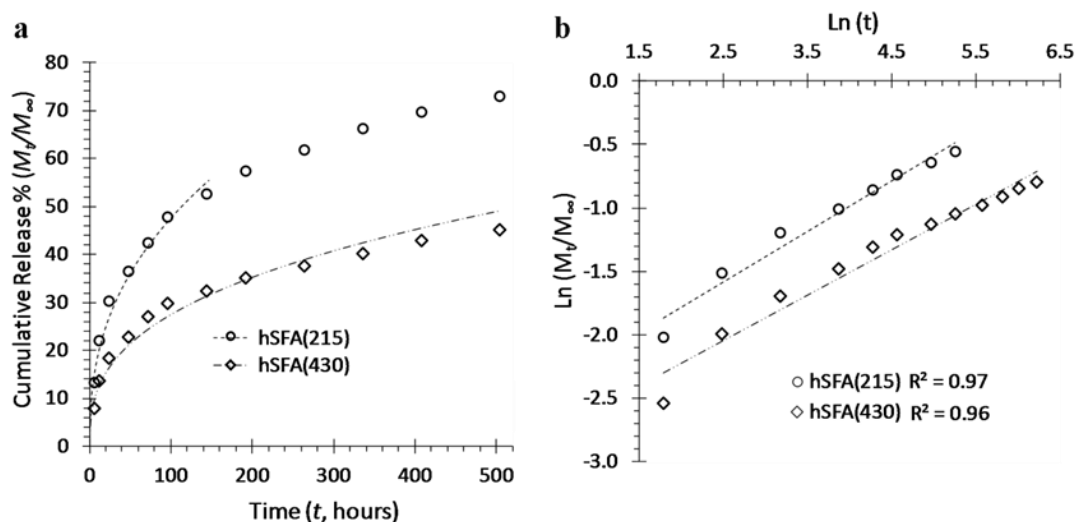


Figure 2-5. (a) Release profiles of DOX, and (b) the corresponding linear fitting using Equation 2-1.

The DOX loading capacity was 28.6 mg.g^{-1} for hSFA(215) and 17.4 mg.g^{-1} for hSFA(430). This difference is likely due to variation in cavity volume between the two types of particles as mentioned in section 3.1. The release was measured over a period of 21 days with sampling at various time intervals. The cumulative release

versus time is displayed in Figure 2-5a, showing a drug burst at early times and a marked retardation of drug transport for longer times for both sets of samples; a typical diffusion driven release. Greater release of DOX was observed from the smaller particles at all times due to their larger surface to volume ratio. For hSFA(215), the cumulative release reached just above 60% at 11 days. However, for hSFA(430), the cumulative release only reached 45% within the monitored time period 21 days. Modelling of the first 60% of release data using Equation 2-1 resulted in n values of 0.40 and 0.36 for hSFA(215) and hSFA(430) respectively, with R^2 correlation coefficients of 0.97 for hSFA(215) and 0.96 for hSFA(430). According to Ritger and Peppas [20], for spherical and mono-disperse particles the diffusional exponent n , is expected to take on the limits: $n = 0.43$ for Fickian diffusion, $0.43 < n < 1$ for anomalous diffusion and $n = 1.00$ for time independent zero order diffusion. In this study, the n values for both particle sizes were smaller than 0.43, which is likely due to the polydisperse nature of the particles under investigation [26].

It is worth noting that liposomal DOX is clinically used in the treatment of various cancers with dosage varying from 10 to 50 $\text{mg}\cdot\text{m}^{-2}$ depending on the disease and patient prognosis [41]. A study by Amantea et al. [42] using DOX, involving 43 patients showed that an average C_{max} value of $0.40 \mu\text{g}\cdot\text{mL}^{-1}\cdot\text{day}^{-1}$ and a dose intensity of $0.7 \text{mg}\cdot\text{m}^{-2}\cdot\text{day}^{-1}$ ($30 \text{mg}\cdot\text{m}^{-2}$ every three weeks) were the minimum requirements to achieve significant decrease in tumour size. As such, for the cell viability study conducted in this work, DOX loaded hSFA(215) NPs were used at a concentration of $50 \mu\text{g}\cdot\text{mL}^{-1}$, corresponding to approximately $0.5 \mu\text{g}\cdot\text{mL}^{-1}$ of released DOX at 24 h. Free DOX at a concentration of $0.5 \mu\text{g}\cdot\text{mL}^{-1}$ was also investigated for comparison.

2.3.4 Cell viability study

Cell viability was assessed after 3T3 and Caco-2 cells were incubated with different NPs at various concentrations. No significant change was observed in the viability of 3T3 cells at 6 h, however, comparatively, Caco-2 cells did show a toxic response to all NPs after a 6 h exposure period (Figure 2-6) with cell viability dropping to as low as 56 % for hS(430) at a concentration of $200 \mu\text{g}\cdot\text{mL}^{-1}$. Responses of both cell lines changed significantly when prolonging exposure to 24 h (Figure 2-6). Significant toxic responses were observed in both cell lines at all investigated

concentrations regardless of the nanoparticle sizes, except for 3T3 cells treated with $50 \mu\text{g}\cdot\text{mL}^{-1}$ hS(215) or hS(430) (Figure 2-6). An apparent concentration dependence was well demonstrated (Figure 2-6 inserts). In comparison to 3T3 cells, the viability of Caco-2 cells at 24 h was more significantly reduced at all nanoparticle concentrations, and dropped to as low as 42 % for hS(430) and 44 % for hS(215) at a concentration of $200 \mu\text{g}\cdot\text{mL}^{-1}$ (Figure 2-6). The results from this study clearly demonstrated a selective toxicity of the hollow silica NPs towards Caco-2 cells. At 24 h, the cell viability was reduced to 66 % and 94 % respectively for Caco-2 and 3T3 cells when $50 \mu\text{g}\cdot\text{mL}^{-1}$ of hS(215) was used (Figure 2-7a). Increasing the NP concentration to $200 \mu\text{g}\cdot\text{mL}^{-1}$ saw the viability reduce to 44 % for Caco-2 and 81 % for 3T3. The results from the larger nanoparticles, hS(430), showed a similar concentration dependence as displayed in the inserts of Figure 2-6.

As mentioned previously, recent studies on hollow silica NPs have reported biocompatibility with various cell lines. Results from this work however, clearly indicate that toxicity induced by hollow silica NPs is dependent on the type of cell line used, time of exposure and concentration of NPs. These findings are analogous to research that has emerged in the past decade utilising solid silica NPs. Further investigations are needed to draw parallel conclusions between hollow and solid silica NPs regarding ROS generation, cell membrane integrity and other cell specific mechanistic driving forces for NP induced toxicity [20, 21].

The influence of DOX on cell viability was also assessed in both its free and encapsulated form. Free DOX had a similar effect in both cell lines with viability dropping to 72 % (3T3) and 80 % (Caco-2) at a concentration of $0.5 \mu\text{g}\cdot\text{mL}^{-1}$ (Figure 2-7b). Encapsulated DOX reduced 3T3 cell viability to 83 %, however with Caco-2 cells the viability diminished to 45% at an equivalent DOX concentration of $0.5 \mu\text{g}\cdot\text{mL}^{-1}$. A pronounced selectivity towards Caco-2 cells by hollow silica NPs was once again demonstrated. When comparing Caco-2 cell viability, encapsulation of DOX within the silica shell obviously served to further reduce cell viability, as seen with other studies [43, 44]. It is known that the Caco-2 cell line is rich with the folate binding protein gp38, and p-glycoprotein (PgP) energy-dependent efflux pumps whereas 3T3 is not [45-47]. The presence of PgP pumps reduces the cytotoxic effect of DOX on cancer cells [45], which explains the difference seen in the cell viability data between

3T3 and Caco-2 cells, i.e., the use of DOX loaded NPs bypassed the PgP pumps, prevented the reduction effect on the toxicity. Furthermore, conjugation with FA may have facilitated the cell uptake of NPs, as demonstrated by the enhanced cell growth in the absence of DOX (Figure 2-7b), leading to enhanced toxicity towards to Caco-2 cells.

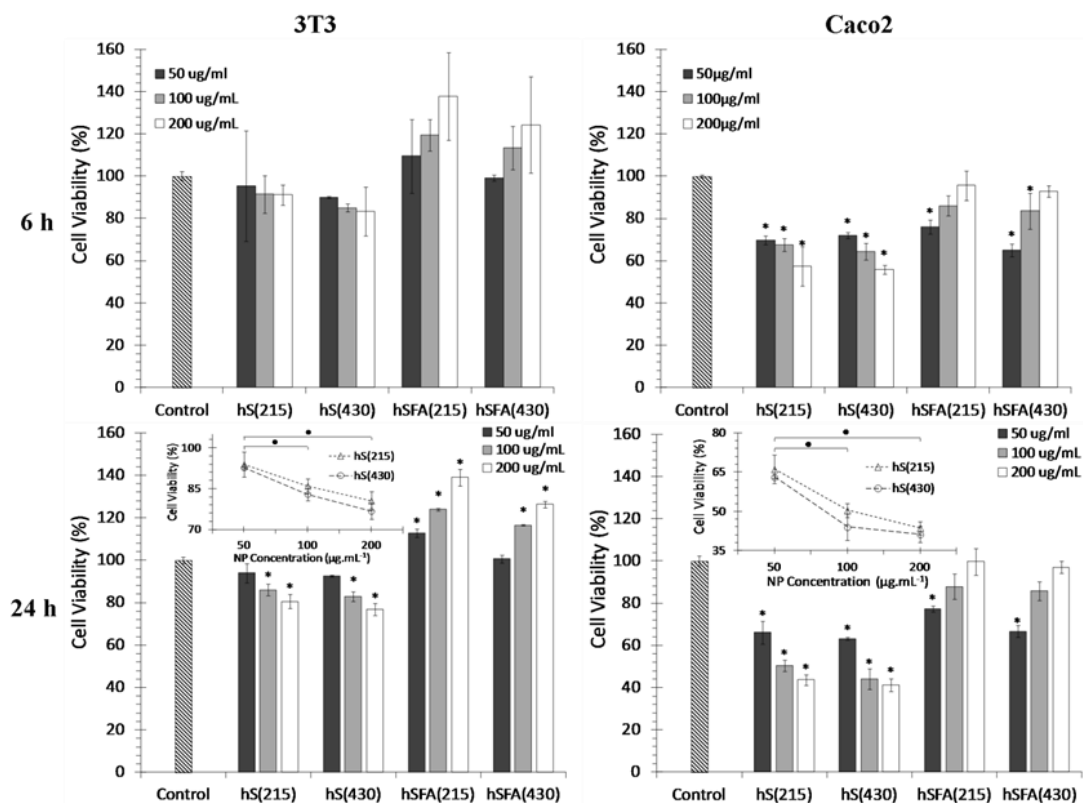


Figure 2-6. Viability of 3T3 and Caco-2 cells at $t = 6$ h and $t = 24$ h. All data are represented as mean \pm SEM with $n = 3$. Inserts in (c) and (d) show concentration dependence of cell viability for hS(215) and hS(430) NPs. * and • denote $P < 0.05$.

It is noteworthy that the presence of conjugated folate on the hollow silica spheres enhanced the growth of 3T3 cells (Figure 2-6). The enhancement was also seen in the Caco-2 cells, however the effect was less obvious due to toxicity associated with the hollow silica (Figure 2-6). This observation, coupled with our previously reported results using L929 and KB cells with FA conjugated titanium dioxide NPs [25], indicates folate conjugation supplements the growth of cells. The enhancement in viability due to FA was seen to increase with hSFA NP concentration (Figure 2-6), indicating the concentration dependence of surface bound FA. A more comprehensive interrogation of the relationship between folate concentration and

cancer cell viability would well supplement the scientific literature in this field. The cell selectivity of pure hollow silica NPs is also an on-going topic of the investigation.

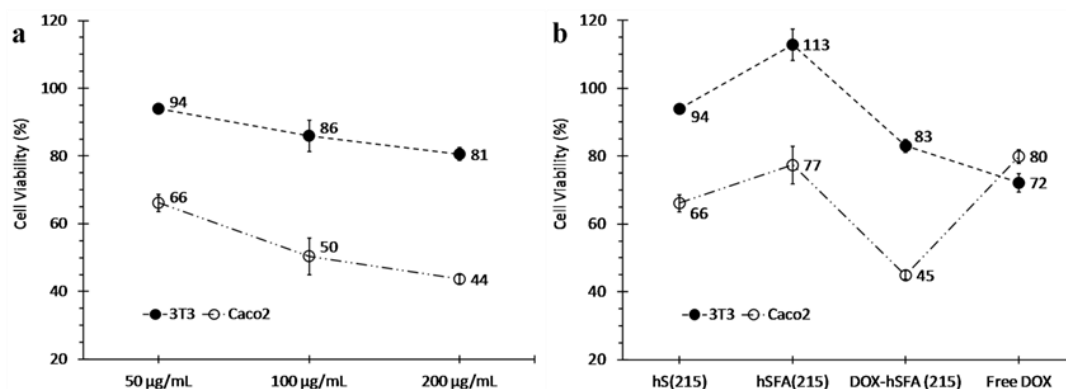


Figure 2-7. (a) Viability of 3T3 and Caco-2 cells at $t = 24$ h upon treatment with hS(215) at various concentrations. (b) Influence of free and encapsulated DOX ($0.5 \mu\text{g.mL}^{-1}$) on 3T3 and Caco-2 cell viability at $t = 24$ h. NP concentration was $50 \mu\text{g.mL}^{-1}$. All data are represented as mean \pm SEM with $n = 3$. Note: dotted lines are used for visual emphasis of cell specificity and do not signify any correlation between NPs.

2.4 Conclusions

Hollow silica nanoparticles of two sizes (215 ± 15 nm and 430 ± 21 nm) and their folic acid conjugated counterparts were synthesized using a facile approach, with confirmation through the use of a physiochemical characterisation scheme. Investigation of drug loading and release properties revealed the drug carrier's ability to discharge the chemotherapeutic agent DOX via Fickian diffusion. Cell viability studies showed hollow silica particle inherent toxicity, selective to Caco-2 cancer cells over 3T3 cells. The selectivity was not limited to folate conjugated NPs, but was also observed through use of the pure hollow silica itself. Cell toxicity was further enhanced via encapsulation of DOX by the NPs, also showing a significant advantage over the free drug upon treatment of Caco-2 cells. FA targeting ligands were found to increase the viability of both cell lines and as such, optimisation of folate content must be a consideration in the synthesis of future systems. A systematic investigation of the relationship between FA content and cell viability is currently underway. So is the study of the selective toxicity of the synthesised hollow silica nanoparticles towards a greater range of cancerous cell lines.

2.5 References

- [1] A. Liberman, N. Mendez, W.C. Trogler, A.C. Kummel, Synthesis and surface functionalization of silica nanoparticles for nanomedicine, *Surface Science Reports* 69(2–3) (2014) 132-158.
- [2] K.E. Sapsford, W.R. Algar, L. Berti, K.B. Gemmill, B.J. Casey, E. Oh, M.H. Stewart, I.L. Medintz, Functionalizing Nanoparticles with Biological Molecules: Developing Chemistries that Facilitate Nanotechnology, *Chemical Reviews* 113(3) (2013) 1904-2074.
- [3] S. Chen, S. Hayakawa, Y. Shirosaki, N. Hanagata, A. Osaka, Biomedical Applications of Sol-Gel Nanocomposites, in: M. Guglielmi, G. Kickelbick, A. Martucci (Eds.) *Sol-Gel Nanocomposites*, Springer New York, New York, 2014, pp. 167-190.
- [4] M. Benezra, O. Penate-Medina, P.B. Zanzonico, D. Schaer, H. Ow, A. Burns, E. DeStanchina, V. Longo, E. Herz, S. Iyer, J. Wolchok, S.M. Larson, U. Wiesner, M.S. Bradbury, Multimodal silica nanoparticles are effective cancer-targeted probes in a model of human melanoma, *The Journal of Clinical Investigation* 121(7) (2011) 2768-2780.
- [5] A.A. Burns, J. Vider, H. Ow, E. Herz, O. Penate-Medina, M. Baumgart, S.M. Larson, U. Wiesner, M. Bradbury, Fluorescent Silica Nanoparticles with Efficient Urinary Excretion for Nanomedicine, *Nano Letters* 9(1) (2009) 442-448.
- [6] I. Brigger, C. Dubernet, P. Couvreur, Nanoparticles in cancer therapy and diagnosis, *Advanced Drug Delivery Reviews* 64, Supplement(0) (2012) 24-36.
- [7] L. Jia, J. Shen, Z. Li, D. Zhang, Q. Zhang, G. Liu, D. Zheng, X. Tian, In vitro and in vivo evaluation of paclitaxel-loaded mesoporous silica nanoparticles with three pore sizes, *International Journal of Pharmaceutics* 445(1–2) (2013) 12-19.
- [8] H. Meng, M. Wang, H. Liu, X. Liu, A. Situ, B. Wu, Z. Ji, C.H. Chang, A.E. Nel, Use of a Lipid-Coated Mesoporous Silica Nanoparticle Platform for Synergistic Gemcitabine and Paclitaxel Delivery to Human Pancreatic Cancer in Mice, *ACS Nano* 9(4) (2015) 3540-3557.
- [9] J. Shen, G. Song, M. An, X. Li, N. Wu, K. Ruan, J. Hu, R. Hu, The use of hollow mesoporous silica nanospheres to encapsulate bortezomib and improve efficacy for non-small cell lung cancer therapy, *Biomaterials* 35(1) (2014) 316-326.
- [10] G.Q. Silveira, R.S. da Silva, L.P. Franco, M.D. Vargas, C.M. Ronconi, Redox-responsive nanoreservoirs: The effect of different types of mesoporous silica on the controlled release of doxorubicin in solution and in vitro, *Microporous and Mesoporous Materials* 206(0) (2015) 226-233.
- [11] H. Meng, W.X. Mai, H. Zhang, M. Xue, T. Xia, S. Lin, X. Wang, Y. Zhao, Z. Ji, J.I. Zink, A.E. Nel, Codelivery of an Optimal Drug/siRNA Combination Using Mesoporous Silica Nanoparticles To Overcome Drug Resistance in Breast Cancer in Vitro and in Vivo, *ACS Nano* 7(2) (2013) 994-1005.
- [12] L. Tan, T. Liu, L. Li, H. Liu, X. Wu, F. Gao, X. He, X. Meng, D. Chen, F. Tang, Uniform double-shelled silica hollow spheres: acid/base selective-etching synthesis and their drug delivery application, *RSC Advances* 3(16) (2013) 5649-5655.
- [13] Z. Zhao, H. Zhang, X. Chi, H. Li, Z. Yin, D. Huang, X. Wang, J. Gao, Silica nanovehicles endow arsenic trioxide with an ability to effectively treat cancer cells and solid tumors, *Journal of Materials Chemistry B* 2(37) (2014) 6313-6323.
- [14] J. Fu, Y. Zhu, Y. Zhao, Controlled free radical generation against tumor cells by pH-responsive mesoporous silica nanocomposite, *Journal of Materials Chemistry B* 2(22) (2014) 3538-3548.
- [15] S.-J. Choi, J.-M. Oh, J.-H. Choy, Toxicological effects of inorganic nanoparticles on human lung cancer A549 cells, *Journal of Inorganic Biochemistry* 103(3) (2009) 463-471.
- [16] W. Lin, Y.-w. Huang, X.-D. Zhou, Y. Ma, In vitro toxicity of silica nanoparticles in human lung cancer cells, *Toxicology and Applied Pharmacology* 217(3) (2006) 252-259.

- [17] Y. Wu, W. Tang, P. Wang, C. Liu, Y. Yuan, J. Qian, Cytotoxicity and Cellular Uptake of Amorphous Silica Nanoparticles in Human Cancer Cells, *Particle & Particle Systems Characterization* 32(7) (2015) 779-787.
- [18] J.-S. Chang, K.L.B. Chang, D.-F. Hwang, Z.-L. Kong, In Vitro Cytotoxicity of Silica Nanoparticles at High Concentrations Strongly Depends on the Metabolic Activity Type of the Cell Line, *Environmental Science & Technology* 41(6) (2007) 2064-2068.
- [19] L. Gonzalez, M. Lukamowicz-Rajska, L.C.J. Thomassen, C.E.A. Kirschhock, L. Leyns, D. Lison, J.A. Martens, A. Elhajouji, M. Kirsch-Volders, Co-assessment of cell cycle and micronucleus frequencies demonstrates the influence of serum on the in vitro genotoxic response to amorphous monodisperse silica nanoparticles of varying sizes, *Nanotoxicology* 8(8) (2014) 876-884.
- [20] I.-Y. Kim, E. Joachim, H. Choi, K. Kim, Toxicity of silica nanoparticles depends on size, dose, and cell type, *Nanomedicine: Nanotechnology, Biology and Medicine* 11(6) (2015) 1407-1416.
- [21] Y. Yu, J. Duan, Y. Li, Y. Yu, M. Jin, C. Li, Y. Wang, Z. Sun, Combined toxicity of amorphous silica nanoparticles and methylmercury to human lung epithelial cells, *Ecotoxicology and Environmental Safety* 112 (2015) 144-152.
- [22] E.W. Seelig, B. Tang, A. Yamilov, H. Cao, R.P.H. Chang, Self-assembled 3D photonic crystals from ZnO colloidal spheres, *Materials Chemistry and Physics* 80(1) (2003) 257-263.
- [23] W. Stöber, A. Fink, E. Bohn, Controlled growth of monodisperse silica spheres in the micron size range, *Journal of Colloid and Interface Science* 26(1) (1968) 62-69.
- [24] R.J. Lee, P.S. Low, Delivery of liposomes into cultured KB cells via folate receptor-mediated endocytosis, *Journal of Biological Chemistry* 269(5) (1994) 3198-3204.
- [25] X. Feng, S. Zhang, H. Wu, X. Lou, A novel folic acid-conjugated TiO₂-SiO₂ photosensitizer for cancer targeting in photodynamic therapy, *Colloids and Surfaces B: Biointerfaces* 125(0) (2015) 197-205.
- [26] P.L. Ritger, N.A. Peppas, A simple equation for description of solute release I. Fickian and non-fickian release from non-swellable devices in the form of slabs, spheres, cylinders or discs, *Journal of Controlled Release* 5(1) (1987) 23-36.
- [27] J. Friedrich, W. Eder, J. Castaneda, M. Doss, E. Huber, R. Ebner, L.A. Kunz-Schughart, A Reliable Tool to Determine Cell Viability in Complex 3-D Culture: The Acid Phosphatase Assay, *Journal of Biomolecular Screening* 12(7) (2007) 925-937.
- [28] J. Zhang, S. Rana, R.S. Srivastava, R.D.K. Misra, On the chemical synthesis and drug delivery response of folate receptor-activated, polyethylene glycol-functionalized magnetite nanoparticles, *Acta Biomaterialia* 4(1) (2008) 40-48.
- [29] P. Wagner, M. Hegner, P. Kern, F. Zaugg, G. Semenza, Covalent immobilization of native biomolecules onto Au(111) via N-hydroxysuccinimide ester functionalized self-assembled monolayers for scanning probe microscopy, *Biophysical Journal* 70(5) (1996) 2052-2066.
- [30] B. Dordi, H. Schönherr, G.J. Vancso, Reactivity in the Confinement of Self-Assembled Monolayers: Chain Length Effects on the Hydrolysis of N-Hydroxysuccinimide Ester Disulfides on Gold, *Langmuir* 19(14) (2003) 5780-5786.
- [31] C. Bonechi, A. Donati, R. Lampariello, S. Martini, M.P. Picchi, M. Ricci, C. Rossi, Solution structure of folic acid: Molecular mechanics and NMR investigation, *Spectrochimica Acta Part A: Molecular and Biomolecular Spectroscopy* 60(7) (2004) 1411-1419.
- [32] R. Singh Dhakad, R. Kumar Tekade, N. Kumar Jain, Cancer Targeting Potential of Folate Targeted Nanocarrier under Comparative Influence of Tretinoin and Dexamethasone, *Current Drug Delivery* 10(4) (2013) 477-491.
- [33] C.M. Alexander, K.L. Hamner, M.M. Maye, J.C. Dabrowiak, Multifunctional DNA-Gold Nanoparticles for Targeted Doxorubicin Delivery, *Bioconjugate Chemistry* 25(7) (2014) 1261-1271.

- [34] D. Xuan, X. Sheng-Hua, S. Zhi-Wei, A. Yan, Effect of the Hydrodynamic Radius of Colloid Microspheres on the Estimation of the Coagulation Rate Constant, *Acta Physico-Chimica Sinica* 26(10) (2010) 2807-2812.
- [35] X. Feng, X. Lou, The effect of surfactants-bound magnetite (Fe₃O₄) on the photocatalytic properties of the heterogeneous magnetic zinc oxides nanoparticles, *Separation and Purification Technology* 147(0) (2015) 266-275.
- [36] M. Ramani, S. Ponnusamy, C. Muthamizhchelvan, J. Cullen, S. Krishnamurthy, E. Marsili, Morphology-directed synthesis of ZnO nanostructures and their antibacterial activity, *Colloids and Surfaces B: Biointerfaces* 105(0) (2013) 24-30.
- [37] G. Xiong, U. Pal, J.G. Serrano, K.B. Ucer, R.T. Williams, Photoluminescence and FTIR study of ZnO nanoparticles: the impurity and defect perspective, *physica status solidi (c)* 3(10) (2006) 3577-3581.
- [38] P. Huang, L. Bao, C. Zhang, J. Lin, T. Luo, D. Yang, M. He, Z. Li, G. Gao, B. Gao, S. Fu, D. Cui, Folic acid-conjugated Silica-modified gold nanorods for X-ray/CT imaging-guided dual-mode radiation and photo-thermal therapy, *Biomaterials* 32(36) (2011) 9796-9809.
- [39] S.K. Sahu, S.K. Mallick, S. Santra, T.K. Maiti, S.K. Ghosh, P. Pramanik, In vitro evaluation of folic acid modified carboxymethyl chitosan nanoparticles loaded with doxorubicin for targeted delivery, *Journal of Materials Science : Materials in Medicine* 21(5) (2010) 1587-1597.
- [40] J. Peng, L. Zhao, X. Zhu, Y. Sun, W. Feng, Y. Gao, L. Wang, F. Li, Hollow silica nanoparticles loaded with hydrophobic phthalocyanine for near-infrared photodynamic and photothermal combination therapy, *Biomaterials* 34(32) (2013) 7905-7912.
- [41] Y. Barenholz, Doxil[®] — The first FDA-approved nano-drug: Lessons learned, *Journal of Controlled Release* 160(2) (2012) 117-134.
- [42] M.A. Amantea, A. Forrest, D.W. Northfelt, R. Mamelok, Population pharmacokinetics and pharmacodynamics of pegylated-liposomal doxorubicin in patients with AIDS-related Kaposi's sarcoma, *Clinical Pharmacology & Therapeutics* 61(3) (1997) 301-311.
- [43] F.M. Kievit, F.Y. Wang, C. Fang, H. Mok, K. Wang, J.R. Silber, R.G. Ellenbogen, M. Zhang, Doxorubicin loaded iron oxide nanoparticles overcome multidrug resistance in cancer in vitro, *Journal of Controlled Release* 152(1) (2011) 76-83.
- [44] S. Paukner, G. Kohl, W. Lubitz, Bacterial ghosts as novel advanced drug delivery systems: antiproliferative activity of loaded doxorubicin in human Caco-2 cells, *Journal of Controlled Release* 94(1) (2004) 63-74.
- [45] P. Anderle, E. Niederer, W. Rubas, C. Hilgendorf, H. Spahn-Langguth, H. Wunderli-Allenspach, H.P. Merkle, P. Langguth, P-glycoprotein (P-gp) mediated efflux in Caco-2 cell monolayers: The influence of culturing conditions and drug exposure on P-gp expression levels, *Journal of Pharmaceutical Sciences* 87(6) (1998) 757-762.
- [46] F. Bottero, A. Tomassetti, S. Canevari, S. Miotti, S. Ménard, M.I. Colnaghi, Gene Transfection and Expression of the Ovarian Carcinoma Marker Folate Binding Protein on NIH/3T3 Cells Increases Cell Growth in Vitro and in Vivo, *Cancer Research* 53(23) (1993) 5791-5796.
- [47] S.D. Weitman, R.H. Lark, L.R. Coney, D.W. Fort, V. Frasca, V.R. Zurawski, B.A. Kamen, Distribution of the Folate Receptor GP38 in Normal and Malignant Cell Lines and Tissues, *Cancer Research* 52(12) (1992) 3396-3401.

CHAPTER 3

3 Novel, folic acid conjugated, Fe₃O₄-ZnO hybrid nanoparticles for cancer targeted photodynamic therapy

3.1 Introduction

Since its first modern demonstration in 1975 [1], photodynamic therapy (PDT) has been the subject of extensive investigation, allowing it to emerge as an alternative oncologic intervention for many types of cancer [2, 3]. PDT involves the administration of a tumour-localising photosensitiser (PS) followed by local irradiation using light of a specified wavelength to activate the PS. The excited PS transfers its energy to molecular oxygen resulting in the formation of cytotoxic reactive oxygen species (ROS). These ROS are able to oxidise key cellular macromolecules, leading to apoptosis or necrosis and eventually tumour shrinkage [4]. Unlike conventional cancer treatments such as chemotherapy, which induces systemic toxicity [5], or radiation therapy, which damages neighbouring normal tissues [6], PDT employs two components, namely the PS and light, that should ideally contribute no toxicity to biological systems on their own.

Current research trends pertinent to PS are steering away from classical porphyrin-based PS drugs that normally contain large π -conjugation domains and are hydrophobic. Hydrophobicity leads to aggregation of these large-molecule-based PSs under physiological conditions, consequently resulting in poor ROS yield, which is essential for efficacious PDT [7]. Furthermore, poor selectivity to target tissues and low clearance levels of classical PSs have led to skin hyper-photosensitivity and associated pain in patients after treatment [8]. Ideally, a PS geared towards efficacious PDT should be able to combine a high yield of ROS, with excellent cancer cell selectivity when used at therapeutic concentrations, while minimising damage to normal tissue. The implementation of nanotechnology to the design of PSs has given rise to promising results in this regard. Recent reviews [9, 10] have highlighted the potential for nanoparticles (NPs) to mitigate the shortfalls of classical PSs. Encapsulation and or conjugation of PS molecules into NPs with biocompatible/hydrophilic surface functional groups has been shown to reduce toxicity and aggregation as well as increase the concentration of PSs to targeted tissue. Summarised also, is the discovery and development of certain nano-scale materials that are able to generate a high level of ROS due to unique optical absorption properties. These semiconducting materials are able to function as PSs without the need of conjugated or encapsulated small molecule PSs. Titanium dioxide (TiO_2) is such an example, and has been widely studied for killing different groups of microorganisms including bacteria, fungi and viruses, as well as cancer cells via PDT [11, 12]. Problems such as insufficient selectivity and low efficiency, as well as metal toxicity are yet to be overcome before TiO_2 can be considered clinically viable. Zinc oxide (ZnO), also an n-type semiconductor material, has been widely investigated for applications in photocatalysis and is well regarded due to its high photosensitivity, environmentally friendly nature and low cost [13, 14]. Under irradiation of UV light with energy greater than its band gap energy (3.2 eV), ZnO can be photoexcited to generate negative electrons (e_{CB}^-) in the conduction band and positive holes (h_{VB}^+) in the valence band. These photo induced electron-hole pairs have strong reduction and oxidation properties and can either recombine or be captured by other molecules such as oxygen or water, forming ROS such as the superoxide radical ($\text{O}_2^{\bullet-}$) and hydroxyl radical (OH^\bullet). These ROS react with surrounding biological molecules such as lipids, proteins and DNA, eventually leading to cell death.

Pure ZnO PSs have been used via PDT for the treatment of malignant cell lines in vitro, with some success [15]. Hackenberg and co-workers [16], used rod shaped (79 nm

longitudinal) ZnO NPs to show a significant ($P < 0.05$) reduction in the viability of two human head and neck squamous cell carcinoma cell lines. Upon 15 min of UVA radiation the viability of HLaC 78 cells was reduced to about 65% and 35% using ZnO NPs at a concentration of 0.2 and 2.0 $\mu\text{g}\cdot\text{mL}^{-1}$ respectively. Similar results were obtained using a UD-SCC 7A cell line. Zhang et al [17] also used rod shaped ZnO PSs; their PS elicited a 45% drop in the viability of SMMC-7721 cells upon exposure to UV radiation for 3 min with a 6 h PS incubation period. Metal doped ZnO PSs have been used analogously, also with promising results [18, 19]. Iron and silver doped ZnO NPs were shown to reduce the viability of human liver adenocarcinoma cells (HepG2) to 50% of a control using respective concentrations of 42.6 and 37.2 $\mu\text{g}\cdot\text{mL}^{-1}$ of the photocatalysts with 3 minutes of exposure to UV irradiation [18]. Rapid recombination of photo-induced electron-hole pairs however, has compromised the photocatalytic effectiveness of ZnO [20, 21] and furthermore, biological toxicity associated with ZnO nanoparticles (NPs) poses another problem [22]. As such, the development of novel, biocompatible, composite ZnO NPs that can effectively suppress charge recombination has gained momentum of late for effective PDT [23, 24].

A recent development by our team has shown a dramatic increase in the phenol degradation efficiency by a Fe_3O_4 -ZnO nanocomposite (82%) when compared to pure ZnO NPs (52%) [20]. The study demonstrated a retardation of charge recombination in ZnO through the presence of Fe^{3+} as electron trapping sites, therefore improving the photophysical properties of the Fe_3O_4 -ZnO hybrid NPs and attracting wide attention of researchers in the field of photocatalysis [25-28]. We also have observed dissolution of ZnO induced by both chemical and photodissolution [20, 21]. The dissolution of the hybrid NPs, which reduces the photocatalytic effectiveness, may become a bonus characteristic in managing clearance from the body and reducing possible side effects, should the NPs prove to be effective in PDT. The aim of the current study was to synthesise and characterise FA conjugated hybrid Fe_3O_4 -ZnO NPs (FZ-SFA), and to further assess their photosensitivity and interactions with cancerous cells under radiation. To achieve this, silanisation and chemical conjugation of FA to the hybrid Fe_3O_4 -ZnO cores was carried out. The photocatalytic properties of the novel PS were assessed and optimised through the photo-degradation of methylene blue (MB). Subsequently, the assessment of cell viability and effective photo-induced cytotoxicity of NPs was carried out through use of colorectal adenocarcinoma (Caco-2) cancer cells. The dissolution of metal components was also examined to provide

insight into the mechanistic workings of the PS, while also provisioning the need for future control of metal toxicity.

3.2 Materials and Methods

3.2.1 Materials

The following chemicals were purchased from Sigma-Aldrich Australia: Zinc acetate dihydrate ($\geq 98\%$, $\text{Zn}(\text{Ac})_2 \cdot 2\text{H}_2\text{O}$), tetraethyl orthosilicate (99.999%, TEOS), (3-aminopropyl) triethoxysilane (99%, APTES), N-hydroxysuccinimide (NHS), N,N'-dicyclohexyl carbodiimide (DCC), reagent grade triethylamine, folic acid (97%, FA). Methylene blue (MB), anhydrous ether, dimethyl sulfoxide (DMSO) and diethylene glycol (99%, DEG) were sourced from Alfa Aesar.

3.2.2 Chemical Synthesis

The synthesis of hybrid iron/zinc oxide (FZ) nanoparticles was carried out by first preparing iron oxide (magnetite, Fe_3O_4) NPs via a chemical co-precipitation method. The Fe_3O_4 NPs were then used as seeds for the growth of hybrid FZ nanoparticles via dehydration of a zinc acetate dihydrate precursor in DEG. Control ZnO NPs were prepared in a similar fashion. Readers are referred to our previous work for detailed synthesis of these initial steps [20]. Subsequent synthetic stages are illustrated schematically in Figure 3-1 and are outlined below.

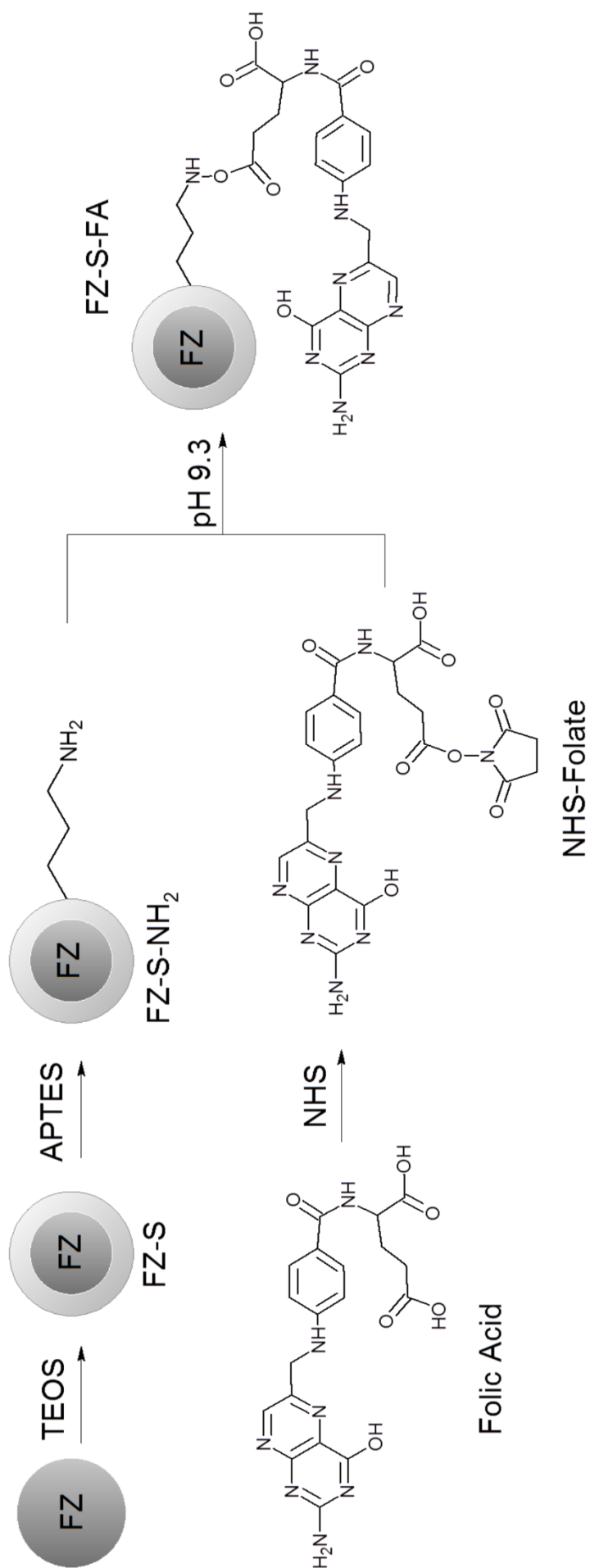


Figure 3-1. Synthetic scheme outlining preparation of FZ-S and FS-SFA NPs.

Silanisation of the FZ hybrid NPs to produce silica coated FZ-S NPs was achieved through a sol-gel process, employing TEOS. Readers are referred to our previous work for detailed silanisation procedures [11]. FA conjugation was achieved by first functionalising the FZ-S NP surfaces with active amine groups. This required the drop-wise addition of APTES (1:1, 2:1 and 4:1 molar ratio of TEOS:APTES) in 20 mL ethanol to a FZ-S NP suspension, followed by 2 hours mechanical stirring at room temperature. Control of the TEOS:APTES ratio was vital to ensure management of folate content in subsequent synthetic steps. The aminated FZ-S NPs (FZ-SNH₂) were collected via external magnet and were washed three times sequentially in ethanol followed by milli-Q water using ultra sonication.

At the same time, the NHS ester of FA (NHS-FA) was synthesised via a DCC coupling method reported previously [29]. NHS-FA intermediate facilitated conjugation of FA to FZ-SNH₂. Briefly, 0.1 g of FZ-SNH₂ NPs were dispersed in 10 mL of Na₂CO₃/NaHCO₃ buffer (pH 9.30) using sonication for 10 min. NHS-FA (1:1 molar ratio of APTES:NHS-FA) was added drop wise to the NP suspension with constant mechanical stirring for one hour. FZ-SFA NPs were collected via external magnet and were washed in conjunction with sonication 5 times in DMSO followed by 3 times with milli-Q water. The prepared FA conjugated NPs were termed FZ-SFA100, FZ-SFA50 and FZ-SFA25 in order of decreasing FA content.

3.2.3 Nanoparticle characterisation

Transmission electron micrographs of the produced NPs were obtained using our previously reported method [12]. Geometric particle size analysis was carried out using Gwyddion imaging software. Hydrodynamic particle size and size distribution were further assessed via dynamic light scattering (DLS) using a Zetasizer Nano-ZS from Malvern Instruments. Zeta potential was carried out using the same instrument. Sodium chloride (10 ml, 0.01 M) was used as a conductive regulator. The pH of the sodium chloride solution was adjusted to 4.0, 6.0, 7.4 and 9.3 using an aqueous solution of NaOH (0.01 M) and HCl (0.01 M). Samples (1 mg) were dispersed in the resulting solutions (10 mL) using ultra sonication (10 min) prior to measurement.

X-ray diffraction (XRD) analysis was conducted on ZnO, Fe₃O₄ and FZ samples using a D8 Discover (Bruker AXS, Germany) x-ray diffractometer with cobalt K α radiation ($\lambda = 1.78901 \text{ \AA}$). A scan rate of 0.015°/s was used to obtain patterns within a 2 θ range of 10-

80° using an accelerating voltage of 35 kV and a current of 40 mA. Phase identification software (Match! Version 3.1.0 50) was used to index the spectral peaks with planes.

A Thermo Scientific Nicolet is50 FT-IR spectrometer equipped with an automated beam splitter exchanger, affording both mid-IR and far-IR capabilities, was used to identify various chemical functional groups. Quantification of FA bound to the NP surfaces was carried out using thermogravimetric analysis (TGA; Mettler Toledo) as reported previously [30].

Elemental iron and zinc content within the NPs was quantified via ICP-OES (Perkin Elmer Optima 8300 ICP-OES spectrometer). Analysis was performed at wavelengths of 238.2 and 206.2 nm respectively for iron and zinc. Samples were prepared through dissolution of approximately 1 mg of NPs in 25 mL of 2 M nitric acid at 80 °C for 60 min under reflux. Upon cooling, samples were diluted with milli-q water to a concentration within the range of prepared standards (5-100 mg.L⁻¹).

Optical properties of the NPs were characterised via UV-Vis diffuse reflectance spectroscopy using a Jasco V670 spectrophotometer equipped with an integrating sphere, with BaSO₄ as a reference material. All samples were subject to a scan range from 250 nm to 750 nm with a band width of 2 nm. Fluorescence spectroscopy was also carried out, using an Aligent Technologies Cary Eclipse fluorescence spectrophotometer with excitation wavelengths of 277 nm for all synthesised NPs and 283 nm for FA conjugated NPs. Spectra were obtained using a scan rate of 600 nm.min⁻¹ with 10 co-added scans.

3.2.4 Adsorption and photoreactivity study

Adsorption and photocatalytic properties of ZnO, Fe₃O₄, FZ, FZ-S, and FZ-SFA NPs were evaluated through measurement of the MB concentration of solutions containing PSs without and with exposure to UV radiation, respectively, over time. Reaction solutions had a MB concentration of 10 mg.L⁻¹ (pH 4.0, 6.0, 7.4 or 9.3) and a photocatalyst concentration of 325 mg.L⁻¹. This reaction mixture was placed in a 1 L double-jacket reactor with cycled cooling water (25 ± 1 °C) where a directed stream of nitrogen gas was used to agitate the reaction mixture. Adsorption of MB on the photocatalysts was investigated in the dark; 2-3 mL aliquots of the reaction mixture were sampled via syringe at set intervals over a 90 min period. Adsorption percentage was determined via ratio of MB concentration at time *t* termed *C_t*, divided by the initial MB concentration (*C₀*). For photodegradation of MB, UV irradiation was facilitated by a MSR 575/2 metal halide lamp (575W, Philips) with a

wavelength range of 315-1050 nm. The experimental setup remained the same, however at the 90 min mark the light source was immediately turned on. Photocatalysts were separated from the reaction solution before UV-Vis analysis by first collecting via external magnet prior to passing the solution through a 0.2 μm Millipore film. Degradation percentage was determined analogously to adsorption percentage; however C_t was divided by the MB concentration at $t = 90$ min (C_0').

3.2.5 Cell culture and MTT cell viability assay

Culture of Caco-2 cells was carried out using a previously reported procedure [30]. Caco-2 cell viability was assessed by 3-(4,5-dimethylthiazol-2-yl)-5-(3-cayboxymethoxyphenyl)-2-(4-sulfophenyl)-2H-tetrazolium (MTT) assay as described by Mossman [31], with some modifications. Briefly, 5×10^3 cells per well were seeded in 96-well plates and cultured for 48 hours before exposure to FZ, FS-S, FZ-SFA50 and FZ-SFA25 NPs at concentrations of 12.5, 25, 50 and 100 $\mu\text{g}\cdot\text{mL}^{-1}$ for 6 hours and 24 hours. After exposure, MTT solution 100 μL (1 $\text{mg}\cdot\text{mL}^{-1}$) was added to each well and incubated for 4 hours at 37°C. The resulting formazan product was dissolved in DMSO (100 μL per well). The absorbance was quantified at 570 nm using a microplate reader (Perkin Elmer). Results were reported as percentage viability with respect to untreated cells according to the following equation:

$$\text{Cell Viability (\%)} = \frac{A_{test} - A_{NP}}{A_{control} - A_{blank}} \quad \text{Equation 3-1}$$

Where A_{test} was the absorbance of the formazan produced by cells incubated with NPs in medium, A_{NP} was the absorbance associated with just NPs in medium, $A_{control}$ was the absorbance of just cells in medium and A_{blank} corresponded to the absorbance of the DMEM medium alone.

3.2.6 Photokilling effect

5×10^3 cells per well were seeded and allowed to grow for 48 h. The cell supernatant was replaced with fresh medium containing FZ, FZ-S FZ-SFA25 and FZ-SFA50 NPs at concentrations of 12.5, 25 and 50 $\mu\text{g}\cdot\text{mL}^{-1}$ incubated for 24 h. Following exposure of the cells with NPs, the plates were treated with UV-A radiation (365 nm) at a dose of 10 $\text{J}\cdot\text{cm}^{-2}$ in a BS-02 UV chamber (8 x 15 W lamps at 120 W total power output, UV-GROEBEL,

Germany) for 10 min at a distance of 10 cm from the lamps. Chamber temperature (37-38°C) was monitored using an IR thermometer (ThermoFisher, Australia) and was maintained via circulating fan within the chamber. After UV exposure the cells were allowed to grow for 24 h, and cell viability was assessed via MTT assay. Viability of cells not exposed to UV radiation was expressed as a percentage according to Eq. 1. The cell viability corresponding to UV exposed samples was expressed in the same way however, A_{test} corresponded to cells incubated with NPs in medium that had also been exposed to UV radiation and $A_{control}$ corresponded to UV exposed cells in the absence of NPs.

3.2.7 Statistical analysis

All experiments were repeated at least two times under identical conditions. The results were expressed as mean \pm standard deviation ($n = 4$). All data were analysed using two-way-ANOVA, via Bonferroni's multiple comparisons test (GraphPad Prism 6). Statistical significance was considered at $P < 0.05$.

3.3 Results and Discussion

3.3.1 Nanoparticle synthesis and characterisation

The hybrid Fe_3O_4 -ZnO oxide (FZ) NPs were prepared according to previously reported work [20]. Surface modification of FZ NPs was carried out with silica and the subsequent esterification of FA with NHS (Figure 3-1). The produced novel, folate bound, silica coated PSs (FZ-SFA) showed an average diameter of 21.4 ± 3.5 nm via TEM, which is greater than that of the unmodified FZ PSs (16.1 ± 2.5 nm). TEM micrographs of FZ and FZ-SFA are presented in Figure 3-2. The silica shell present in FZ-SFA NPs is clearly visible and is indicated by the arrows in Figure 3-2b. The estimated shell thickness was approximately 2.7 nm, coinciding well with our previous work [11].

XRD spectra for Fe_3O_4 , ZnO and FZ NPs are presented in Figure 3-3. Peak identification software allowed assignment of the $2\theta = 21.37^\circ$, 35.26° , 41.59° , 50.76° , 63.35° , 37.64° and 74.58° diffraction signals to the (111), (202), (311), (400), (422), (333) and (404) planes of magnetite respectively, with a cubic crystal structure according to [32]. Hybridisation to form FZ NPs resulted in the appearance of 4 new signals, identified at the $2\theta = 37.05^\circ$, 40.22° , 42.30° and 55.81° positions. These signals were also present in the diffraction pattern of pure ZnO and correspond to the (100), (002), (101) and (012) planes of hexagonal

wurtzite-structured ZnO (zincite) [33]. The relatively weak signals at 21.37° and 50.76° match those of the (111) and (400) planes in Fe_3O_4 indicating the presence of the iron oxide within the hybrid NPs. The relatively low signal strength of the Fe_3O_4 phase can be explained by the mass ratio of Iron oxide to zinc oxide in the hybrid NPs. The ratio was determined via quantification of metal content via ICP-OES and was determined to be 1:5.2 in favour of ZnO.

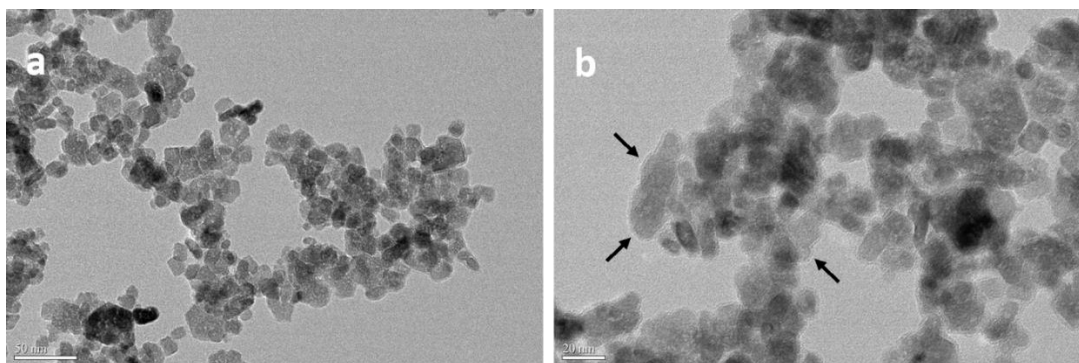


Figure 3-2. TEM micrographs of (a) FZ and (b) FZ-SFA NPs. Black arrows in (b) indicate the silica layer.

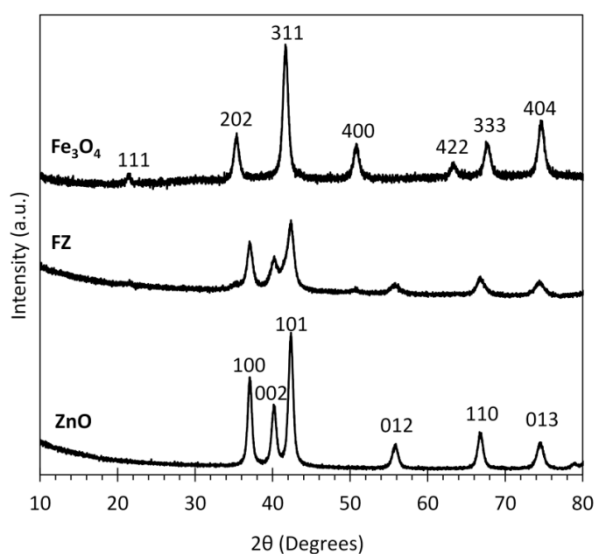


Figure 3-3. XRD diffraction patterns for Fe_3O_4 (a), FZ (b) and Zn (c) NPs.

FTIR spectra of all nanoparticles are displayed in Fig. 4a (left). Both of the Fe–O and Zn–O stretching vibrations were evident in the spectra of hybrid FZ NPs and corresponded well with literature [34, 35]. Silanisation was confirmed by appearance of a strong absorption band between 1000 cm^{-1} and 1200 cm^{-1} (FZ-SNH₂ spectrum), attributable to the asymmetric bending and stretching vibrational modes of siloxane groups [36]. Amination

was confirmed by appearance of bands between 1603 cm^{-1} and 1625 cm^{-1} , indicative of N–H bending and NH_3^+ deformation vibrational modes [12]. The shoulder at 1624 cm^{-1} was ascribed to the vibrational mode of the carbonyl group in the unbound carboxylic acid moiety of FA. The amide bond that was formed upon FA conjugation gave rise to bands at 1622 cm^{-1} due to vibrational modes of the amide band I C=O group, as well as 1576 cm^{-1} and 1538 cm^{-1} , assigned respectively to the C–N and N–H bending modes of the amide band II. The signal at 3321 cm^{-1} was assigned to N–H stretching vibration, and further confirmed FA conjugation [12, 37]. Signals between 2830 cm^{-1} and 2950 cm^{-1} grew in intensity and were assigned to C–H symmetric and asymmetric stretching vibrations.

Solid-state UV-visible DRS absorbance spectra are detailed in Figure 3-4a. An absorbance threshold of 400 nm was observed for pure ZnO, corresponding to a band gap energy of 3.1 eV, well corroborated by literature and assigned to electron transitions from the valence band to the conduction band ($\text{O}2\text{p} \rightarrow \text{Zn}3\text{d}$) [38]. The broad absorbance region between 350–650 nm in the case of the Fe_3O_4 was attributed to octahedral Fe^{3+} [20, 39]. All hybrid NPs contained absorbance regions corresponding to both ZnO and Fe_3O_4 . The presence of the silica layer enhanced the absorbance intensity within the region of the characteristic ZnO band. The absorption threshold of FZ composite NPs was estimated to be 430 nm by taking the departure point from zero of the second derivative of absorption spectra provisioning an estimated band gap energy of 2.9 eV. The shift towards lower band gap energy for the hybrid NPs suggests that light within the visible region of the electromagnetic spectrum may have sufficient energy for electron excitation and subsequently ROS generation.

Figure 3-4b (left) exemplifies the TGA curves for mass loss percentage as a function of temperature using FZ-SFA25, FZ-SNH₂, and FZ-S. From the TGA curves, a FA content of 0.059, 0.085 and 0.187 $\text{mmol}\cdot\text{g}^{-1}$ was obtained respectively for FZ-SFA25, FZ-SFA50 and FZ-SFA100 [30].

The fluorescence emission intensity of FZ-SFA samples at 451 nm using an excitation wavelength of 283 nm (Figure 3-4b (right)) was compared to that of standard FA solutions ranging from 0.006 to 0.06 $\text{mg}\cdot\text{L}^{-1}$. FA content was found to be 0.063, 0.090 and 0.145 $\text{mmol}\cdot\text{g}^{-1}$ for FZ-SFA25, FZ-SFA50 and FZ-SFA100 NPs respectively. These values agree well with those obtained via TGA. FA, commonly used in the growth medium for cell culture work had a concentration of 4 $\mu\text{g}\cdot\text{mL}^{-1}$ within the DMEM medium according to the product specification sheet. Previously we showed that FA content on our NPs serves to

supplement the growth of cancer cells [12, 30]. This prompted the need for control of FA content on the NP surfaces. The NP concentration range used for cell work in this study was 12.5 – 100 $\mu\text{g}\cdot\text{mL}^{-1}$ and corresponded to a FA content of 0.33 – 2.60 $\mu\text{g}\cdot\text{mL}^{-1}$ and 0.47 – 3.75 $\mu\text{g}\cdot\text{mL}^{-1}$ for FZ-SFA25 and FZ-SFA50 respectively. Using the average particle size of FZ-SFA, the density of FA on NP surfaces was estimated to be 0.39, 0.60 and 1.25 molecules per nm^2 for FZ-SFA25, FZ-SFA50 and FZ-SFA100. The estimation for FZ-SFA100 was expected to be and is consistent with the FA density of ZSFA(215) NPs from chapter 2 (1.16 molecules per nm^2) as similar FA precursor amounts were used in the synthesis of these particles. The estimation also shows that reducing the amount of FA precursor in the synthetic stage has in fact reduced the density of the targeting ligand on the surfaces of FZ-SFA25 and FZ-SFA50 NPs.

NP optical properties were also probed using fluorescence spectroscopy. Fluorescence emission due to ZnO was found to be centred at 351 nm for all particles and the emission intensity was lower for the hybrid FZ NPs as compared to pure ZnO as shown in Figure 3-4b (centre). This was attributed to the presence of additional electronic energy states afforded by hybridisation with Fe_3O_4 . Silanisation of the hybrid particles saw a further reduction in the fluorescence intensity. This was ascribed to shielding of incident radiation by the silica layer and was demonstrated clearly in our previous work with TiO_2 [11]. The poly-cyclic aromatic ring structure of the FA molecule is known to facilitate fluorescent properties with a low quantum yield (< 0.005) [40]. The fluorescence associated with FA was believed to combine synergistically with that of the ZnO resulting in the observed increase in emission intensity of FA conjugated NPs. Figure 3-4b (right) portrays the emission spectra of free FA and FA conjugated NPs when subject to an excitation wavelength of 283 nm. Fluorescent intensity increased with increasing FA content and emission maxima were centred well at a wavelength of 451 nm. The signal centred at 352 nm in Figure 3-4b (right) was not present in the spectrum of free FA and was ascribed to emission due to ZnO present in the nanoparticulate samples.

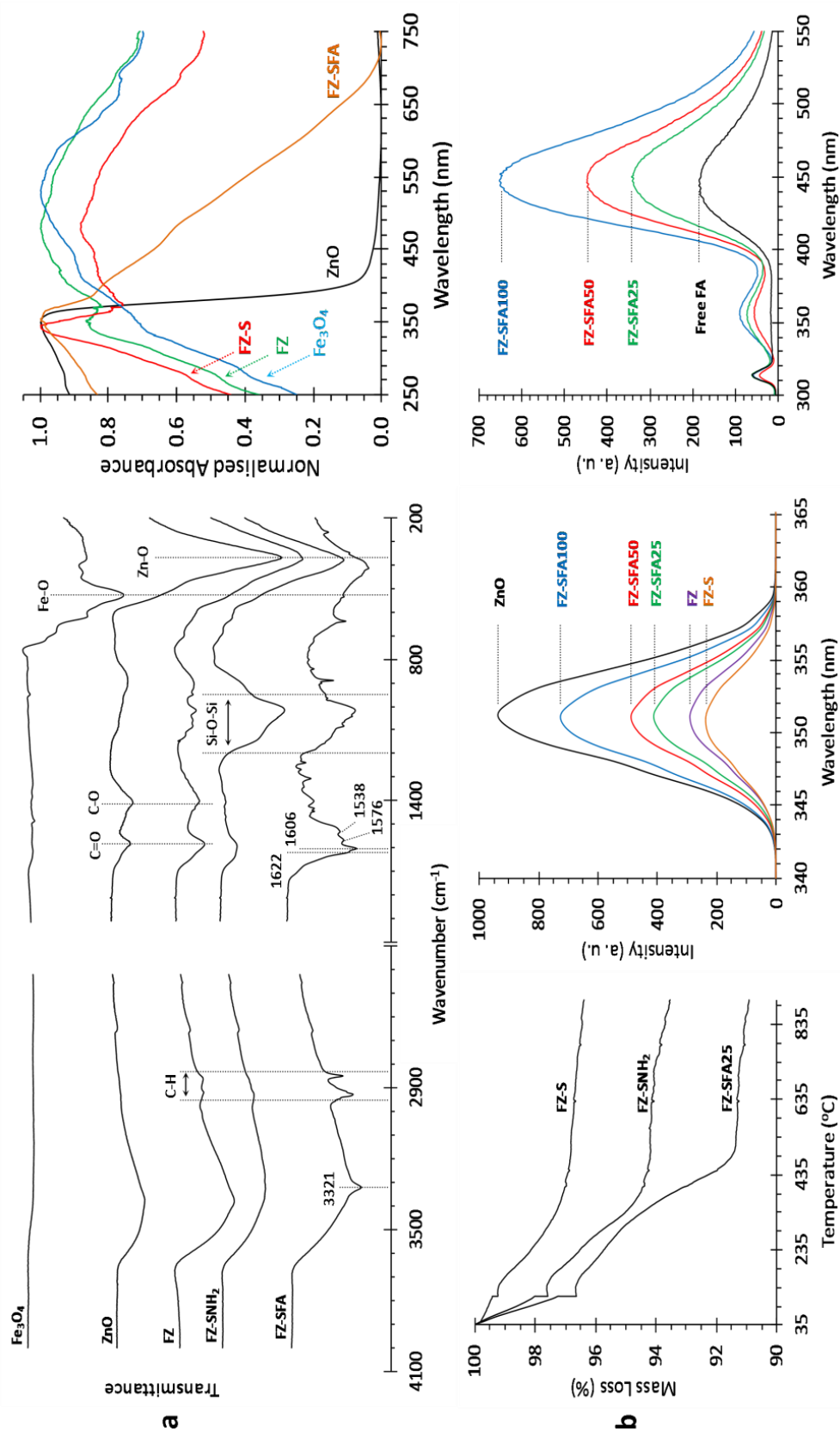


Figure 3-4. FTIR spectra (a, left), UV-Vis DRS spectra (a, right), TGA curves (b, left), fluorescence emission spectra using an excitation wavelength of 277 nm (b, centre) and 283 nm (b, right).

3.3.2 Adsorption and photocatalytic properties of FZ, FZ-S and FZ-S-FA NPs

The adsorption of MB over time is presented in Figure 3-5 (left) where C_t/C_0 represents the ratio of MB concentration at time t , over that at $t = 0$. At $t = 0$, the percentage of MB adsorption was determined to be 0.0, 33.8, 26.3, 30.8 and 24.0% for FZ, FZ-S, FZ-SFA25, FZ-SFA50 and FZ-SFA100 respectively. The measured zeta potential of the PSs indicated a double layer charge of -0.91, -16.5, -17.2, -20.6 and -23.4 mV respectively. As MB is known to be positively charged in solution [41], ultra-sonication during the dispersion process may have facilitated electrostatic adsorption of the dye onto the negatively charged particle surfaces. Lack of adsorption on FZ NPs was correlated to their less negative surface charge. The lower magnitude of charge on FZ NPs was ascribed to the presence of $N(CH_3)_4^+$ ions from a trimethyl ammonium hydroxide dispersing agent, used in their synthesis. A dramatic decrease in charge was seen for silanised particles due to the accumulation of surface hydroxyl groups. Folate conjugation correlated to a further increase in the magnitude of the negative charge. The presence of the unbound carboxylate group on FA (Figure 3-1) would lead to dissociation of a hydrogen ion in solution, leaving a negative charge on the surface of the particles. Charge induced adsorption of MB to negatively charged silica NPs seems a viable conclusion, and has been reported elsewhere [42]. Whilst the increase of FA content from FZ-SFA50 to FZ-SFA100 caused a reduction in the zeta potential, MB adsorption was found to decrease slightly, this was theorised to be a result of steric hindrance. Reduction in MB concentration via complexation with Zn^{2+} , Fe^{2+} , and Fe^{3+} ions was ruled out through repetition of adsorption experiments, where PSs were replaced by either Zn^{2+} and or Fe^{2+}/Fe^{3+} ions; no decline in MB concentration was found in these instances. Similar results were obtained through use of MB solutions at concentrations of 5 and 20 $mg.L^{-1}$.

After the initial 90 min adsorption period in the dark, MB concentration was found to stabilise and photodegradation was initiated by switching on the lamp. The percentage degradation of MB over time is displayed in Figure 3-5 (centre). A marked improvement in photodegradation was observed when using hybrid PSs over control ZnO NPs. The Langmuir-Hinshelwood equation (Eq. 3-2) [43], was used to estimate the apparent rate constant (κ , min^{-1}) for each NP catalyst, with fitting applied to the first 90 min of degradation data. C_t was defined as the MB concentration at time t , and C_0' was defined as

the concentration of MB at time $t = 90$ min. The fitting, apparent rate constants and least squares regression coefficients are presented in Figure 3-5 (right).

$$\ln(C_t/C_o') = \kappa t \quad \text{Equation 3-2}$$

While all hybrid NPs outperformed the control ZnO NPs, the photocatalytic efficiency of FZ-SFA PSs was found to decrease with increasing FA content. This is in agreement with our previous work investigating the shielding effect of silica using TiO₂ and phenol [11, 12]. The rate constant of FZ was over 5 fold greater than that of pure ZnO. This, combined with the reduction in fluorescence emission intensity of FZ NPs when compared to ZnO NPs (Figure 3-4b (centre)), showed conformity to our work with hybrid Fe₃O₄-ZnO and phenol [20].

Redox cycling resulting from electron entrapment by Fe³⁺ ions and subsequent reactions with oxygen within the reaction solution impedes recombination of photo-induced charge carriers within ZnO. The presence of dissolved iron at concentrations between 0.3 - 0.4 mg.L⁻¹ (Table 1) within the photocatalysis reaction mixtures at the end of the degradation studies was measured by ICP-OES, further confirming our hypothesis [20, 21]. A recent study [44] has also demonstrated that the synthesis of a p-n junction through the coupling of iron (III) oxide and ZnO allowed continuous diffusion of photoexcited electrons from the ZnO to the iron oxide (and vice versa for photo-induced holes) resulting in suppression of electron-hole pair recombination.

Table 3-1. ICP-OES quantification of Zinc and Iron in initial and final reaction solutions for adsorption and photodegradation studies at pH 7.4.

Analyte	Time (min)	FZ	FZS	FZ-SFA100	FZ-SFA50	FZ-SFA25
Zn (mg.L ⁻¹)	0	5.322	4.701	4.300	4.298	4.610
	90*	5.561	4.873	4.494	4.512	4.818
	240	7.230	6.840	6.741	6.692	6.910
Fe (mg.L ⁻¹)	0	0.000	0.001	0.000	0.002	0.000
	90*	0.001	0.002	0.000	0.002	0.001
	240	0.390	0.340	0.330	0.320	0.340

* $t = 90$ min corresponded to the end of the adsorption study. The UV lamp was switched on at this point, where photodegradation began.

3.3.3 Effect of pH on adsorption and photodegradation

Adsorption and degradation experiments were repeated under identical conditions at pH 4.0, 6.0, and 9.3 (Figure 3-6). MB adsorption percentage was found to increase with increasing pH, this trend was observed in all samples excluding the FZ NPs (Figure 3-6 (left)), which showed little to no adsorption. Adsorption trends correlated well with the increase in magnitude of the negative surface charge on the particles measured via Zeta potential (Figure 3-6). Despite having a greater electronegative surface charge, FA modified samples saw a decrease in adsorbed MB comparative to FS-S NPs, which as before, was ascribed to steric hindrance. A lower degree of adsorption at pH 4.0 and 6.0 was observed and ascribed to chemical corrosion of the PSs.

The pH dependence of MB photodegradation is highlighted in Figure 3-6b. Degradation increased with increasing pH. Lower photodegradation at lower pH values was due to the chemical dissolution of ZnO. The amount of dissolved zinc measured using ICP-OES in the reaction solutions over the studied pH range is shown in Table 1. The lower dissolved metal content at pH 9.3 demonstrated a much higher chemical stability of the PSs, leading to greater photodegradation of MB. Improved photodegradation could also be due to elevated particle surface charge at higher pH, as observed from DLS data (Figure 3-6b), which enhances inter-particle repulsion therefore increasing available surface area of the PSs.

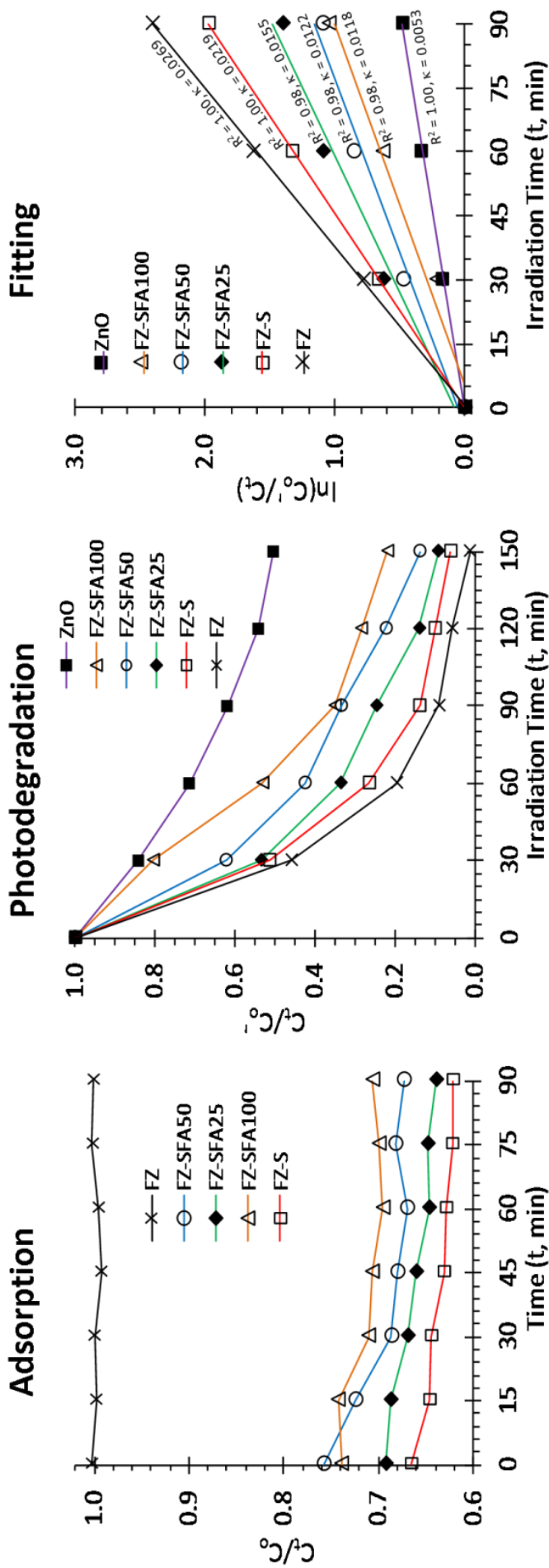


Figure 3-5. Change in MB concentration over time for adsorption (left) and photodegradation (centre) studies at pH 7.4. The linear fit as per Eq. 3-2 of the first 90 min of degradation data is shown on the right.

Dissolution of zinc and iron was not limited to pH based chemical corrosion, but was also observed to result from photocorrosion. This observation is best highlighted through ICP-OES analysis of iron content at pH 7.4 in Table 1. The iron content was clearly low and stable between the 90 min initial and post adsorption study periods in the absence of UV radiation. The measured iron content was higher after the photodegradation study with UV irradiation.. The increase in iron dissolution was attributed to photo-corrosion of the hybrid NPs, whereby interactions between photo-induced holes and the metal oxides yielded water soluble Zn^{2+} and Fe^{2+}/Fe^{3+} ions [20]. The presence of Fe^{2+}/Fe^{3+} ions therefore, is not limited to chemical corrosion and corroborates the hypothesis in our previous work [20] regarding electron-trapping as a mechanism for slower electron-hole recombination. The mildly acidic extracellular pH of tumour microenvironments may contribute to the chemical corrosion of the fabricated PSs. Whilst the presence of Fe^{3+} has been shown to enhance photo catalysis, corrosion of the ZnO phase could result in diminutive photocatalytic efficiency as well as possible metal induced toxicity. Optimisation of the dissolution kinetics under biological conditions is the subject of current investigations.

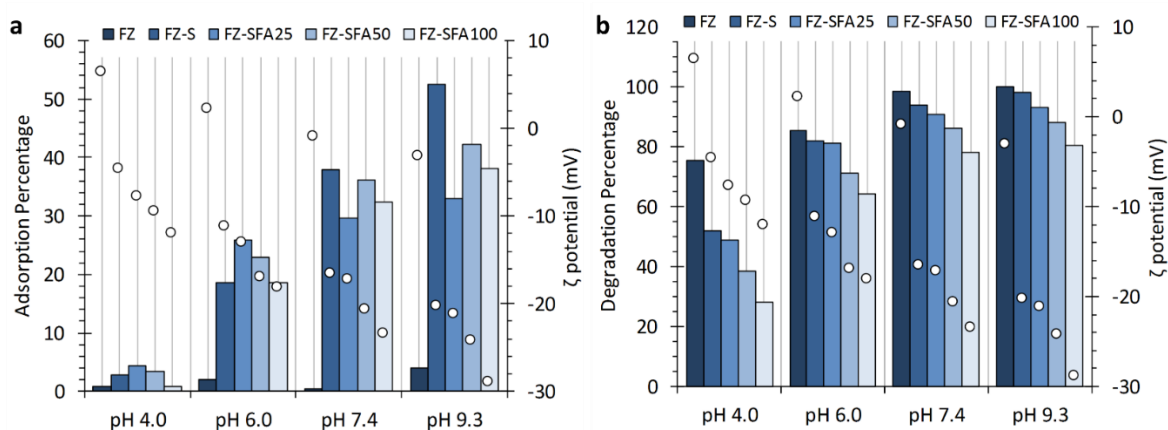


Figure 3-6. Effect of pH on adsorption (a) and photodegradation (b) of MB. Open circles designate the zeta potential of the corresponding samples, at the given pH.

3.3.4 Cell toxicity and photokilling effect

Caco-2 cell viability was assessed after incubation in the presence of FZ, FZ-S, FZ-SFA25 and FZ-SFA50 NPs for 6 h at various concentrations as per Figure 3-7. A time and concentration dependence was seen across all samples. After a 6 h exposure to the NPs, Caco-2 cell viability was above 80% at a NP concentrations $< 100 \mu\text{g}\cdot\text{mL}^{-1}$ for all samples (Figure 3-7 (left)). Increasing the exposure time to 24 h (Figure 3-7 (centre)) saw a

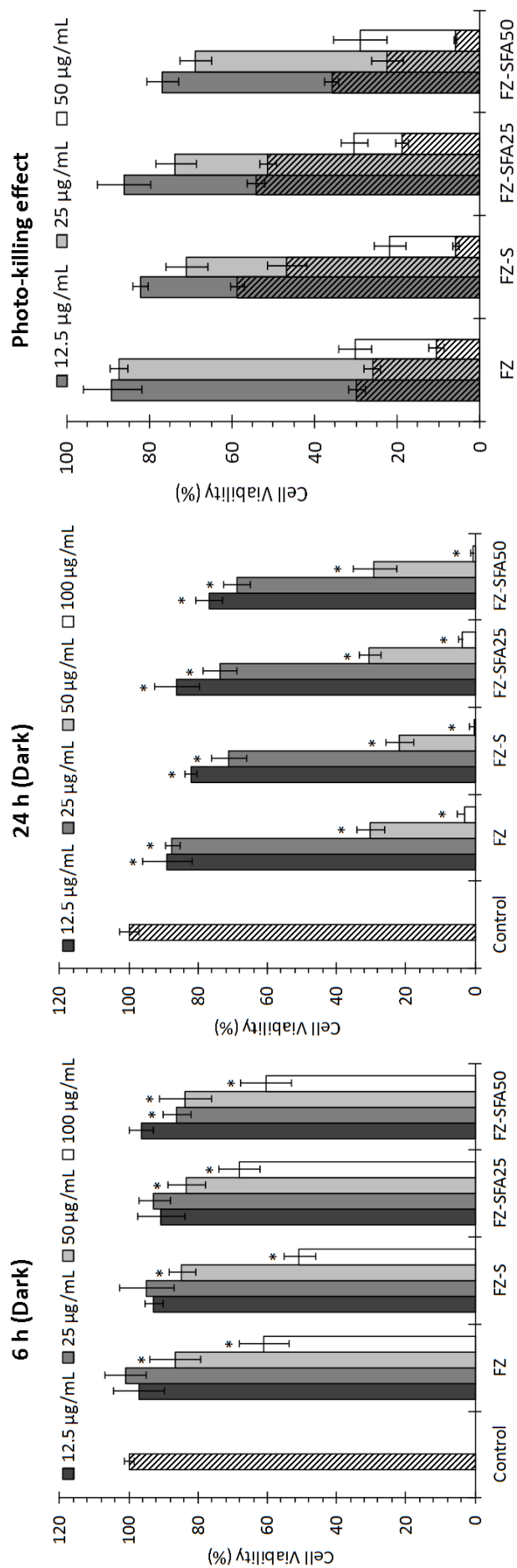


Figure 3-7. Viability of Caco-2 cells upon exposure to various NPs for 6 h (left) and 24 h (center) and 24 h (right) at various concentrations. Photo-induced reduction in Caco-2 cell viability is shown on the right, where shaded portions of the columns represent the level to which cell viability was reduced after exposure to UV radiation.

statistically significant reduction in cell viability for all NPs, at all concentrations ($P < 0.05$). The cell viability was above 70% at NP concentrations $\leq 25 \mu\text{g.mL}^{-1}$, however dropped to below 35% when the NP concentrations were $\geq 50 \mu\text{g.mL}^{-1}$ (Figure 3-7 (centre)). This indicated possible toxicity caused by dissolved zinc ions (7.5 mg.L^{-1} across all NPs as shown in Table 1). A study by Zödl et al reported significant reduction in Caco-2 cell proliferation upon exposure to zinc at concentrations $> 150 \mu\text{M}$ (9.8 mg.L^{-1}) [45]. At 6 h, the presence of the silica coating was found to reduce the cell viability from 64% (FZ) to 52% (FZ-S) (Figure 3-7 (left)) at $100 \mu\text{g.mL}^{-1}$. This trend was even more obvious upon prolonged exposure to 24h with FZ-S showing a statistically significant reduction in cell viability when compared to FZ (Figure 3-7 (centre)) at all concentrations. Whilst in many cases silica has been used to promote cell compatibility [11], some studies have reported in vitro toxicity associated with silica NPs, stemming from ROS generation [46], impaired cell membrane integrity [47], metabolic activity of cell line [48], as well as simply adjusting the dose, size of NPs, time of exposure to cells and type of cell line. Our recent work with hollow silica NPs [30] has also shown toxic effect towards Caco-2. We have speculated that Caco-2 may have an aversion to silica NPs. The results in Figure 3-7 (left) also showed that the cell viability for FA bound NPs at $100 \mu\text{g.mL}^{-1}$ were greater than that of FZ and FZ-S NPs, suggesting supplementation of cell growth, also reported in other studies [12, 30, 49]. The estimated folate content of FZ-SFA25 and FZ-SFA50 at a NP concentration of $100 \mu\text{g.mL}^{-1}$ equated to 2.60 and $3.75 \mu\text{g.mL}^{-1}$ of FA respectively, corresponding to a 65% and 94% increase in the total FA content in the DMEM medium.

FZ, FZ-S, FZ-SFA25 and FZ-SFA50 were chosen to assess the effect of UV exposed PSs to the viability of Caco-2 cells after an incubation period of 24 h. Figure 3-7 highlights the photo-induced reduction in cell viability in which the influence of radiation alone on the cells was subtracted and changes in viability upon exposure were due fundamentally to cellular interactions with light irradiated PSs. In all cases, Caco-2 cells suffered a substantial photo-induced reduction in viability. At a nano-PS concentration of $50 \mu\text{g.mL}^{-1}$ the cell viability was reduced to 6 to 11% upon UV irradiation, compared to 22 to 31% in the absence of radiation. For UV irradiated FZ at $12.5 \mu\text{g.mL}^{-1}$ the cell viability was reduced to 30%, compared to 89% in the dark. The silica coating hampered photo-killing due to the shielding effect when compared to FZ NPs, leading to a cell viability of 59%. Conjugation of FA improved the photo-killing effect with the viability being reduced to 54% and 36%

respectively upon UV irradiation of FZ-SFA25 and FZ-SFA50 respectively. This was likely due to the increased particle-cell interactions in the presence of FA. A similar effect was seen in our previous work with folate bound TiO_2 [12].

3.4 Conclusion

A novel folic acid conjugated hybrid Fe_3O_4 -ZnO (FZ-SFA) NP was fabricated and assessed for its potential as a photosensitiser (PS) in therapeutic applications pertinent to PDT. Photodegradation studies on methylene blue highlighted enhanced due to the presence of Fe^{3+} and its impedance of charge recombination through electron trapping. Caco-2 cell viability studies in the absence of radiation indicated a dose and time dependant toxicity to the PSs. UV irradiation of the nano-PSs resulted in a significant photo-killing effect, with drastic reduction in Caco-2 cell viability. FA conjugation further enhanced photo-induced toxicity. Whilst the synthesised nano-PSs showed potential as a therapeutic agent for PDT, elevated toxicity at higher doses and longer exposure times were of concern and are being addressed in current work via chemical modification for the control of dissolution kinetics. The presence of a magnetic component in Fe_3O_4 will allow exploration of multimodality in the form of MRI imaging and the use of external magnetic fields in assisting tumour localisation.

3.5 References

- [1] T.J. Dougherty, G.B. Grindey, R. Fiel, K.R. Weishaupt, D.G. Boyle, Photoradiation Therapy. II. Cure of Animal Tumors With Hematoporphyrin and Light, *Journal of the National Cancer Institute* 55(1) (1975) 115-121.
- [2] R.R. Allison, Photodynamic therapy: oncologic horizons, *Future Oncology* 10(1) (2014) 123-4.
- [3] J.P. Díaz-Jimenez, R.T. Mezalek, Photodynamic Therapy for Early and Advanced Lung Cancer, in: P.J. Díaz-Jimenez, N.A. Rodriguez (Eds.), *Interventions in Pulmonary Medicine*, Springer New York, New York, NY, 2013, pp. 147-163.
- [4] M. Korbelik, W. Zhang, S. Merchant, Involvement of damage-associated molecular patterns in tumor response to photodynamic therapy: surface expression of calreticulin and high-mobility group box-1 release, *Cancer Immunology, Immunotherapy* 60(10) (2011) 1431-7.
- [5] M.J. Lind, Principles of cytotoxic chemotherapy, *Medicine* 39(12) (2011) 711-716.
- [6] K. Hojan, P. Milecki, Opportunities for rehabilitation of patients with radiation fibrosis syndrome, *Reports of Practical Oncology & Radiotherapy* 19(1) (2014) 1-6.
- [7] J. Sobczyński, H.H. Tønnesen, S. Kristensen, Influence of aqueous media properties on aggregation and solubility of four structurally related meso-porphyrin photosensitizers evaluated by spectrophotometric measurements, *Die Pharmazie - An International Journal of Pharmaceutical Sciences* 68(2) (2013) 100-109.
- [8] H. Nakamura, L. Liao, Y. Hitaka, K. Tsukigawa, V. Subr, J. Fang, K. Ulbrich, H. Maeda, Micelles of zinc protoporphyrin conjugated to N-(2-hydroxypropyl)methacrylamide (HPMA) copolymer for

imaging and light-induced antitumor effects in vivo, *Journal of Controlled Release* 165(3) (2013) 191-198.

[9] L. Cheng, C. Wang, L. Feng, K. Yang, Z. Liu, Functional Nanomaterials for Phototherapies of Cancer, *Chemical Reviews* 114(21) (2014) 10869-10939.

[10] S.S. Lucky, K.C. Soo, Y. Zhang, Nanoparticles in Photodynamic Therapy, *Chemical Reviews* 115(4) (2015) 1990-2042.

[11] X. Feng, S. Zhang, X. Lou, Controlling silica coating thickness on TiO₂ nanoparticles for effective photodynamic therapy, *Colloids and Surfaces B: Biointerfaces* 107(0) (2013) 220-226.

[12] X. Feng, S. Zhang, H. Wu, X. Lou, A novel folic acid-conjugated TiO₂-SiO₂ photosensitizer for cancer targeting in photodynamic therapy, *Colloids and Surfaces B: Biointerfaces* 125(0) (2015) 197-205.

[13] S.G. Kumar, K.S.R.K. Rao, Zinc oxide based photocatalysis: tailoring surface-bulk structure and related interfacial charge carrier dynamics for better environmental applications, *RSC Advances* 5(5) (2015) 3306-3351.

[14] A. Moezzi, A.M. McDonagh, M.B. Cortie, Zinc oxide particles: Synthesis, properties and applications, *Chemical Engineering Journal* 185-186 (2012) 1-22.

[15] J. Li, D. Guo, X. Wang, H. Wang, H. Jiang, B. Chen, The Photodynamic Effect of Different Size ZnO Nanoparticles on Cancer Cell Proliferation In Vitro, *Nanoscale Research Letters* 5(6) (2010) 1063 - 1071.

[16] S. Hackenberg, A. Scherzed, M. Kessler, K. Froelich, C. Ginzkey, C. Koehler, M. Burghartz, R. Hagen, N. Kleinsasser, Zinc oxide nanoparticles induce photocatalytic cell death in human head and neck squamous cell carcinoma cell lines in vitro, *International Journal of Oncology* 37(6) (2010) 1583-1590.

[17] H. Zhang, B. Chen, H. Jiang, C. Wang, H. Wang, X. Wang, A strategy for ZnO nanorod mediated multi-mode cancer treatment, *Biomaterials* 32(7) (2011) 1906-1914.

[18] A.F.M. Ismail, M.M. Ali, L.F.M. Ismail, Photodynamic therapy mediated antiproliferative activity of some metal-doped ZnO nanoparticles in human liver adenocarcinoma HepG2 cells under UV irradiation, *Journal of Photochemistry and Photobiology B: Biology* 138 (2014) 99-108.

[19] X. Wei, W. Wang, K. Chen, ZnO:Er,Yb,Gd Particles Designed for Magnetic-Fluorescent Imaging and Near-Infrared Light Triggered Photodynamic Therapy, *The Journal of Physical Chemistry C* 117(45) (2013) 23716-23729.

[20] X. Feng, H. Guo, K. Patel, H. Zhou, X. Lou, High performance, recoverable Fe₃O₄ZnO nanoparticles for enhanced photocatalytic degradation of phenol, *Chemical Engineering Journal* 244(0) (2014) 327-334.

[21] X. Feng, X. Lou, The effect of surfactants-bound magnetite (Fe₃O₄) on the photocatalytic properties of the heterogeneous magnetic zinc oxides nanoparticles, *Separation and Purification Technology* 147(0) (2015) 266-275.

[22] R. Roy, M. Das, P.D. Dwivedi, Toxicological mode of action of ZnO nanoparticles: Impact on immune cells, *Molecular Immunology* 63(2) (2015) 184-192.

[23] E. Paszko, C. Ehrhardt, M.O. Senge, D.P. Kelleher, J.V. Reynolds, Nanodrug applications in photodynamic therapy, *Photodiagnosis and Photodynamic Therapy* 8(1) (2011) 14-29.

[24] P. Xu, G.M. Zeng, D.L. Huang, C.L. Feng, S. Hu, M.H. Zhao, C. Lai, Z. Wei, C. Huang, G.X. Xie, Z.F. Liu, Use of iron oxide nanomaterials in wastewater treatment: A review, *Science of The Total Environment* 424 (2012) 1-10.

[25] M. Shekofteh-Gohari, A. Habibi-Yangjeh, Facile preparation of Fe₃O₄@AgBr-ZnO nanocomposites as novel magnetically separable visible-light-driven photocatalysts, *Ceramics International* 41(1, Part B) (2015) 1467-1476.

[26] M. Saranya, R. Ramachandran, E.J.J. Samuel, S.K. Jeong, A.N. Grace, Enhanced visible light photocatalytic reduction of organic pollutant and electrochemical properties of CuS catalyst, *Powder Technology* 279 (2015) 209-220.

[27] A. Akhundi, A. Habibi-Yangjeh, Novel magnetically separable g-C₃N₄/AgBr/Fe₃O₄ nanocomposites as visible-light-driven photocatalysts with highly enhanced activities, *Ceramics International* 41(4) (2015) 5634-5643.

- [28] C. Karunakaran, P. Vinayagamoorthy, J. Jayabharathi, Nonquenching of Charge Carriers by Fe₃O₄ Core in Fe₃O₄/ZnO Nanosheet Photocatalyst, *Langmuir* 30(49) (2014) 15031-15039.
- [29] R.J. Lee, P.S. Low, Delivery of liposomes into cultured KB cells via folate receptor-mediated endocytosis, *Journal of Biological Chemistry* 269(5) (1994) 3198-3204.
- [30] K. Patel, B. Sundara Raj, Y. Chen, X. Lou, Cytotoxicity of folic acid conjugated hollow silica nanoparticles toward Caco2 and 3T3 cells, with and without encapsulated DOX, *Colloids and Surfaces B: Biointerfaces* 140 (2016) 213-222.
- [31] T. Mosmann, Rapid colorimetric assay for cellular growth and survival: Application to proliferation and cytotoxicity assays, *Journal of Immunological Methods* 65(1-2) (1983) 55-63.
- [32] C. Haavik, S. Stolen, H. Fjellvag, M. Hanfland, D. Hausermann, Equation of state of magnetite and its high-pressure modification: Thermodynamics of the Fe-O system at high pressure, *American Mineralogist* 85 (2000) 514-523.
- [33] Y.-N. Xu, W.Y. Ching, Electronic, optical, and structural properties of some wurtzite crystals, *Physical Review B* 48(7) (1993) 4335-4351.
- [34] M. Ramani, S. Ponnusamy, C. Muthamizhchelvan, J. Cullen, S. Krishnamurthy, E. Marsili, Morphology-directed synthesis of ZnO nanostructures and their antibacterial activity, *Colloids and Surfaces B: Biointerfaces* 105(0) (2013) 24-30.
- [35] G. Xiong, U. Pal, J.G. Serrano, K.B. Ucer, R.T. Williams, Photoluminescence and FTIR study of ZnO nanoparticles: the impurity and defect perspective, *physica status solidi (c)* 3(10) (2006) 3577-3581.
- [36] P. Huang, L. Bao, C. Zhang, J. Lin, T. Luo, D. Yang, M. He, Z. Li, G. Gao, B. Gao, S. Fu, D. Cui, Folic acid-conjugated Silica-modified gold nanorods for X-ray/CT imaging-guided dual-mode radiation and photo-thermal therapy, *Biomaterials* 32(36) (2011) 9796-9809.
- [37] S.K. Sahu, S.K. Mallick, S. Santra, T.K. Maiti, S.K. Ghosh, P. Pramanik, In vitro evaluation of folic acid modified carboxymethyl chitosan nanoparticles loaded with doxorubicin for targeted delivery, *Journal of Materials Science : Materials in Medicine* 21(5) (2010) 1587-1597.
- [38] A. Huang, J. Caro, Shape evolution of zinc oxide from twinned disks to single spindles through solvothermal synthesis in binary solvents, *Journal of Crystal Growth* 312(20) (2010) 2977-2982.
- [39] S. Xing, Z. Zhou, Z. Ma, Y. Wu, Characterization and reactivity of Fe₃O₄/FeMnOx core/shell nanoparticles for methylene blue discoloration with H₂O₂, *Applied Catalysis B: Environmental* 107(3-4) (2011) 386-392.
- [40] A. Tyagi, A. Penzkofer, Fluorescence spectroscopic behaviour of folic acid, *Chemical Physics* 367(2-3) (2010) 83-92.
- [41] N.N. Nassar, A. Ringsred, Rapid Adsorption of Methylene Blue from Aqueous Solutions by Goethite Nanoadsorbents, *Environmental Engineering Science* 29(8) (2012) 790-797.
- [42] T.-S. Ding, X.-C. Huang, Y.-L. Luo, H.-Y. Hsu, In vitro investigation of methylene blue-bearing, electrostatically assembled aptamer-silica nanocomposites as potential photodynamic therapeutics, *Colloids and Surfaces B: Biointerfaces* 135 (2015) 217-224.
- [43] C.-H. Wu, H.-W. Chang, J.-M. Chern, Basic dye decomposition kinetics in a photocatalytic slurry reactor, *Journal of Hazardous Materials* 137(1) (2006) 336-343.
- [44] Y.H. Tan, P.S. Goh, A.F. Ismail, Development of photocatalytic coupled zinc-iron oxide nanoparticles via solution combustion for bisphenol-A removal, *International Biodeterioration & Biodegradation* 102 (2015) 346-352.
- [45] B. Zödl, M. Zeiner, M. Sargazi, N.B. Roberts, W. Marktl, I. Steffan, C. Ekmekcioglu, Toxic and biochemical effects of zinc in Caco-2 cells, *Journal of Inorganic Biochemistry* 97(4) (2003) 324-330.
- [46] Y. Yu, J. Duan, Y. Li, Y. Yu, M. Jin, C. Li, Y. Wang, Z. Sun, Combined toxicity of amorphous silica nanoparticles and methylmercury to human lung epithelial cells, *Ecotoxicology and Environmental Safety* 112 (2015) 144-152.
- [47] I.-Y. Kim, E. Joachim, H. Choi, K. Kim, Toxicity of silica nanoparticles depends on size, dose, and cell type, *Nanomedicine: Nanotechnology, Biology and Medicine* 11(6) (2015) 1407-1416.
- [48] J.-S. Chang, K.L.B. Chang, D.-F. Hwang, Z.-L. Kong, In Vitro Cytotoxicity of Silica Nanoparticles at High Concentrations Strongly Depends on the Metabolic Activity Type of the Cell Line, *Environmental Science & Technology* 41(6) (2007) 2064-2068.

[49] E.-Q. Song, Z.-L. Zhang, Q.-Y. Luo, W. Lu, Y.-B. Shi, D.-W. Pang, Tumor Cell Targeting Using Folate-Conjugated Fluorescent Quantum Dots and Receptor-Mediated Endocytosis, *Clinical Chemistry* 55(5) (2009) 955-963.

CHAPTER 4

4 Surface modification of Fe₃O₄-ZnO hybrid nanoparticles to produce a multimodal photosensitiser

4.1 Introduction

As discussed in Chapter 3 the development of photosensitisers (PSs) with efficient photocatalytic properties and selectivity toward cancerous cells has seen growing interest for applications in photodynamic therapy (PDT) [1]. The inherent toxicity and inefficiency in photocatalysis of titanium dioxide (TiO₂) and zinc oxide (ZnO), as well as the inability to target diseased sites were previously mentioned as limiting factors for transition of semiconductor materials to clinical use in PDT [2, 3]. Chapter 3 addressed some of these limitations via hybridisation of ZnO using iron oxide (Fe₃O₄). The resultant heterogeneous photosensitiser (PS) outperformed its conventional ZnO counterpart. Furthermore, surface modification to form a core shell, silanised and folic acid decorated PS highlighted the potential for use in PDT via photokilling of colorectal adenocarcinoma (Caco-2) cells. While photoefficiency and targeting were enhanced, metal toxicity was still an issue, where, in the absence of radiation, prolonged exposure and PS concentrations $\geq 50 \mu\text{g.mL}^{-1}$ resulted in a significant reduction of Caco-2 cell viability. This chapter details further surface modification of the existing iron oxide – zinc oxide PSs to increase their potential as a viable candidate for applications in cancer treatment.

The modification of therapeutic and diagnostic agents with polyethylene glycol (PEG) has been termed PEGylation. Work with PEGylated nanoparticles (NPs) in the early 1990's focussed on drug delivery applications, where PEG incorporation was found to increase NP blood circulation half-lives [4-6]. Longer blood circulation was later shown to be a result of reduced uptake by mononuclear phagocytes [7], as well as via provision of a thick and dynamic hydration shell, rendering the adsorption of biomacromolecules to PEG coated surfaces thermodynamically unfavourable [8]. The significance of this outcome was highlighted by increased tumour localisation, where NPs with longer circulation times were better able to take advantage of the enhanced permeability and retention (EPR) effect [9]. The mechanism of these effects have more recently been explained through prevention of protein corona formation, whereby the tendency of protein adsorption onto PEGylated surfaces is mitigated, masking NPs from the body's immune response [10]. Furthermore, formation of a protein corona has also been shown to hinder interactions between targeting ligands with cellular membranes [11] such a disadvantage provides further credence for PEGylation. The effectiveness of "stealth" behaviour imparted upon NPs through PEGylation has been shown to be critically dependant on the density of the surface PEG chains [12], which in turn controls their conformation; a low PEG density instigates a "mushroom" like conformation while higher densities result in a "brush" like conformation [10, 13, 14] as illustrated in Figure 4-1. As explained by Yang and co-workers [15], the resultant PEG conformation is dictated by grafting distance (D : the distance between closest neighbouring PEG anchors, inversely proportional to density) and the Flory radius (R_F) of the PEG coils, which is directly related to the molecular weight of the PEG used. They further showed that a dense brush conformation was essential to evading uptake by macrophages in vitro and extending particle circulation times in vivo.

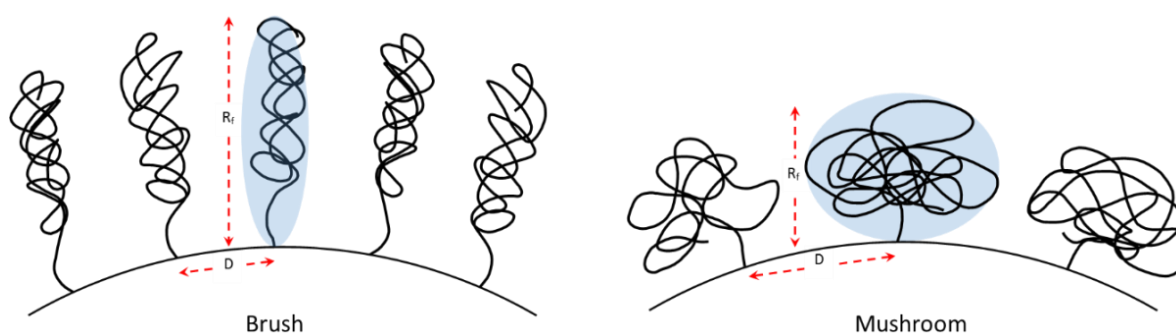


Figure 4-1. An illustration depicting the brush and mushroom conformations of PEG chains.

Whilst PEGylation has allowed for a reduced uptake by immune cells, it has also been reported to reduce NP uptake in cultured cells *in vitro* [12, 16]; an undesirable quality when considering the delivery of a therapeutic payload to target cells. As such, employing targeting ligands when utilising PEG for enhanced tumour localisation is a must if cellular uptake is a prerequisite of the treatment modality. The work of Bartlett [17] and Kirpotin [18] clearly illustrates that while PEGylated NPs are able to agglomerate within tumour interstitium, concomitant use of a receptor binding ligand, facilitates cellular uptake of the NPs, preventing recirculation into the bloodstream.

Clearly, the surface characteristics of nanoparticulate PSs are paramount in the determination of their biological fate and as discussed in Chapter 3, their photocatalytic efficiency [19, 20]. This chapter details surface modification of the hybrid iron oxide-zinc oxide (FZ) NPs described in Chapter 3, with PEG to include also a folic acid (FA) targeting ligand. Whilst enhancing biodistribution and facilitating cellular uptake are clear goals for making a successful transition to efficacious PDT, the ability to determine the PSs biodistribution is also of importance. As such, the PS platform was also modified with 5-dimethylaminonaphthalene sulfonyl chloride (dansyl chloride, DnCl), a fluorophore well established in its use for the derivatisation of amino acids and labelling of drugs and proteins for applications in cellular imaging [21-23]. DnCl offers a high emission quantum yield and a large Stokes shift with respective excitation and emission wavelengths of 340 nm and 520 nm [24], additionally the synthetic flexibility afforded by the sulfonic acid moiety afforded facile preparation of a novel fluorescent PS. Incorporation of DnCl, would not only allow for visualisation of the PS's biodistribution, but adds an element of multimodality with potential applications in diagnostics and also highlights the versatility of the synthetic approach used. The work herein describes PEGylation of the silanised FZ NPs (FZ-S) prepared in chapter 3, to produce PSs with varying PEG density; viz. FZ-S-PEG25 and FZ-S-PEG50 in order of increasing PEG content. A FA targeting ligand was then covalently bound to the PEG to produce FZ-S-PEG-FA25 and FZ-S-PEGFA50 in order of increasing FA content. DnCl was used to prepare the novel fluorescent FZ-S-DnS50 PS. PEG was again used as a spacer to produce FZ-S-PEG-DnS50. To assess the effect of surface modification on photocatalytic efficiency, methylene blue (MB) was used as a model organic compound in photodegradation studies at various pH conditions. Thermogravimetric analysis was used to quantify the various surface conjugated moieties and estimate the density and conformation of PEG groups. The suitability of the prepared

PSs for future biological testing, with regards to surface modification and photocatalytic performance shall be discussed.

4.2 Materials and methods

4.2.1 Materials

The following chemicals were purchased from Sigma-Aldrich Australia: Zinc acetate dihydrate ($\geq 98\%$, $\text{Zn}(\text{Ac})_2 \cdot 2\text{H}_2\text{O}$), tetraethyl orthosilicate (99.999%, TEOS), (3-aminopropyl) triethoxysilane (99%, APTES), (3-glycidyloxypropyl) trimethoxysilane ($\geq 98\%$, GPS), α -(2-aminoethyl)- ω -hydroxy poly(oxyethylene) (M_p 3000, PEG), N-hydroxysuccinimide (NHS), N,N'-dicyclohexyl carbodiimide (DCC), reagent grade triethylamine, folic acid (97%, FA) and 5-dimethylaminonaphthalene sulfonyl chloride (98%, dansyl chloride, DnCl). Methylene blue (MB), anhydrous ether, dimethyl sulfoxide (DMSO) and diethylene glycol (99%, DEG) were sourced from Alfa Aesar.

4.2.2 Chemical synthesis

The synthesis of hybrid iron/zinc oxide (FZ) nanoparticles was carried out as previously reported [19]. Subsequent synthetic stages are illustrated schematically in Figure 4-2 and are outlined below. Table 4-1 summarises various reactant amounts utilised in the different stages of surface functionalisation and also details the corresponding quantification estimates of functional surface groups as measured via thermogravimetric analysis (TGA).

4.2.2.1 *Synthesis of core-shell hybrid FZ-S-NH₂50 and FZ-S-GPS NPs*

Silanisation of the FZ hybrid NPs to produce silica coated FZ-S NPs was achieved through a sol-gel process, employing TEOS ($0.908 \text{ mmol.g}^{-1}$) as per our previous work [25]. The surface silica layer was activated with reactive functional groups. Amine functional groups were introduced using APTES (Figure 4-2a) and epoxide functional groups were added via GPS (Figure 4-2b). The final surface density of PEG, FA and DnS molecules was controlled at this stage through variation of APTES and GPS quantity. Amination of the silica shell required drop-wise addition of APTES in 20 mL ethanol ($0.523 \text{ mmol.g}^{-1}$ equivalent NH_2) to a FZ-S NP suspension, followed by 2 hours mechanical stirring at room temperature. The aminated FZ-S NPs (FZ-SNH₂50) were collected via external magnet and were washed

three times sequentially in ethanol followed by milli-Q water using ultra-sonication. TGA quantification yielded an NH_2 concentration of $0.459 \text{ mmol.g}^{-1}$ on the surface of FZ-S- NH_2 50 NPs (88% reaction yield). GPS functionalised NPs (FZ-S-GPS; Figure 4-2b) were prepared in the same way as aminated particles, however APTES was replaced with GPS (quantity in Table 1). Quantification via TGA yielded 0.232 and $0.461 \text{ mmol.g}^{-1}$ of epoxide functional groups for FZ-S-GPS25 and FZ-S-GPS50 respectively, (90 and 92% reaction yields).

4.2.2.2 *Synthesis of FZ-S-DnS50 NPs*

Dry acetone was first prepared via distillation of acetone after treating with calcium chloride overnight. FZ-S- NH_2 50 NPs ($9.18 \text{ } \mu\text{mol}$ equivalent NH_2) were dispersed in 40 mL of dry acetone containing 0.25 mL (1.79 mmol) triethylamine. DnCl (10 mg , $37 \text{ } \mu\text{mol}$) was dissolved in 10 mL dry acetone and then added to the FZ-S- NH_2 50 dispersion. The reaction was stirred at room temperature for 24 h in the dark (Figure 4-2a). The FZ-S-DnS50 product was then isolated and cleaned via external magnet, washing sequentially in acetone and milli Q water three times each with ultra-sonication.

4.2.2.3 *Synthesis of FZ-S-PEG and FZ-S-PEG-DnS NPs*

PEGylated hybrid NPs, FZ-S-PEG25 and FZ-S-PEG50 (Figure 4-2b), were prepared by dispersing the FZ-S-GPS precursor (refer to Table 1 for reactant quantities) in 10 mL of milli Q water and heating to $65 \text{ }^\circ\text{C}$. α -(2-aminoethyl)- ω -hydroxy poly(oxyethylene) (PEG; dissolved in 10 mL milli Q water, quantity in Table 4-1) was added to the NP dispersion under mechanical stirring. The temperature was maintained for a further 6 h with constant stirring. PEGylated NPs were termed FZ-S-PEG25 and FZ-S-PEG50 in order of increasing PEG content and were washed three times sequentially with milli Q water, acetone and dry acetone. Dansylation of FZ-S-PEG50 (Figure 4-2c) was carried out as per section 2.2.2 (refer to Table 4-1 for reactant quantities) and the final FZ-S-PEG-DnS50 product was stored as a suspension in milli Q water in the dark.

4.2.2.4 *Synthesis of FZ-S-PEG-FA NPs*

The NHS ester of FA (NHS-FA) was synthesised first via a DCC coupling method as reported previously [26] (not shown in Figure 4-2). The NHS-FA intermediate facilitated conjugation of FA to FZ-S-PEG. FZ-S-PEG NPs were dispersed in 10 mL of $\text{Na}_2\text{CO}_3/\text{NaHCO}_3$

buffer (pH 9.30) using sonication for 10 min. NHS-FA was added drop wise to the NP suspension (Figure 4-2d) with constant mechanical stirring for one hour. FZ-S-PEG-FA NPs were collected via external magnet and were washed in conjunction with sonication 5 times in DMSO followed by 3 times with milli-Q water. The prepared FA conjugated NPs were termed FZ-S-PEG-FA25 and FZ-S-PEG-FA50 in order of increasing FA content. Reactant quantities used are summarised in Table 4-1 below.

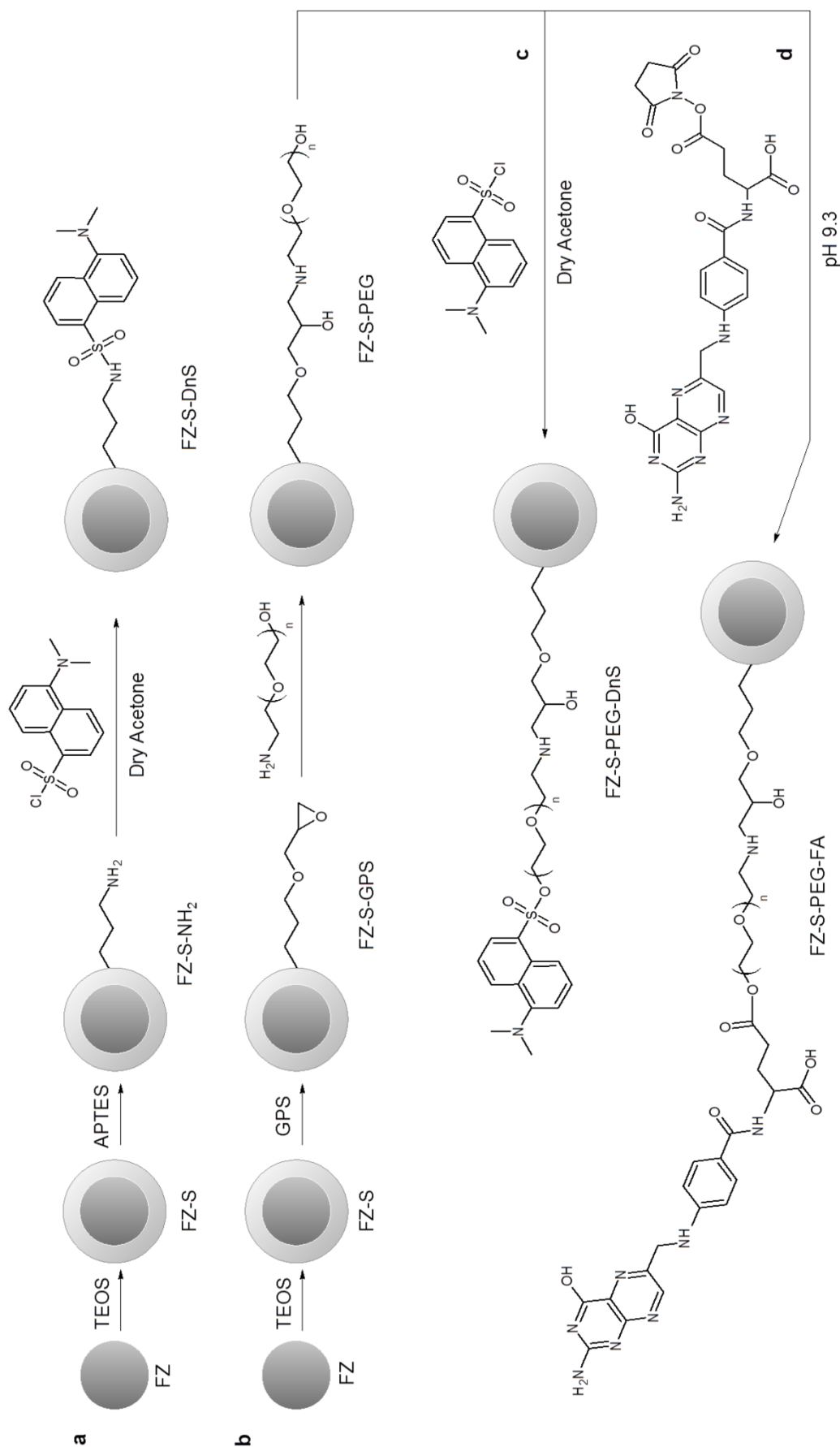


Figure 4-2. Synthetic scheme detailing the preparation of (a) dansylated hybrid NPs FZ-S-DnS, (b) PEGylation to produce FZ-S-PEG and subsequently (c) FZ-S-PEG-DnS and (d) FZ-S-PEG-FA.

Table 4-1. Quantity of reactants used to prepare specified samples and the measured molar concentration of corresponding functional groups per gram of NP.

Sample	TEOS added (mmol.g ⁻¹)	Quantity (mmol.g ⁻¹)											
		Added APTES	Measured NH ₂	Added GPS	Measured epoxide	Added PEG	Measured PEG	Added DnCl	Measured DnS	Added NHS-FA	Measured FA		
FZ-S	0.908												
FZ-S-NH ₂ 50	0.908	0.523	0.459										
FZ-S-DnS50	0.908	0.523	0.459					0.911	0.061				
FZ-S-GPS25	0.908			0.257	0.232								
FZ-S-GPS50	0.908			0.501	0.461								
FZ-S-PEG25	0.908			0.257	0.232	0.500	0.047						
FZ-S-PEG50	0.908			0.501	0.461	1.005	0.092						
FZ-S-PEG-DnS50	0.908			0.501	0.461	1.005	0.092	0.250	0.052				
FZ-S-PEG-FA25	0.908			0.257	0.232	0.500	0.047					0.150	0.030
FZ-S-PEG-FA50	0.908			0.501	0.461	1.005	0.092					0.302	0.058

4.2.3 Nanoparticle characterisation

Geometric particle size was evaluated using high resolution TEM (JOEL JSM 2011, equipped with a Gatan digital camera) as per previously reported method [3]. Hydrodynamic particle size and size distribution were assessed via dynamic light scattering (DLS) using a Zetasizer Nano-ZS from Malvern Instruments. Zeta potential was carried out using the same instrument. Sodium chloride (10 ml, 0.01 M) was used as a conductive regulator. The pH of the sodium chloride solution was adjusted to 4.0, 6.0, 7.4 and 9.3 using an aqueous solution of NaOH (0.01 M) and HCl (0.01 M). Samples (1 mg) were dispersed in the resulting solutions (10 mL) using ultra sonication (10 min) prior to measurement.

A Thermo Scientific Nicolet is50 FT-IR spectrometer equipped with an automated beam splitter exchanger, affording both mid-IR and far-IR capabilities, was used to identify various chemical functional groups. Quantification of organic moieties bound to the NP surfaces was carried out using thermogravimetric analysis (TGA; Mettler Toledo) as reported previously [27]. Estimation of the density of PEG surface coverage was carried out using an average FZ NP diameter of 13.74 nm and a silica shell thickness of 1.86 nm as obtained via TEM. To approximate the conformational regime of PEG the Flory radius R_F and the grafting distance D were determined using the following equations obtained from Yang et al. [15]: $R_F = \alpha N^{3/5}$, $D = 2(A/\pi)^{1/2}$ and $A = 1/P$; where α is the monomer length of PEG (oxyethylene; 0.35 nm), N the number of PEG repeat units ($N = 68$), A is the area occupied per PEG chain and P is the density of PEG surface coverage (obtained via TGA). Mushroom and brush conformations were defined by $R_F/D \leq 1$ and $R_F/D > 1$ respectively and the dense brush conformation was defined as $R_F/D > 2.8$.

Elemental iron and zinc content within the NPs was quantified via ICP-OES (Perkin Elmer Optima 8300 ICP-OES spectrometer). Analysis was performed at wavelengths of 238.2 and 206.2 nm respectively for iron and zinc. Samples were prepared as per section 2.3 in Chapter 3.

Fluorescence spectroscopy was carried out using an Aligent Technologies Cary Eclipse fluorescence spectrophotometer with excitation wavelengths of 277 nm for all synthesised NPs, with 283 nm for FA conjugated NPs and 327 nm for dansylated particles. Spectra were obtained using a scan rate of 600 nm.min⁻¹ with 10 co-added scans.

Fluorescent micrographs of FZ-S-PEG-DnS and the control FZ-S-PEG NPs were obtained using an Olympus fluorescence microscope equipped with a Xenon arc lamp. An

excitation wavelength of 335 nm was used with a 510 nm long pass emission filter. Aqueous dispersions of FZ-S-PEG-DnS were prepared at concentrations of 25 and 100 $\mu\text{g}\cdot\text{mL}^{-1}$ with control NPs having a concentration of 100 $\mu\text{g}\cdot\text{mL}^{-1}$ also. Dispersions were drop cast on to pre cleaned glass slides. A magnification of 240x was used for all imaging.

4.2.4 Adsorption and photoreactivity study

Adsorption and photocatalytic properties of FZ, FZ-S, FZ-S-PEG, FZ-S-PEG-DnS and FZ-S-PEG-FA NPs were evaluated through measurement of the MB concentration of solutions containing PSs without and with exposure to UV radiation, respectively, over time. Reaction solutions had a MB concentration of 10 $\text{mg}\cdot\text{L}^{-1}$ (pH 4.0, 6.0, 7.4 or 9.3) and a photocatalyst concentration of 325 $\text{mg}\cdot\text{L}^{-1}$. The experimental setup for adsorption and photodegradation was the same as that described in section 2.4 of Chapter 3. Adsorption percentage was determined via ratio of MB concentration at time t (C_t), divided by the initial MB concentration (C_0) and degradation percentage was determined by dividing C_t by the MB concentration at $t = 90$ min (C_0').

4.3 Results and discussion

4.3.1 Synthesis and characterisation of FZ-S-PEG, FZ-S-PEG-FA and FZ-S-PEG-DnS

PSs with various surface modifications were prepared according to Figure 4-2. FZ hybrid nanoparticles were first prepared according to a previously reported method [19]. The hybrid core was coated with a thin layer of silica which was subsequently functionalised with 3-aminopropyl or 3-glycidyloxypropyl functional groups. TEOS and either APTES or GPS were used simultaneously in these reactions. DnCl was then conjugated to the aminated NPs to produce the PS FZ-S-DnS50. GPS functionalised NPs were subject to PEGylation to produce the PSs FZ-S-PEG25 and FZ-S-PEG50. Subsequent esterification allowed the preparation of the PEGylated PSs FZ-S-PEG-DnS50 and FZ-S-PEG-FA. FA content was varied by altering the ratio of TEOS:GPS as per Table 1 resulting in FZ-S-PEG-FA25 and FZ-S-PEG-FA50 in order of increasing FA content.

Size and size distribution of the PSs were evaluated via DLS and TEM and are displayed in Figure 4-3. The hybrid FZ core particles had a hydrodynamic diameter of 43 ± 11 nm. This compared to a geometric diameter of 13.74 ± 2.22 nm obtained via TEM (Figure 4-3a). Hydrodynamic diameters are known to be larger than their geometric

counterparts and this observation has been reported previously in published work [27]. Furthermore, the large discrepancy in size measurements between DLS and TEM may be accounted for by aggregation of the NPs in dispersions used for DLS. Coating with silica resulted in an increase in the geometric diameter to 17.46 ± 2.82 nm, which corresponded to a silica shell thickness of 1.86 nm (Figure 4-3b). Conjugation of PEG showed no significant increase in the thickness of the shell component when imaged via TEM (Figure 4-3c and d). A reduction in the polydispersity index measured by DLS was observed upon PEGylation (0.253 , FZ; 0.181 , FZ-S-FA; 0.101 for FZ-S-PEG-FA), which suggests a possible reduction in aggregation afforded by inclusion of the polymer spacer.

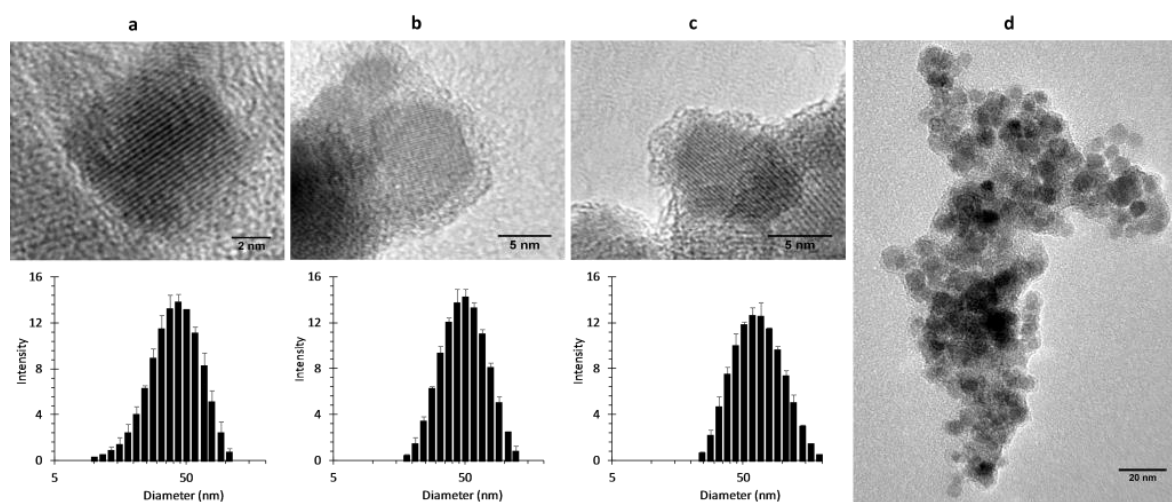


Figure 4-3. TEM micrographs (above) and DLS size distributions (below) of (a) FZ, (b) FZ-S-FA and (c) FZ-S-PEG-FA nanoparticles. Where (d) is a lower magnification TEM micrograph of FZ-S-PEG-FA NPs.

FTIR was used to confirm the successful modification of the PS surfaces with organic moieties and spectra are displayed in Figure 4-4, with Figure 4-4 showing spectra of free FA, DnCl and PEG for comparison. Stretching vibrations corresponding to Fe–O and Zn–O were evident in all spectra and corresponded well with literature [28, 29]. The appearance of a broad band between 1000 cm^{-1} and 1200 cm^{-1} in the spectra of FZ-S-NH₂ (Figure 4-4a) and FZ-S-GPS (Figure 4-4b) corresponded to the asymmetric bending and stretching vibrational modes of siloxane groups [30] confirming silanisation. Amine functionalisation of the silica shell (Figure 4-4a) was confirmed by the appearance of bands at 1603 cm^{-1} and 1625 cm^{-1} , indicative of N–H bending and NH₃⁺ deformation vibrational modes [3]. GPS functionalisation of the silica shell was validated by the emergence of a band at 951 cm^{-1} (Figure 4-4b) corresponding to the ring deformation mode of the epoxy functional group

[24]. Successful dansylation to form the FZ-S-DnS PS was confirmed by the presence of new bands at 1152 cm^{-1} and 1209 cm^{-1} corresponding to the stretching vibrations of C-C and S=O respectively (Figure 4-4a) [24]. The weaker signals at 1371 and 1565 cm^{-1} were ascribed to C-CH bending vibrations of the aromatic ring within the dansyl group [31].

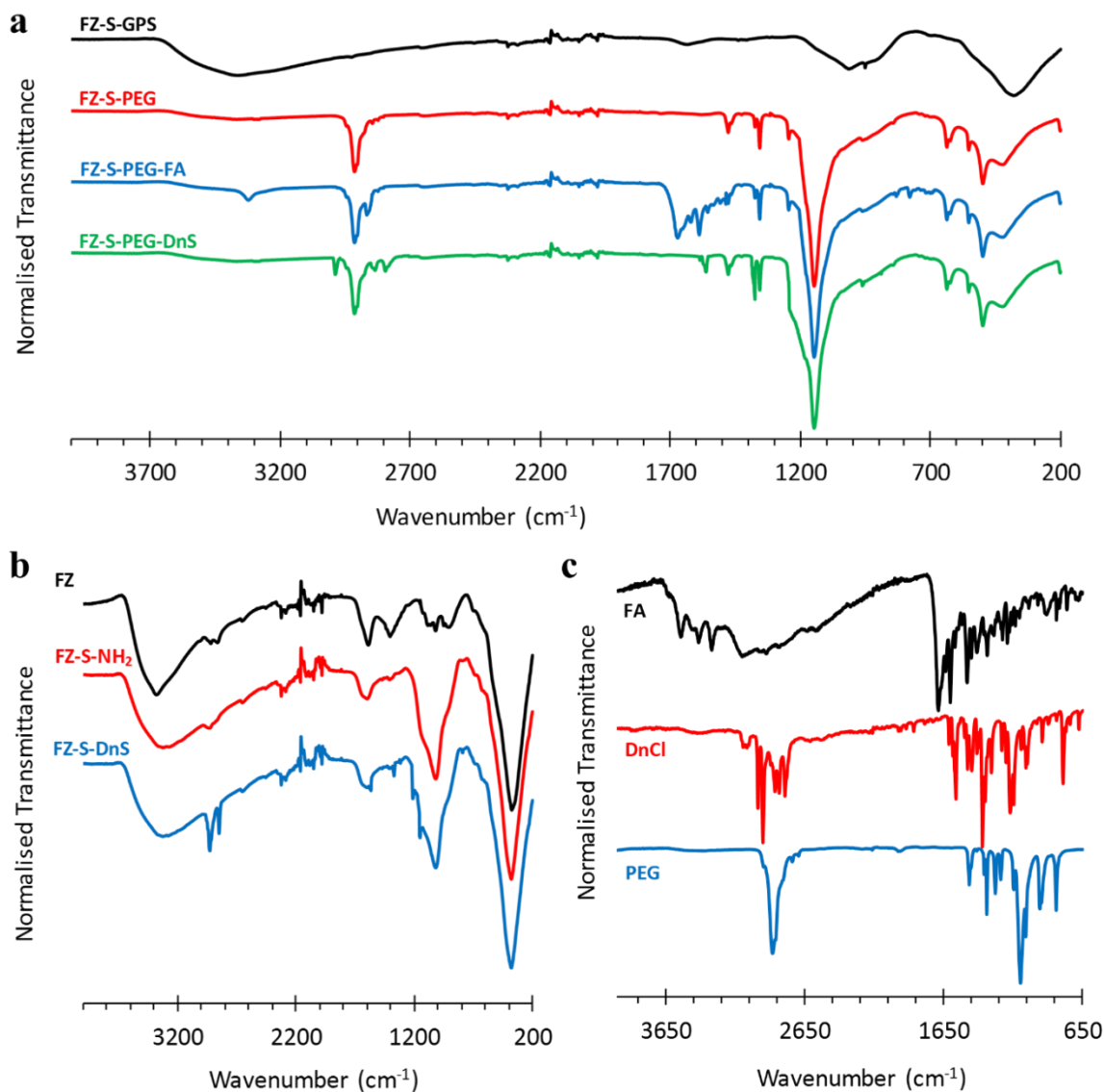


Figure 4-4. FTIR spectra detailing (a) GPS functionalisation, PEGylation and conjugation of FA and the dansyl fluorophore to include the PEG spacer. (b) amination and dansylation without a PEG spacer and (c) free FA, DnCl and PEG molecules used in the synthesis.

PEGylation was confirmed in the spectra of FZ-S-PEG, FZ-S-PEG-Dns and FS-S-PEG-FA by appearance of the strong signal at 1146 cm^{-1} , corresponding to the C-O stretching vibrational band (Figure 4-4b). The appearance of the asymmetric and symmetric stretching vibrational bands of CH₂ groups between 2800 and 2970 cm^{-1} as well as weaker signals at 1478 and 1356 cm^{-1} corresponding to H-C-H bending vibrational modes, further confirmed successful PEGylation [24]. Attachment of FA to produce FZ-S-PEG-FA gave rise

to several new bands between 1470 and 1700 cm^{-1} (Figure 4-4b). The signal at 1670 cm^{-1} corresponded to the C=O stretching vibration characteristic to FA [32]. The shoulder at 1643 cm^{-1} corresponded to the bending vibration of the newly formed O-H bond between PEG and FA and the signal at 1611 cm^{-1} corresponded to the deformation vibrational mode of NH_2 . The signals at 1587 cm^{-1} and 1537 cm^{-1} were associated with the C-N and N-H bending modes of the amide band II [33]. Dansylation of the FZ-S-PEG-DnS PS was confirmed by the appearance of a new shoulder on the strong C-O signal at 1160 cm^{-1} (Figure 4-4b), which correlated to the C-N stretching vibration of the dansyl group. Further contribution to the shoulder was ascribed to stretching of the O=S=O group at 1210 cm^{-1} . The new bands at 1375 and 1561 cm^{-1} were assigned to the C-CH stretching vibrations of the aromatic ring structure within the dansyl moiety and the asymmetric stretching frequencies of CH_3 groups of the dansyl moiety were appeared at 2985 cm^{-1} [31], further confirming successful dansylation.

Example TGA curves for FZ-S-PEG-FA25 and FZ-S-DnS50 together with their intermediates are displayed in Figure 4-5a and b respectively. Similar data was obtained for FZ-S-PEG-DnS and its constituents. All NPs were subject to a mass loss region between 35-110 $^\circ\text{C}$ corresponding to evaporation of adsorbed water. More significant losses were observed between 110-585 $^\circ\text{C}$ and were correlated to loss of the various functional groups chemically bound to the NP surfaces.

Estimation based on this data allowed quantification of various functional groups as summarized in Table 1. Dansylation of FZ-S- NH_2 50 to produce FZ-S-DnS50 saw an estimated dansyl moiety concentration of 0.061 mmol.g^{-1} at a reaction yield of 13% (Figure 4-5b). PEGylation was achieved via nucleophilic substitution of the epoxide groups on FZ-S-GPS NPs. For FZ-S-PEG25 (Figure 4-5a) the reaction yield was 20% and gave an estimated 0.047 mmol.g^{-1} of PEG. The PEG content on FZ-S-PEG50 (TGA curve not shown) was estimated to be 0.092 mmol.g^{-1} with a reaction yield of 20%. Subsequent reaction to form FZ-S-PEG-DnS50 (TGA curve not shown) yielded a dansyl fluorophore concentration of 0.052 mmol.g^{-1} , with a reaction yield of 57%. The reaction yield for PEGylated dansyl bound PSs was about 4 times greater than its non-PEGylated counterpart. Conjugation of DnCl in either case was achieved via nucleophilic substitution to form a sulfonate ester; via $-\text{NH}_2$ for FZ-S-DnS50 and via $-\text{OH}$ for FZ-S-PEG-DnS50. The latter being a weaker nucleophile suggests the PEGylated analogue should produce the lower reaction yield. However, as explained by Pourfallah et al. the presence of the inert hydrophilic PEG spacer may have

resulted in a more facile reaction, with direct attachment to the NP surfaces being more sterically hindered [24] thus resulting in a higher reaction yield. Folate conjugation was also achieved via reaction with epoxide groups and for FZ-S-PEG-FA(25) the FA content was calculated at $0.030 \text{ mmol.g}^{-1}$ (Figure 4-5a) equating to a reaction yield of 64%. For FZ-S-PEG-FA50 (TGA curve not shown) the FA content was $0.058 \text{ mmol.g}^{-1}$ corresponding to a reaction yield of 63%.

Quantification of PEG content revealed 0.047 and $0.092 \text{ mmol.g}^{-1}$ respectively for FZ-S-PEG25 and FZ-S-PEG50 correlating to an estimated PEG coverage density of 0.31 and 0.62 PEG.nm^{-2} through use of particle size and shell thickness. These values translated to $R_F/D = 2.2$ and $R_F/D = 3.1$ for FZ-S-PEG25 and FZ-S-PEG50 respectively. The former value equating 2.2 suggests a brush PEG conformation and the latter being greater than 2.8 corresponds to a dense brush conformation. These estimations signify the potential for protein and macrophage resistance of the synthesized NPs and compare well to several reports in reviewed literature [14].

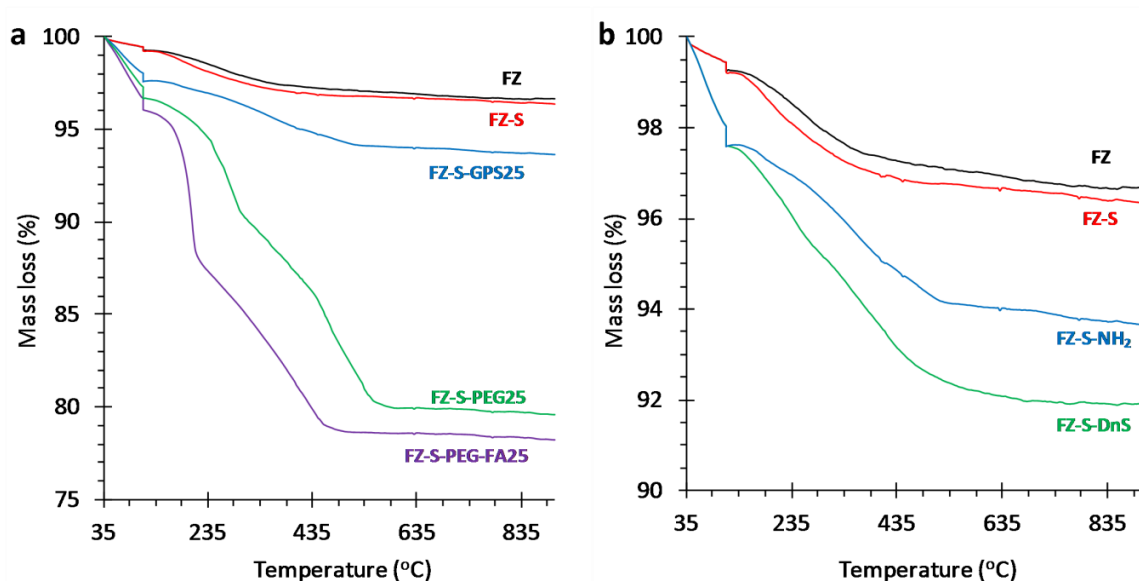


Figure 4-5. Mass loss percentage curves for (a) FZ-S-PEG-FA25 and (b) FZ-S-DnS and their constituent NPs as obtained via thermogravimetric analysis.

Fluorescence emission spectra of the synthesised PSs are presented in Figure 4-6 below. Emission corresponding to the dansyl moiety was investigated through use of an excitation wavelength of 327 nm (Figure 4-6a) and the concentration of the dansyl group was held constant for DnCl, FZ-S-DnS50 and FZ-S-PEG-DnS50, with FZ, FZ-S and FZ-S-PEG50 not containing any dansyl groups. The emission at $\lambda_{\text{max}} = 498 \text{ nm}$ observed for free DnCl

(Figure 4-6a) was attributed to charge transfer from the tertiary amine group to the naphthalene ring [34]. The fluorescence emission was enhanced for FZ-S-DnS50, likely due to the intermolecular charge transfer from the dimethyl amino electron donor group to the electron withdrawal sulphonamide group as per the red chemical scheme insert in Figure 4-6a [34-36]. Addition of the PEG spacer to form FZ-S-PEG-DnS50 saw a further increase in the emission intensity and a shift to 508 nm. Bonding with PEG was facilitated by the more electronegative oxygen atom, thus affording a greater electron withdrawing capacity through the sulfonic ester group (black chemical scheme insert in Figure 4-6b). Hence, an enhanced push-pull effect would result, therefore increasing the emission intensity. An increase in the charge transfer would also result in a decrease in the energy gap between the highest occupied molecular orbital and the lowest unoccupied molecular orbital, explaining the red shift in emission wavelength [37]. Emission spectra of FZ, FZ-S and FZ-S-PEG50 did not contain the characteristic emission band of the dansyl moiety (Figure 4-6a). All spectra in Figure 4-6a also exhibited an emission centered at 353 nm which was attributed to electron transitions associated with ZnO. Interestingly, spectra of FZ-S-DnS50 and FZ-S-PEG-DnS50 also contained a shoulder at 388 nm (Figure 4-6a) that was absent in the spectra of free DnCl and NPs not containing the dansyl moiety.

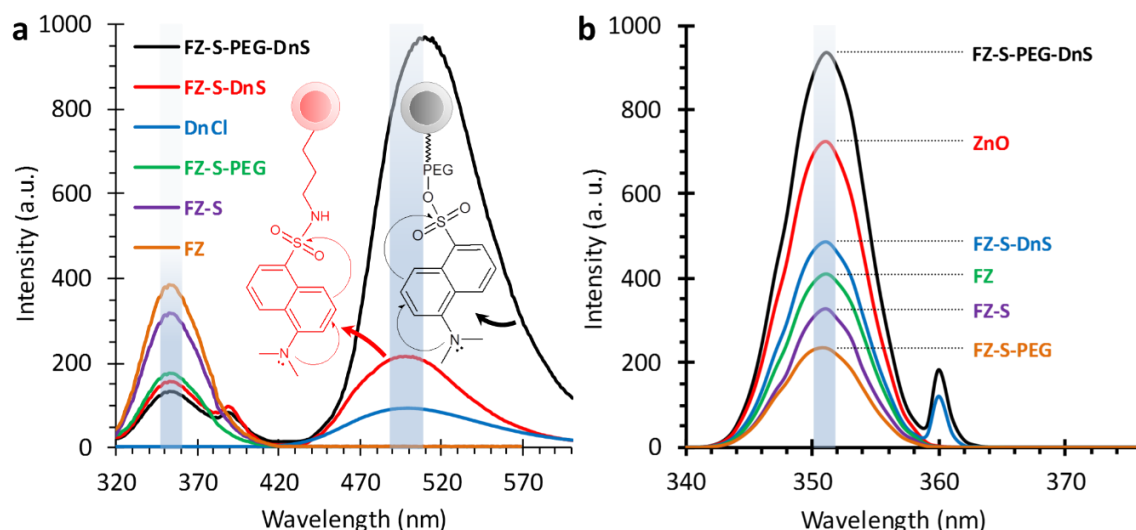


Figure 4-6. Fluorescence emission spectra using an excitation wavelength of (a) 327 nm and (b) 277 nm. The chemical scheme inserts in a) represent variations in electronic charge transfer resulting from changes in bond type and are colour coded to match respective spectra.

Fluorescence emission associated with the ZnO component of the dansylated NPs was investigated through use of an excitation wavelength of 277 nm and spectra are

displayed in Figure 4-6b. The zinc content in each sample was kept constant. All PSs exhibited an emission at $\lambda_{\text{max}} = 351$ nm in accordance with analogous work carried out in Chapter 3. Emission intensity of the FZ PS was lower than that of pure ZnO as expected and reported previously in published work [19] and Chapter 3. Incorporation of the silica shell once again saw a reduction in the emission intensity due to shielding, also as expected [25]. PEGylation to form FZ-S-PEG saw a further reduction in the emission intensity and was also attributed to shielding due to presence of the bulky PEG molecules. Direct conjugation of the dansyl fluorophore saw an increase in fluorescent intensity, ascribed to a synergistic contribution from the fluorophore and ZnO. The use of a PEG spacer saw a further increase in intensity, again due to the combinatory effect of fluorescence emission from the semiconductor and fluorophore. Interestingly an additional emission was seen at 360 nm in the spectra of FZ-S-DnS50 and FZ-S-PEG-DnS50. Initially the extra emission was believed to be a product of Raman scattering, however, variation of the excitation wavelength to 10 nm either side of the original 277 nm excitation wavelength did not result in a corresponding 10 nm shift of the 360 nm emission signal as would be expected from a signal caused by Raman scattering. It was then postulated that there may be a possible electron transition occurring at the interface of the ZnO and Fe₃O₄ crystallites that form the bulk of the core NP, however, the signal was not present in the spectra of FZ and FZ-S NPs. To eliminate, possible artefacts due to solvent impurities the samples were reprepared in fresh solvent and the fluorescence emission retested, however the signal at 360 nm persisted in the spectra of FZ-S-DnS50 and FZ-S-PEG-DnS50. As such, it was hypothesised that an additional excited state of ZnO may have formed due to the complex nature of the composite nanostructure, however additional investigation would be required to confidently assign the emission.

The fluorescent properties of FZ-S-PEG-DnS NPs were further demonstrated via fluorescence microscopy, where dilute suspensions (25 and 100 $\mu\text{g}\cdot\text{mL}^{-1}$) of the PS were drop cast on to glass slides for imaging. A 100 $\mu\text{g}\cdot\text{mL}^{-1}$ sample of FZ-S-PEG was used as a control. As shown in Figure 4-7, several green spots of NP fluorescence can be observed (Figure 4-7a and b), indicating the presence of dansyl terminated PEGylated NPs on the surface of the glass slide; inconsistency in the brightness and size of spots was attributed to aggregation. In contrast, the absence of the dansyl moiety on the control NPs is clearly illustrated by the lack of fluorescent green spots observed in Figure 4-7c. The use of FZ-S-PEG-DnS as a fluorescent marker in cell culture is currently under investigation.

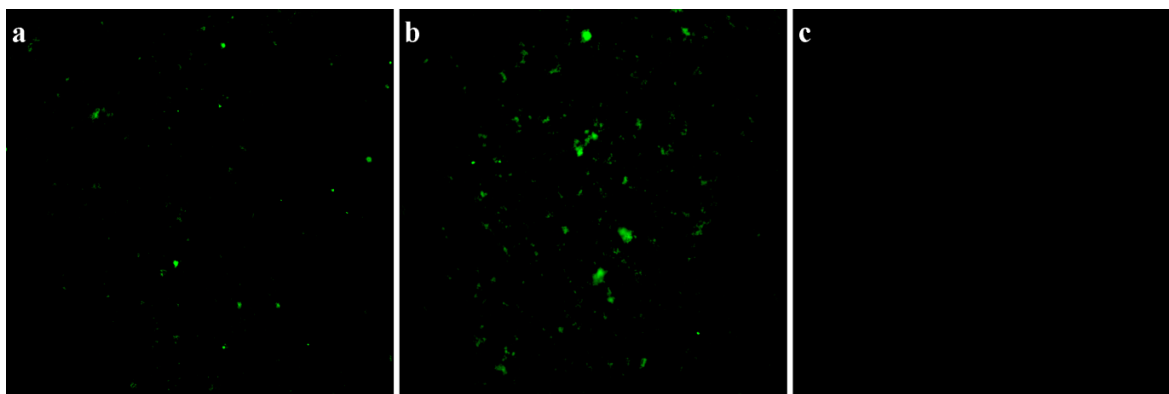


Figure 4-7. Fluorescence micrographs of FZ-S-PEG-DnS NPs at (a) $25 \mu\text{g.mL}^{-1}$ and (b) $100 \mu\text{g.mL}^{-1}$. With (c) FZ-S-PEG at $100 \mu\text{g.mL}^{-1}$. A magnification of 240x was used for all images.

4.3.2 Adsorption and photodegradation of MB

Adsorption and Photodegradation experiments were carried out using a well-established method based on previously published work [2, 3]. As such, testing was not carried out in replicate, however several trial experiments were run to establish the reproducibility and reliability of the method; supporting results are presented in Appendix 1. The percentage adsorption and photodegradation of MB through use of FZ, FZ-S, and FZ-S-PEG25 and FZ-S-PEG50 is displayed in Figure 4-8 with corresponding zeta potential measurements also displayed. MB adsorption (Figure 4-8a), evaluated in the dark from $t = 0$ min to $t = 90$ min, was facilitated via electrostatic attraction between the negatively charged PS surfaces and positively charged MB [38], and was observed to be instantaneous, as seen previously in Chapter 3. Adsorption was maximised on FZ-S NPs due to the accumulation of surface hydroxyl groups promoting electronegativity (Figure 4-8a). Charge induced adsorption of MB with silica NPs has been reported previously [39]. As pH was reduced from 9.3 to 4.0, protonation caused a decrease in the magnitude of the electronegative double layer and corresponded to a reduction in MB adsorption. Adsorption of MB to FZ core NPs was negligible ($< 1.5\%$) over the studied pH range (Figure 4-8a). MB adsorption was observed to vary inversely with PEG content across the entire pH range. Increasing the PEG content had a neutralising effect on PS surface charge, explaining the observed decrease in adsorption; charge neutralisation through PEG conjugation has been reported elsewhere [15]. Conjugation of FA onto FZ-S-PEG25 and FZ-S-PEG50 had no discernible change on MB adsorption and thus FZ-S-PEG-FA25 and FZ-S-PEG-FA50 have not been include in Figure 4-8a.

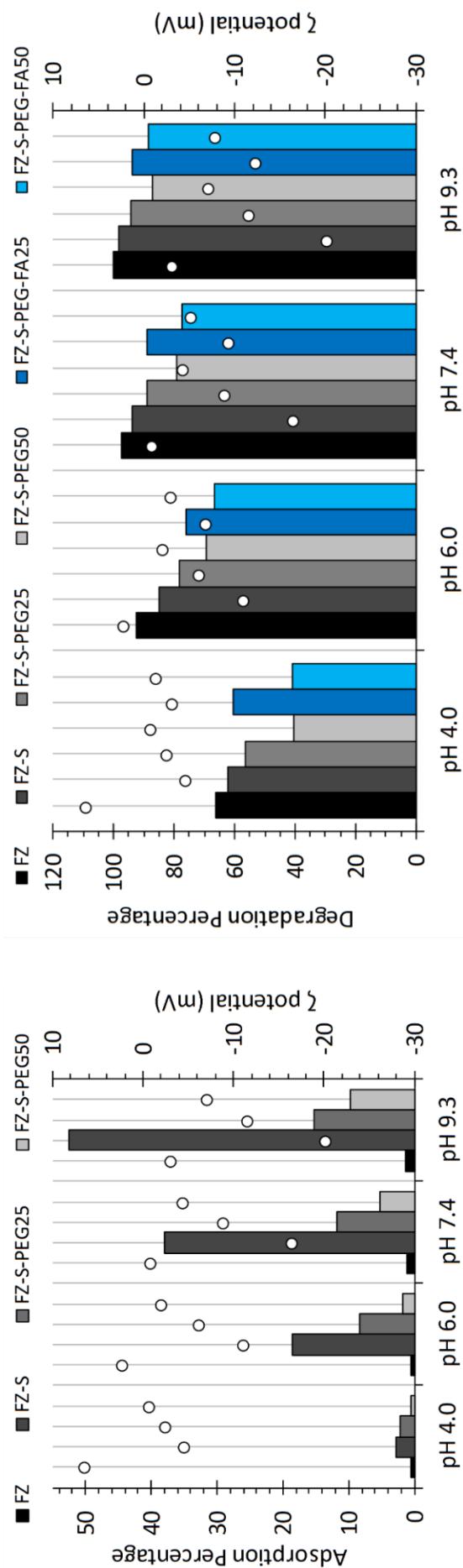


Figure 4-8. Effect of PEG on adsorption (a) and photodegradation (b) of MB. Open circles designate the zeta potential of the corresponding samples, at the given pH, in the absence of MB.

The percentage degradation of MB after exposure to 150 min of UV radiation using FZ, FZ-S, FZ-S-PEG25, FZ-S-PEG50, FZ-S-PEG-FA25 and FZ-S-PEG-FA50 is displayed in Figure 4-8b. Photodegradation was maximised at high pH and this trend was obvious through use of all photocatalysts and correlated well with observations in Chapter 3. The reduction in photocatalytic performance at lower pH was attributed to corrosion of the catalytic ZnO component, where the corroded zinc content for the FZ reaction solution was measured to be 256 mg.L^{-1} at pH 4 via ICP-OES. MB degradation efficiency and stability of the catalyst dispersions was maximised at pH 9.3 due to elevated particle surface charge and minimal corrosion (1.4 and 0.003 mg.L^{-1} zinc and iron respectively for FZ NP reaction solution), resulting in increased inter-particle repulsion and maximised PS surface area. The efficiency of MB photodegradation generally decreased with increasing degree of surface modification ($\text{FZ} > \text{FZ-S} > \text{FZ-S-PEG25} > \text{FZ-S-PEG50}$) irrespective of reaction pH, with no significant difference in photo degradation between FZ-S-PEG25 and FZ-S-PEG-FA25 and FZ-S-PEG50 and FZ-S-PEG-FA50. In Chapter 3 and in our previous work with TiO_2 and phenol, silanisation was shown to shield the FZ core from irradiation and act as a barrier, preventing the migration of reactive radical species to the surface of the PS mitigating oxidation of MB [25]. Addition of bulky PEG molecules to the surface of FZ-S seemed to augment this shielding effect as observed by the reduction in MB photodegradation upon PEGylation and the further decrease upon increasing the PEG content. Subsequent attachment of FA had little impact on the degradation efficiency.

MB photodegradation percentage using FZ, FZ-S, FZ-S-DnS50, FZ-S-PEG50 and FZ-S-PEG-DnS50 is displayed in Figure 4-9b. Similar trends were seen as before with degradation being maximised at higher pH. FZ-S-DnS50 outperformed its PEGylated counterpart at all pH trials due to the shielding effect of the PEG spacer. Degradation afforded by FZ-S was greater than that of FZ-S-DnS50, possibly due to steric hindrance afforded by the fluorophore molecules, as seen with FA in Chapter 3.

To confirm the prevalence of photocorrosion, aliquots of reaction solutions were subject to ICP-OES analysis for zinc and iron content at predetermined time points of the adsorption and degradation studies. Quantification of zinc and iron was carried out for reaction solutions of pH 9.3 to avoid the influence of chemical corrosion. Quantification data are represented graphically in Figure 4-10 below. The increase in zinc and iron content after $t = 90$ min was attributed to photo-corrosion of the hybrid NPs, whereby interactions between photo-induced holes and the metal oxides yielded water soluble Zn^{2+} and $\text{Fe}^{2+}/\text{Fe}^{3+}$

ions. Furthermore, surface modification with silica was found to reduce the degree of photocorrosion through the formation of a physical barrier. This effect was compounded upon PEGylation and more so upon increasing the PEG content. PEGylation may further assist compatibility of the synthesised PSs with biological environments by curbing metal associated toxicity.

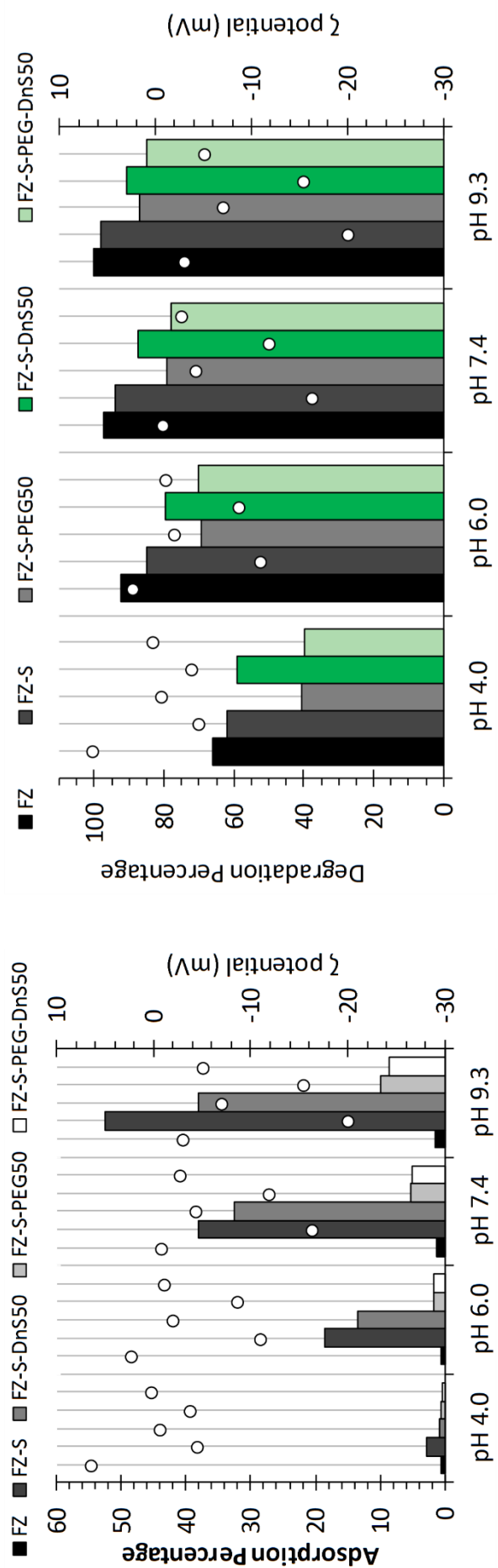


Figure 4-9. Effect of dansylation on adsorption (a) and photodegradation (b) of MB. Open circles designate the zeta potential of the corresponding samples, at the given pH, in the absence of MB.

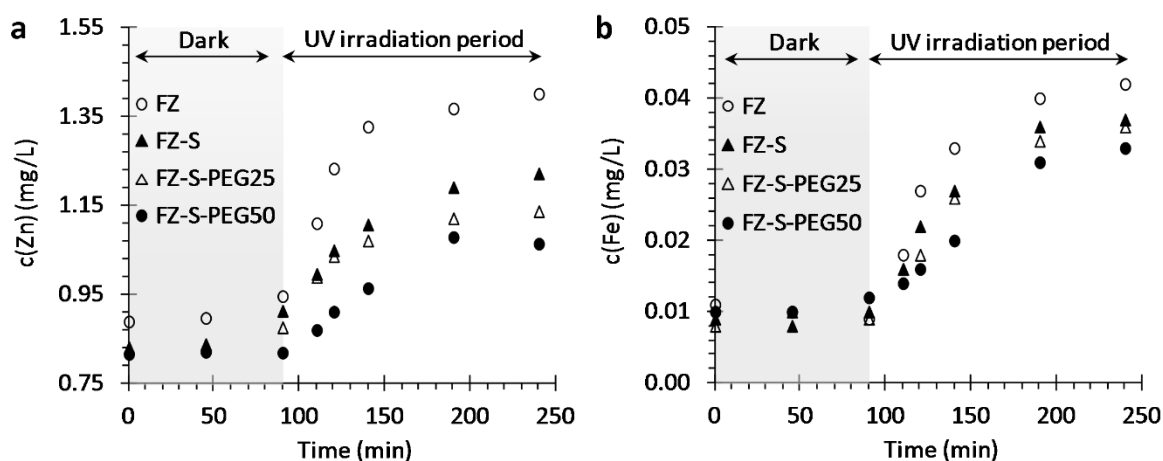


Figure 4-10. ICP-OES analysis of (a) zinc content and (b) iron content at pH 9.3 over the adsorption (dark) and photodegradation periods.

4.4 Conclusion

The surface modification of hybrid iron oxide/ zinc oxide nanoparticles with a silica shell and PEG was successfully carried out to produce the novel core shell PEGylated photosensitisers FZ-S-PEG25 and FZ-S-PEG50. Subsequent chemical modification allowed conjugation of a folic acid targeting ligand to produce FZ-S-PEG-FA25 and FZ-S-PEG-FA50. The flexibility of this synthetic scheme was highlighted through attachment of a dansyl fluorophore either with a PEG spacer or directly to the silanised core-shell particles to form novel fluorescent labelled PSs FS-S-PEG-DnS50 and FZ-S-DnS50 respectively. Adsorption and photodegradation studies using methylene blue showed that surface modification with either PEG or the fluorophore did not compromise the photocatalytic properties of the hybrid core. Furthermore, metal dissolution was found to be curbed by the presence of PEG, possibly lowering metal associated toxicity. Estimates of PEG surface coverage revealed a possible dense brush conformation of the surface bound polymer and indicated a potential for resistance to protein adsorption and macrophage elimination. Fluorescence microscopy revealed a green fluorescent emission from the dansylated NPs, suggesting a potential for cellular imaging. An in vitro cell toxicity study revealed that PEGylation mitigated the toxic response of NPs towards a Caco-2 cell line (to be published in a separate paper). Future in vivo work shall provide a foundation to pave the way for the clinical application of these heterogeneous semiconductor photosensitisers in photodynamic therapy.

4.5 References

- [1] S.S. Lucky, K.C. Soo, Y. Zhang, Nanoparticles in Photodynamic Therapy, *Chemical Reviews* 115(4) (2015) 1990-2042.
- [2] X. Feng, X. Lou, The effect of surfactants-bound magnetite (Fe₃O₄) on the photocatalytic properties of the heterogeneous magnetic zinc oxides nanoparticles, *Separation and Purification Technology* 147(0) (2015) 266-275.
- [3] X. Feng, S. Zhang, H. Wu, X. Lou, A novel folic acid-conjugated TiO₂-SiO₂ photosensitizer for cancer targeting in photodynamic therapy, *Colloids and Surfaces B: Biointerfaces* 125(0) (2015) 197-205.
- [4] A.L. Klibanov, K. Maruyama, V.P. Torchilin, L. Huang, Amphipathic polyethyleneglycols effectively prolong the circulation time of liposomes, *FEBS Letters* 268(1) (1990) 235-237.
- [5] J.S. Tan, D.E. Butterfield, C.L. Voycheck, K.D. Caldwell, J.T. Li, Surface modification of nanoparticles by PEO/PPO block copolymers to minimize interactions with blood components and prolong blood circulation in rats, *Biomaterials* 14(11) (1993) 823-833.
- [6] R. Gref, Y. Minamitake, M. Peracchia, V. Trubetskoy, V. Torchilin, R. Langer, Biodegradable long-circulating polymeric nanospheres, *Science* 263(5153) (1994) 1600-1603.
- [7] C.D. Walkey, J.B. Olsen, H. Guo, A. Emili, W.C.W. Chan, Nanoparticle Size and Surface Chemistry Determine Serum Protein Adsorption and Macrophage Uptake, *Journal of the American Chemical Society* 134(4) (2012) 2139-2147.
- [8] A.J. Pertsin, M. Grunze, Computer Simulation of Water near the Surface of Oligo(ethylene glycol)-Terminated Alkanethiol Self-Assembled Monolayers, *Langmuir* 16(23) (2000) 8829-8841.
- [9] K.F. Pirollo, E.H. Chang, Does a targeting ligand influence nanoparticle tumor localization or uptake?, *Trends in Biotechnology* 26(10) (2008) 552-558.
- [10] B. Pelaz, P. del Pino, P. Maffre, R. Hartmann, M. Gallego, S. Rivera-Fernández, J.M. de la Fuente, G.U. Nienhaus, W.J. Parak, Surface Functionalization of Nanoparticles with Polyethylene Glycol: Effects on Protein Adsorption and Cellular Uptake, *ACS Nano* 9(7) (2015) 6996-7008.
- [11] L. Treuel, S. Brandholt, P. Maffre, S. Wiegele, L. Shang, G.U. Nienhaus, Impact of Protein Modification on the Protein Corona on Nanoparticles and Nanoparticle-Cell Interactions, *ACS Nano* 8(1) (2014) 503-513.
- [12] Q. He, J. Zhang, J. Shi, Z. Zhu, L. Zhang, W. Bu, L. Guo, Y. Chen, The effect of PEGylation of mesoporous silica nanoparticles on nonspecific binding of serum proteins and cellular responses, *Biomaterials* 31(6) (2010) 1085-1092.
- [13] N. Backmann, N. Kappeler, T. Braun, F. Huber, H.-P. Lang, C. Gerber, R.Y.H. Lim, Sensing surface PEGylation with microcantilevers, *Beilstein Journal of Nanotechnology* 1 (2010) 3-13.
- [14] J.L. Perry, K.G. Reuter, M.P. Kai, K.P. Herlihy, S.W. Jones, J.C. Luft, M. Napier, J.E. Bear, J.M. DeSimone, PEGylated PRINT Nanoparticles: The Impact of PEG Density on Protein Binding, Macrophage Association, Biodistribution, and Pharmacokinetics, *Nano Letters* 12(10) (2012) 5304-5310.
- [15] Q. Yang, S.W. Jones, C.L. Parker, W.C. Zamboni, J.E. Bear, S.K. Lai, Evading Immune Cell Uptake and Clearance Requires PEG Grafting at Densities Substantially Exceeding the Minimum for Brush Conformation, *Molecular Pharmaceutics* 11(4) (2014) 1250-1258.
- [16] Q. Dai, C. Walkey, W.C.W. Chan, Polyethylene Glycol Backfilling Mitigates the Negative Impact of the Protein Corona on Nanoparticle Cell Targeting, *Angewandte Chemie International Edition* 53(20) (2014) 5093-5096.
- [17] D.W. Bartlett, H. Su, I.J. Hildebrandt, W.A. Weber, M.E. Davis, Impact of tumor-specific targeting on the biodistribution and efficacy of siRNA nanoparticles measured by multimodality in vivo imaging, *Proceedings of the National Academy of Sciences of the United States of America* 104(39) (2007) 15549-15554.
- [18] D.B. Kirpotin, D.C. Drummond, Y. Shao, M.R. Shalaby, K. Hong, U.B. Nielsen, J.D. Marks, C.C. Benz, J.W. Park, Antibody Targeting of Long-Circulating Lipidic Nanoparticles Does Not Increase Tumor Localization but Does Increase Internalization in Animal Models, *Cancer Research* 66(13) (2006) 6732-6740.

- [19] X. Feng, H. Guo, K. Patel, H. Zhou, X. Lou, High performance, recoverable Fe₃O₄ZnO nanoparticles for enhanced photocatalytic degradation of phenol, *Chemical Engineering Journal* 244(0) (2014) 327-334.
- [20] S. Naahidi, M. Jafari, F. Edalat, K. Raymond, A. Khademhosseini, P. Chen, Biocompatibility of engineered nanoparticles for drug delivery, *Journal of Controlled Release* 166(2) (2013) 182-194.
- [21] A. Giuffrida, G. Maccarrone, V. Cucinotta, S. Orlandini, A. Contino, Recent advances in chiral separation of amino acids using capillary electromigration techniques, *Journal of Chromatography A* 1363 (2014) 41-50.
- [22] L.C. Kenmogne, R. Maltais, D. Poirier, Synthesis of a dansyl-labeled inhibitor of 17 β -hydroxysteroid dehydrogenase type 3 for optical imaging, *Bioorganic & Medicinal Chemistry Letters* 26(9) (2016) 2179-2183.
- [23] G. Liu, H. Wu, H. Zheng, L. Tang, H. Hu, H. Yang, S. Yang, Synthesis and applications of fluorescent-magnetic-bifunctional dansylated Fe₃O₄@SiO₂ nanoparticles, *Journal of Materials Science* 46(18) (2011) 5959-5968.
- [24] G. Pourfallah, X. Lou, A novel recyclable magnetic nanostructure for highly sensitive, selective and reversible detection of zinc ions in aqueous solutions, *Sensors and Actuators B: Chemical* 233 (2016) 379-387.
- [25] X. Feng, S. Zhang, X. Lou, Controlling silica coating thickness on TiO₂ nanoparticles for effective photodynamic therapy, *Colloids and Surfaces B: Biointerfaces* 107(0) (2013) 220-226.
- [26] R.J. Lee, P.S. Low, Delivery of liposomes into cultured KB cells via folate receptor-mediated endocytosis, *Journal of Biological Chemistry* 269(5) (1994) 3198-3204.
- [27] K. Patel, B. Sundara Raj, Y. Chen, X. Lou, Cytotoxicity of folic acid conjugated hollow silica nanoparticles toward Caco2 and 3T3 cells, with and without encapsulated DOX, *Colloids and Surfaces B: Biointerfaces* 140 (2016) 213-222.
- [28] M. Ramani, S. Ponnusamy, C. Muthamizhchelvan, J. Cullen, S. Krishnamurthy, E. Marsili, Morphology-directed synthesis of ZnO nanostructures and their antibacterial activity, *Colloids and Surfaces B: Biointerfaces* 105(0) (2013) 24-30.
- [29] G. Xiong, U. Pal, J.G. Serrano, K.B. Ucer, R.T. Williams, Photoluminescence and FTIR study of ZnO nanoparticles: the impurity and defect perspective, *physica status solidi (c)* 3(10) (2006) 3577-3581.
- [30] P. Huang, L. Bao, C. Zhang, J. Lin, T. Luo, D. Yang, M. He, Z. Li, G. Gao, B. Gao, S. Fu, D. Cui, Folic acid-conjugated Silica-modified gold nanorods for X-ray/CT imaging-guided dual-mode radiation and photo-thermal therapy, *Biomaterials* 32(36) (2011) 9796-9809.
- [31] V.L. Furer, I.I. Vandyukova, A.E. Vandyukov, S. Fuchs, J.P. Majoral, A.M. Caminade, V.I. Kovalenko, Vibrational spectra study of fluorescent dendrimers built from the cyclotriphosphazene core with terminal dansyl and carbamate groups, *Spectrochimica Acta Part A: Molecular and Biomolecular Spectroscopy* 79(3) (2011) 462-470.
- [32] Q. Yuan, S. Hein, R.D.K. Misra, New generation of chitosan-encapsulated ZnO quantum dots loaded with drug: Synthesis, characterization and in vitro drug delivery response, *Acta Biomaterialia* 6(7) (2010) 2732-2739.
- [33] S.K. Sahu, S.K. Mallick, S. Santra, T.K. Maiti, S.K. Ghosh, P. Pramanik, In vitro evaluation of folic acid modified carboxymethyl chitosan nanoparticles loaded with doxorubicin for targeted delivery, *Journal of Materials Science : Materials in Medicine* 21(5) (2010) 1587-1597.
- [34] M. Montalti, L. Prodi, N. Zaccheroni, G. Battistini, S. Marcuz, F. Mancin, E. Rampazzo, U. Tonellato, Size Effect on the Fluorescence Properties of Dansyl-Doped Silica Nanoparticles, *Langmuir* 22(13) (2006) 5877-5881.
- [35] B.P. Joshi, C.R. Lohani, K.-H. Lee, A highly sensitive and selective detection of Hg(II) in 100% aqueous solution with fluorescent labeled dimerized Cys residues, *Organic & Biomolecular Chemistry* 8(14) (2010) 3220-3226.
- [36] V. Tharmaraj, K. Pitchumani, An acyclic, dansyl based colorimetric and fluorescent chemosensor for Hg(II) via twisted intramolecular charge transfer (TICT), *Analytica Chimica Acta* 751 (2012) 171-175.
- [37] H. Maeda, T. Maeda, K. Mizuno, Absorption and Fluorescence Spectroscopic Properties of 1- and 1,4-Silyl-Substituted Naphthalene Derivatives, *Molecules* 17(5) (2012) 5108.

- [38] N.N. Nassar, A. Ringsred, Rapid Adsorption of Methylene Blue from Aqueous Solutions by Goethite Nanoadsorbents, *Environmental Engineering Science* 29(8) (2012) 790-797.
- [39] T.-S. Ding, X.-C. Huang, Y.-L. Luo, H.-Y. Hsu, In vitro investigation of methylene blue-bearing, electrostatically assembled aptamer–silica nanocomposites as potential photodynamic therapeutics, *Colloids and Surfaces B: Biointerfaces* 135 (2015) 217-224.

CHAPTER 5

5 Conclusions and future considerations

The methods, techniques and results presented in this dissertation are of significant value to practitioners of experimental cancer therapeutics because they not only contribute to current knowledge pertaining to nanoparticle (NP) design and synthesis for theragnostic applications, but they also provide a novel, yet facile surface modification scheme that allows a transition of NP systems intended for photocatalytic based applications, to use in biological settings as potential cancer therapeutics. The multifarious nature of cancer is impetus alone for the application of rigorous exploration and adaptation to developing and established therapies, and so it seems only logical that future work be carried out on the systems developed and studied in this thesis.

Cytotoxicity investigations utilising hollow silica shells provided new insights into cell specific toxic responses. The hollow silica shells not only showed cytotoxicity specific to a malignant cell line, they did so in the absence of the attached folic acid (FA) cell targeting ligand. This finding merits further investigation to elucidate the mechanisms driving cell specific toxic responses. Furthermore, research should be carried out to determine whether the developed silica shells show toxic avidity towards other malignant cell lines over non-malignant counterparts. While conjugation with the folate ligand did enhance cancer cell specificity, it also proved to increase the viability of both the malignant and non-malignant cell lines. Although there are a few investigations detailing the optimal FA ligand

density for cellular uptake [1, 2], the effect of the FA ligand density on cell viability has not been openly discussed in the prevailing research. As such, further stipulations on folate content must be provisioned when designing such systems. Future studies with this hollow silica shell material may pave the way for designing a single NP system able to impart specificity towards multiple cancer cell types. Application of the silica coating on to an established iron oxide-zinc oxide photocatalyst ($\text{Fe}_3\text{O}_4\text{-ZnO}$) demonstrated a decline in the photophysical properties of the core structure. However, the novel core-shell system was also proven to be more effective than its pure zinc oxide (ZnO). More importantly, this research has demonstrated that the hybrid core-shell nanoparticles have a great potential in applications geared towards photodynamic therapy (PDT). The FA conjugated core-shell system demonstrated a significant photokilling effect with a drastic reduction in the viability of human epithelial colorectal adenocarcinoma (Caco-2) cells. While concerning toxicity at larger doses and longer incubation periods was observed, it was postulated that this toxicity stemmed from metal dissolution of the core – a property that could be mitigated with design adaptations. An investigation confirming the processes behind this toxicity and understanding and controlling the dissolution kinetics would assist in the design of photosensitisers that are compatible with cell lines in the absence of radiation – a key requirement for PDT.

Further modification of the silica coated $\text{Fe}_3\text{O}_4\text{-ZnO}$ core-shell system with polyethylene glycol (PEG) and a dansyl fluorophore was carried out in order to impart multimodality in the way of potential stealth and imaging properties. Physicochemical characterisation confirmed and highlighted the flexibility and facile nature of the synthetic route employed. Furthermore, the photophysical properties of the surface modified core-shell systems were shown to remain highly efficient and PEGylation was found to mitigate the effect of NP associated cell toxicity in vitro towards a Caco-2 cell line. Additional work can be carried out to assess the impact of PEGylation and dansylation in in vivo biological settings. The photo-killing effect of the surface modified NP should also be investigated to prove the proposed concept, hence forming a continuous topic of research in this group. Finally, studying and applying the magnetic properties of iron oxide within the core towards magnetic resonance imaging and tumour targeting via external magnetic fields would further extend the multifaceted nature of this NP system.

5.1 References

- [1] Z. Tang, D. Li, H. Sun, X. Guo, Y. Chen, S. Zhou, Quantitative control of active targeting of nanocarriers to tumor cells through optimization of folate ligand density, *Biomaterials* 35(27) (2014) 8015-8027.
- [2] E. Moradi, D. Vllasaliu, M. Garnett, F. Falcone, S. Stolnik, Ligand density and clustering effects on endocytosis of folate modified nanoparticles, *RSC Advances* 2(7) (2012) 3025-3033.

BIBLIOGRAPHY

A

- Akhundi, A., & Habibi-Yangjeh, A. (2015). Novel magnetically separable g-C₃N₄/AgBr/Fe₃O₄ nanocomposites as visible-light-driven photocatalysts with highly enhanced activities. *Ceramics International*, *41*(4), 5634-5643. doi: <http://dx.doi.org/10.1016/j.ceramint.2014.12.145>
- Alexander, C. M., Hamner, K. L., Maye, M. M., & Dabrowiak, J. C. (2014). Multifunctional DNA-Gold Nanoparticles for Targeted Doxorubicin Delivery. *Bioconjugate Chemistry*, *25*(7), 1261-1271. doi: 10.1021/bc500136r
- Allison, R. R. (2014). Photodynamic therapy: oncologic horizons. *Future Oncology*, *10*(1), 123-124. doi: <http://dx.doi.org/10.2217/fon.13.176>
- Amantea, M. A., Forrest, A., Northfelt, D. W., & Mamelok, R. (1997). Population pharmacokinetics and pharmacodynamics of pegylated-liposomal doxorubicin in patients with AIDS-related Kaposi's sarcoma. *Clinical Pharmacology & Therapeutics*, *61*(3), 301-311. doi: 10.1016/s0009-9236(97)90162-4
- Anderle, P., Niederer, E., Rubas, W., Hilgendorf, C., Spahn-Langguth, H., Wunderli-Allenspach, H., . . . Langguth, P. (1998). P-glycoprotein (P-gp) mediated efflux in Caco-2 cell monolayers: The influence of culturing conditions and drug exposure on P-gp expression levels. *Journal of Pharmaceutical Sciences*, *87*(6), 757-762. doi: 10.1021/js970372e

B

- Baban, D. F., & Seymour, L. W. (1998). Control of tumour vascular permeability. *Advanced Drug Delivery Reviews*, *34*(1), 109-119. doi: [http://dx.doi.org/10.1016/S0169-409X\(98\)00003-9](http://dx.doi.org/10.1016/S0169-409X(98)00003-9)

- Backmann, N., Kappeler, N., Braun, T., Huber, F., Lang, H.-P., Gerber, C., & Lim, R. Y. H. (2010). Sensing surface PEGylation with microcantilevers. *Beilstein Journal of Nanotechnology*, 1, 3-13. doi: 10.3762/bjnano.1.2
- Baeza, A. (2014). Ceramic Nanoparticles for Cancer Treatment *Bio-Ceramics with Clinical Applications* (pp. 421-455): John Wiley & Sons, Ltd.
- Ballarini, F., Altieri, S., Bortolussi, S., Giroletti, E., & Protti, N. (2013). A Model of Radiation-Induced Cell Killing: Insights into Mechanisms and Applications for Hadron Therapy. *Radiation Research*, 180(3), 307-315
- Barenholz, Y. (2012). Doxil® — The first FDA-approved nano-drug: Lessons learned. *Journal of Controlled Release*, 160(2), 117-134. doi: <http://dx.doi.org/10.1016/j.jconrel.2012.03.020>
- Bartlett, D. W., Su, H., Hildebrandt, I. J., Weber, W. A., & Davis, M. E. (2007). Impact of tumor-specific targeting on the biodistribution and efficacy of siRNA nanoparticles measured by multimodality in vivo imaging. *Proceedings of the National Academy of Sciences of the United States of America*, 104(39), 15549-15554. doi: 10.1073/pnas.0707461104
- Bazak, R., Hourri, M., El Achy, S., Kamel, S., & Refaat, T. (2015). Cancer active targeting by nanoparticles: a comprehensive review of literature. *Journal of Cancer Research and Clinical Oncology*, 141(5), 769-784. doi: 10.1007/s00432-014-1767-3
- Benezra, M., Penate-Medina, O., Zanzonico, P. B., Schaer, D., Ow, H., Burns, A., . . . Bradbury, M. S. (2011). Multimodal silica nanoparticles are effective cancer-targeted probes in a model of human melanoma. *The Journal of Clinical Investigation*, 121(7), 2768-2780. doi: 10.1172/jci45600
- Bertrand, N., Wu, J., Xu, X., Kamaly, N., & Farokhzad, O. C. (2014). Cancer nanotechnology: The impact of passive and active targeting in the era of modern cancer biology. *Advanced Drug Delivery Reviews*, 66, 2-25. doi: <http://dx.doi.org/10.1016/j.addr.2013.11.009>
- Bonechi, C., Donati, A., Lampariello, R., Martini, S., Picchi, M. P., Ricci, M., & Rossi, C. (2004). Solution structure of folic acid: Molecular mechanics and NMR investigation. *Spectrochimica Acta Part A: Molecular and Biomolecular Spectroscopy*, 60(7), 1411-1419. doi: <http://dx.doi.org/10.1016/j.saa.2003.08.007>
- Bottero, F., Tomassetti, A., Canevari, S., Miotti, S., Ménard, S., & Colnaghi, M. I. (1993). Gene Transfection and Expression of the Ovarian Carcinoma Marker Folate Binding Protein on NIH/3T3 Cells Increases Cell Growth in Vitro and in Vivo. *Cancer Research*, 53(23), 5791-5796
- Brigger, I., Dubernet, C., & Couvreur, P. (2012). Nanoparticles in cancer therapy and diagnosis. *Advanced Drug Delivery Reviews*, 64, Supplement(0), 24-36. doi: <http://dx.doi.org/10.1016/j.addr.2012.09.006>

Burns, A. A., Vider, J., Ow, H., Herz, E., Penate-Medina, O., Baumgart, M., . . . Bradbury, M. (2009). Fluorescent Silica Nanoparticles with Efficient Urinary Excretion for Nanomedicine. *Nano Letters*, *9*(1), 442-448. doi: 10.1021/nl803405h

Byrne, J. D., Betancourt, T., & Brannon-Peppas, L. (2008). Active targeting schemes for nanoparticle systems in cancer therapeutics. *Advanced Drug Delivery Reviews*, *60*(15), 1615-1626

C

Chang, J.-S., Chang, K. L. B., Hwang, D.-F., & Kong, Z.-L. (2007). In Vitro Cytotoxicity of Silica Nanoparticles at High Concentrations Strongly Depends on the Metabolic Activity Type of the Cell Line. *Environmental Science & Technology*, *41*(6), 2064-2068. doi: 10.1021/es062347t

Chen, S., Hayakawa, S., Shirotsaki, Y., Hanagata, N., & Osaka, A. (2014). Biomedical Applications of Sol-Gel Nanocomposites. In M. Guglielmi, G. Kickelbick & A. Martucci (Eds.), *Sol-Gel Nanocomposites*. In M. A. Aegerter & M. Prassas (Series Eds.), *Advances in Sol-Gel Derived Materials and Technologies* (Vol. 3, pp. 167-190). New York: Springer New York.

Chen, Y., & Liu, L. (2012). Modern methods for delivery of drugs across the blood-brain barrier. *Advanced Drug Delivery Reviews*, *64*(7), 640-665. doi: <http://dx.doi.org/10.1016/j.addr.2011.11.010>

Cheng, L., Wang, C., Feng, L., Yang, K., & Liu, Z. (2014). Functional Nanomaterials for Phototherapies of Cancer. *Chemical Reviews*, *114*(21), 10869-10939. doi: 10.1021/cr400532z

Choi, S.-J., Oh, J.-M., & Choy, J.-H. (2009). Toxicological effects of inorganic nanoparticles on human lung cancer A549 cells. *Journal of Inorganic Biochemistry*, *103*(3), 463-471. doi: <http://dx.doi.org/10.1016/j.jinorgbio.2008.12.017>

Corrie, P. G. (2011). Cytotoxic chemotherapy: clinical aspects. *Medicine*, *39*(12), 717-722. doi: <http://dx.doi.org/10.1016/j.mpmed.2011.09.012>

D

Dai, Q., Walkey, C., & Chan, W. C. W. (2014). Polyethylene Glycol Backfilling Mitigates the Negative Impact of the Protein Corona on Nanoparticle Cell Targeting. *Angewandte Chemie International Edition*, *53*(20), 5093-5096. doi: 10.1002/anie.201309464

Dawar, S., Singh, N., Kanwar, R. K., Kennedy, R. L., Veedu, R. N., Zhou, S.-F., . . . Kanwar, J. R. (2013). Multifunctional and multitargeted nanoparticles for drug delivery to overcome barriers of drug resistance in human cancers. *Drug Discovery Today*, *18*(23-24), 1292-1300. doi: <http://dx.doi.org/10.1016/j.drudis.2013.09.009>

- De Jong, W. H., Hagens, W. I., Krystek, P., Burger, M. C., Sips, A. J. A. M., & Geertsma, R. E. (2008). Particle size-dependent organ distribution of gold nanoparticles after intravenous administration. *Biomaterials*, *29*(12), 1912-1919. doi: <http://dx.doi.org/10.1016/j.biomaterials.2007.12.037>
- Deatsch, A. E., & Evans, B. A. (2014). Heating efficiency in magnetic nanoparticle hyperthermia. *Journal of Magnetism and Magnetic Materials*, *354*, 163-172. doi: <http://dx.doi.org/10.1016/j.jmmm.2013.11.006>
- Díaz-Jimenez, J. P., & Mezalek, R. T. (2013). Photodynamic Therapy for Early and Advanced Lung Cancer. In P. J. Díaz-Jimenez & N. A. Rodriguez (Eds.), *Interventions in Pulmonary Medicine* (pp. 147-163). New York, NY: Springer New York.
- Ding, H.-m., & Ma, Y.-q. (2012). Role of physicochemical properties of coating ligands in receptor-mediated endocytosis of nanoparticles. *Biomaterials*, *33*(23), 5798-5802. doi: <http://dx.doi.org/10.1016/j.biomaterials.2012.04.055>
- Ding, T.-S., Huang, X.-C., Luo, Y.-L., & Hsu, H.-Y. (2015). In vitro investigation of methylene blue-bearing, electrostatically assembled aptamer-silica nanocomposites as potential photodynamic therapeutics. *Colloids and Surfaces B: Biointerfaces*, *135*, 217-224. doi: <http://dx.doi.org/10.1016/j.colsurfb.2015.07.064>
- Dordi, B., Schönherr, H., & Vancso, G. J. (2003). Reactivity in the Confinement of Self-Assembled Monolayers: Chain Length Effects on the Hydrolysis of N-Hydroxysuccinimide Ester Disulfides on Gold. *Langmuir*, *19*(14), 5780-5786. doi: 10.1021/la0343066
- Dougherty, T. J., Grindey, G. B., Fiel, R., Weishaupt, K. R., & Boyle, D. G. (1975). Photoradiation Therapy. II. Cure of Animal Tumors With Hematoporphyrin and Light. *Journal of the National Cancer Institute*, *55*(1), 115-121. doi: 10.1093/jnci/55.1.115

F

- Feng, X., Guo, H., Patel, K., Zhou, H., & Lou, X. (2014). High performance, recoverable Fe₃O₄-ZnO nanoparticles for enhanced photocatalytic degradation of phenol. *Chemical Engineering Journal*, *244*(0), 327-334. doi: <http://dx.doi.org/10.1016/j.cej.2014.01.075>
- Feng, X., & Lou, X. (2015). The effect of surfactants-bound magnetite (Fe₃O₄) on the photocatalytic properties of the heterogeneous magnetic zinc oxides nanoparticles. *Separation and Purification Technology*, *147*(0), 266-275. doi: <http://dx.doi.org/10.1016/j.seppur.2015.04.036>
- Feng, X., Zhang, S., & Lou, X. (2013). Controlling silica coating thickness on TiO₂ nanoparticles for effective photodynamic therapy. *Colloids and Surfaces B:*

Biointerfaces, 107(0), 220-226. doi:
<http://dx.doi.org/10.1016/j.colsurfb.2013.02.007>

Feng, X., Zhang, S., Wu, H., Lou, X. (2015). A novel folic acid-conjugated TiO₂-SiO₂ photosensitizer for cancer targeting in photodynamic therapy, *Colloids and Surfaces B: Biointerfaces*, 125(0), 197-205. doi:
<https://doi.org/10.1016/j.colsurfb.2014.11.035>

Ferlay, J., Soerjomataram, I., Ervik, M., Dikshit, R., Eser, S., Mathers, C., . . . Bray, F. (2013). GLOBOCAN 2012 v1.0, Cancer Incidence and Mortality Worldwide: IARC CancerBase No. 11. from GLOBOCAN 2012 v1.0, Cancer Incidence and Mortality Worldwide: IARC CancerBase No. 11, International Agency for Research on Cancer (IARC) <http://globocan.iarc.fr>.

Friedrich, J., Eder, W., Castaneda, J., Doss, M., Huber, E., Ebner, R., & Kunz-Schughart, L. A. (2007). A Reliable Tool to Determine Cell Viability in Complex 3-D Culture: The Acid Phosphatase Assay. *Journal of Biomolecular Screening*, 12(7), 925-937. doi: 10.1177/1087057107306839

Fu, J., Zhu, Y., & Zhao, Y. (2014). Controlled free radical generation against tumor cells by pH-responsive mesoporous silica nanocomposite. *Journal of Materials Chemistry B*, 2(22), 3538-3548. doi: 10.1039/C4TB00387J

Furer, V. L., Vandyukova, I. I., Vandyukov, A. E., Fuchs, S., Majoral, J. P., Caminade, A. M., & Kovalenko, V. I. (2011). Vibrational spectra study of fluorescent dendrimers built from the cyclotriphosphazene core with terminal dansyl and carbamate groups. *Spectrochimica Acta Part A: Molecular and Biomolecular Spectroscopy*, 79(3), 462-470. doi:
<http://dx.doi.org/10.1016/j.saa.2011.03.010>

G

Gabriel, J. (2008). What is Cancer? *The Biology of Cancer* (pp. 3-9): John Wiley & Sons Ltd.

Ghosh Chaudhuri, R., & Paria, S. (2012). Core/Shell Nanoparticles: Classes, Properties, Synthesis Mechanisms, Characterization, and Applications. *Chemical Reviews*, 112(4), 2373-2433. doi: 10.1021/cr100449n

Giuffrida, A., Maccarrone, G., Cucinotta, V., Orlandini, S., & Contino, A. (2014). Recent advances in chiral separation of amino acids using capillary electromigration techniques. *Journal of Chromatography A*, 1363, 41-50. doi:
<http://dx.doi.org/10.1016/j.chroma.2014.08.041>

Gonzalez, L., Lukamowicz-Rajska, M., Thomassen, L. C. J., Kirschhock, C. E. A., Leyns, L., Lison, D., . . . Kirsch-Volders, M. (2014). Co-assessment of cell cycle and micronucleus frequencies demonstrates the influence of serum on the in vitro genotoxic response to amorphous monodisperse silica nanoparticles

of varying sizes. *Nanotoxicology*, 8(8), 876-884. doi:
doi:10.3109/17435390.2013.842266

Gref, R., Minamitake, Y., Peracchia, M., Trubetsky, V., Torchilin, V., & Langer, R. (1994). Biodegradable long-circulating polymeric nanospheres. *Science*, 263(5153), 1600-1603. doi: 10.1126/science.8128245

Grobmyer, S. R., Moudgil, B. M., Kularatne, S. A., & Low, P. S. (2010). Targeting of Nanoparticles: Folate Receptor. In J. M. Walker (Ed.), *Cancer Nanotechnology* (Vol. 624, pp. 249-265): Humana Press.

H

Haavik, C., Stolen, S., Fjellvag, H., Hanfland, M., & Hausermann, D. (2000). Equation of state of magnetite and its high-pressure modification: Thermodynamics of the Fe-O system at high pressure. *American Mineralogist*, 85, 514-523

Hackenberg, S., Scherzed, A., Kessler, M., Froelich, K., Ginzkey, C., Koehler, C., . . . Kleinsasser, N. (2010). Zinc oxide nanoparticles induce photocatalytic cell death in human head and neck squamous cell carcinoma cell lines in vitro. *International Journal of Oncology*, 37(6), 1583-1590. doi: 10.3892/ijo_00000812

Hak, S., Helgesen, E., Hektoen, H. H., Huuse, E. M., Jarzyna, P. A., Mulder, W. J. M., . . . Davies, C. d. L. (2012). The Effect of Nanoparticle Polyethylene Glycol Surface Density on Ligand-Directed Tumor Targeting Studied in Vivo by Dual Modality Imaging. *ACS Nano*, 6(6), 5648-5658. doi: 10.1021/nn301630n

Hanahan, D., & Weinberg, R. A. (2000). The Hallmarks of Cancer. *Cell*, 100(1), 57-70. doi: 10.1016/s0092-8674(00)81683-9

Hanahan, D., & Weinberg, Robert A. (2011). Hallmarks of Cancer: The Next Generation. *Cell*, 144(5), 646-674. doi: <http://dx.doi.org/10.1016/j.cell.2011.02.013>

Harrington, K. J. (2008). Biology of cancer. *Medicine*, 36(1), 1-4. doi: <http://dx.doi.org/10.1016/j.mpmed.2007.10.013>

He, Q., Zhang, J., Shi, J., Zhu, Z., Zhang, L., Bu, W., . . . Chen, Y. (2010). The effect of PEGylation of mesoporous silica nanoparticles on nonspecific binding of serum proteins and cellular responses. *Biomaterials*, 31(6), 1085-1092. doi: <http://dx.doi.org/10.1016/j.biomaterials.2009.10.046>

Hobbs, S. K., Monsky, W. L., Yuan, F., Roberts, W. G., Griffith, L., Torchilin, V. P., & Jain, R. K. (1998). Regulation of transport pathways in tumor vessels: Role of tumor type and microenvironment. *Proceedings of the National Academy of Sciences*, 95(8), 4607-4612

- Hogle, W. P. (2006). The State of the Art in Radiation Therapy. *Seminars in Oncology Nursing*, 22(4), 212-220. doi: <http://dx.doi.org/10.1016/j.soncn.2006.07.004>
- Hojan, K., & Milecki, P. (2014). Opportunities for rehabilitation of patients with radiation fibrosis syndrome. *Reports of Practical Oncology & Radiotherapy*, 19(1), 1-6. doi: <http://dx.doi.org/10.1016/j.rpor.2013.07.007>
- Horn, L., & Johnson, D. H. (2010). Ephraim McDowell, the First Ovariectomy, and the Birth of Abdominal Surgery. *Journal of Clinical Oncology*, 28(7), 1262-1268. doi: 10.1200/jco.2009.25.7261
- Huang, A., & Caro, J. (2010). Shape evolution of zinc oxide from twinned disks to single spindles through solvothermal synthesis in binary solvents. *Journal of Crystal Growth*, 312(20), 2977-2982. doi: <http://dx.doi.org/10.1016/j.jcrysgro.2010.07.028>
- Huang, P., Bao, L., Zhang, C., Lin, J., Luo, T., Yang, D., . . . Cui, D. (2011). Folic acid-conjugated Silica-modified gold nanorods for X-ray/CT imaging-guided dual-mode radiation and photo-thermal therapy. *Biomaterials*, 32(36), 9796-9809. doi: 10.1016/j.biomaterials.2011.08.086

I

- Ismail, A. F. M., Ali, M. M., & Ismail, L. F. M. (2014). Photodynamic therapy mediated antiproliferative activity of some metal-doped ZnO nanoparticles in human liver adenocarcinoma HepG2 cells under UV irradiation. *Journal of Photochemistry and Photobiology B: Biology*, 138, 99-108. doi: <http://dx.doi.org/10.1016/j.jphotobiol.2014.04.006>

J

- Jain, P. K., Lee, K. S., El-Sayed, I. H., & El-Sayed, M. A. (2006). Calculated Absorption and Scattering Properties of Gold Nanoparticles of Different Size, Shape, and Composition: Applications in Biological Imaging and Biomedicine. *The Journal of Physical Chemistry B*, 110(14), 7238-7248. doi: 10.1021/jp057170o
- Jia, L., Shen, J., Li, Z., Zhang, D., Zhang, Q., Liu, G., . . . Tian, X. (2013). In vitro and in vivo evaluation of paclitaxel-loaded mesoporous silica nanoparticles with three pore sizes. *International Journal of Pharmaceutics*, 445(1-2), 12-19. doi: <http://dx.doi.org/10.1016/j.ijpharm.2013.01.058>
- Jiang, W., KimBetty, Y. S., Rutka, J. T., & ChanWarren, C. W. (2008). Nanoparticle-mediated cellular response is size-dependent. *Nat Nano*, 3(3), 145-150
- John, A. A., Subramanian, A. P., Vellayappan, M. V., Balaji, A., Jaganathan, S. K., Mohandas, H., . . . Yusof, M. (2015). Review: physico-chemical modification

as a versatile strategy for the biocompatibility enhancement of biomaterials. *RSC Advances*, 5(49), 39232-39244. doi: 10.1039/C5RA03018H

Jokerst, J. V., Lobovkina, T., Zare, R. N., & Gambhir, S. S. (2011). Nanoparticle PEGylation for imaging and therapy. *Nanomedicine (London, England)*, 6(4), 715-728. doi: 10.2217/nnm.11.19

Joshi, B. P., Lohani, C. R., & Lee, K.-H. (2010). A highly sensitive and selective detection of Hg(II) in 100% aqueous solution with fluorescent labeled dimerized Cys residues. *Organic & Biomolecular Chemistry*, 8(14), 3220-3226. doi: 10.1039/B925744F

K

Karunakaran, C., Vinayagamorthy, P., & Jayabharathi, J. (2014). Nonquenching of Charge Carriers by Fe₃O₄ Core in Fe₃O₄/ZnO Nanosheet Photocatalyst. *Langmuir*, 30(49), 15031-15039. doi: 10.1021/la5039409

Kasper, B., D'Hondt, V., Vereecken, P., & Awada, A. (2007). Novel treatment strategies for malignant melanoma: A new beginning? *Critical Reviews in Oncology/Hematology*, 62(1), 16-22. doi: <http://dx.doi.org/10.1016/j.critrevonc.2006.11.007>

Kenmogne, L. C., Maltais, R., & Poirier, D. (2016). Synthesis of a dansyl-labeled inhibitor of 17 β -hydroxysteroid dehydrogenase type 3 for optical imaging. *Bioorganic & Medicinal Chemistry Letters*, 26(9), 2179-2183. doi: <http://dx.doi.org/10.1016/j.bmcl.2016.03.069>

Kievit, F. M., Wang, F. Y., Fang, C., Mok, H., Wang, K., Silber, J. R., . . . Zhang, M. (2011). Doxorubicin loaded iron oxide nanoparticles overcome multidrug resistance in cancer in vitro. *Journal of Controlled Release*, 152(1), 76-83. doi: <http://dx.doi.org/10.1016/j.jconrel.2011.01.024>

Kim, I.-Y., Joachim, E., Choi, H., & Kim, K. (2015). Toxicity of silica nanoparticles depends on size, dose, and cell type. *Nanomedicine: Nanotechnology, Biology and Medicine*, 11(6), 1407-1416. doi: <http://dx.doi.org/10.1016/j.nano.2015.03.004>

Kirpotin, D. B., Drummond, D. C., Shao, Y., Shalaby, M. R., Hong, K., Nielsen, U. B., . . . Park, J. W. (2006). Antibody Targeting of Long-Circulating Lipidic Nanoparticles Does Not Increase Tumor Localization but Does Increase Internalization in Animal Models. *Cancer Research*, 66(13), 6732-6740. doi: 10.1158/0008-5472.can-05-4199

Kisch, H. (2013). Semiconductor Photocatalysis—Mechanistic and Synthetic Aspects. *Angewandte Chemie International Edition*, 52(3), 812-847. doi: 10.1002/anie.201201200

- Klibanov, A. L., Maruyama, K., Torchilin, V. P., & Huang, L. (1990). Amphipathic polyethyleneglycols effectively prolong the circulation time of liposomes. *FEBS Letters*, *268*(1), 235-237. doi: 10.1016/0014-5793(90)81016-H
- Knop, K., Hoogenboom, R., Fischer, D., & Schubert, U. S. (2010). Poly(ethylene glycol) in Drug Delivery: Pros and Cons as Well as Potential Alternatives. *Angewandte Chemie International Edition*, *49*(36), 6288-6308. doi: 10.1002/anie.200902672
- Kolhar, P., Anselmo, A. C., Gupta, V., Pant, K., Prabhakarandian, B., Ruoslahti, E., & Mitragotri, S. (2013). Using shape effects to target antibody-coated nanoparticles to lung and brain endothelium. *Proceedings of the National Academy of Sciences*, *110*(26), 10753-10758. doi: 10.1073/pnas.1308345110
- Korbelik, M., Zhang, W., & Merchant, S. (2011). Involvement of damage-associated molecular patterns in tumor response to photodynamic therapy: surface expression of calreticulin and high-mobility group box-1 release. *Cancer Immunology, Immunotherapy*, *60*(10), 1431-1437. doi: <http://dx.doi.org/10.3322/caac.20114>
- Kumar, S. G., & Rao, K. S. R. K. (2015). Zinc oxide based photocatalysis: tailoring surface-bulk structure and related interfacial charge carrier dynamics for better environmental applications. *RSC Advances*, *5*(5), 3306-3351. doi: 10.1039/C4RA13299H

L

- Lee, R. J., & Low, P. S. (1994). Delivery of liposomes into cultured KB cells via folate receptor-mediated endocytosis. *Journal of Biological Chemistry*, *269*(5), 3198-3204
- Lee, R. J., & Low, P. S. (1994). Delivery of liposomes into cultured KB cells via folate receptor-mediated endocytosis. *Journal of Biological Chemistry*, *269*(5), 3198-3204
- Li, J., Guo, D., Wang, X., Wang, H., Jiang, H., & Chen, B. (2010). The Photodynamic Effect of Different Size ZnO Nanoparticles on Cancer Cell Proliferation In Vitro. *Nanoscale Research Letters*, *5*(6), 1063 - 1071
- Lieberman, A., Mendez, N., Trogler, W. C., & Kummel, A. C. (2014). Synthesis and surface functionalization of silica nanoparticles for nanomedicine. *Surface Science Reports*, *69*(2-3), 132-158. doi: <http://dx.doi.org/10.1016/j.surfrep.2014.07.001>
- Lin, W., Huang, Y.-w., Zhou, X.-D., & Ma, Y. (2006). In vitro toxicity of silica nanoparticles in human lung cancer cells. *Toxicology and Applied Pharmacology*, *217*(3), 252-259. doi: <http://dx.doi.org/10.1016/j.taap.2006.10.004>

- Lin, W.-I., Lin, C.-Y., Lin, Y.-S., Wu, S.-H., Huang, Y.-R., Hung, Y., . . . Mou, C.-Y. (2013). High payload Gd(iii) encapsulated in hollow silica nanospheres for high resolution magnetic resonance imaging. *Journal of Materials Chemistry B*, 1(5), 639-645. doi: 10.1039/c2tb00283c
- Lind, M. J. (2011). Principles of cytotoxic chemotherapy. *Medicine*, 39(12), 711-716. doi: <http://dx.doi.org/10.1016/j.mpmed.2011.09.009>
- Liu, G., Wu, H., Zheng, H., Tang, L., Hu, H., Yang, H., & Yang, S. (2011). Synthesis and applications of fluorescent-magnetic-bifunctional dansylated Fe₃O₄@SiO₂ nanoparticles. *Journal of Materials Science*, 46(18), 5959-5968. doi: 10.1007/s10853-011-5551-3
- Liu, J., Zhang, W., Zhang, H., Yang, Z., Li, T., Wang, B., . . . Chen, H. (2013). A multifunctional nanoprobe based on Au-Fe₃O₄ nanoparticles for multimodal and ultrasensitive detection of cancer cells. *Chemical Communications*, 49(43), 4938-4940. doi: 10.1039/C3CC41984C
- Liu, X., Fu, F., Xu, K., Zou, R., Yang, J., Wang, Q., . . . Hu, J. (2014). Folic acid-conjugated hollow mesoporous silica/CuS nanocomposites as a difunctional nanoplatform for targeted chemo-photothermal therapy of cancer cells. *Journal of Materials Chemistry B*, 2(33), 5358-5367. doi: 10.1039/c4tb00919c
- Lu, Y., & Low, P. S. (2012). Folate-mediated delivery of macromolecular anticancer therapeutic agents. *Advanced Drug Delivery Reviews*, 64, Supplement(0), 342-352. doi: <http://dx.doi.org/10.1016/j.addr.2012.09.020>
- Lucky, S. S., Soo, K. C., & Zhang, Y. (2015). Nanoparticles in Photodynamic Therapy. *Chemical Reviews*, 115(4), 1990-2042. doi: 10.1021/cr5004198

M

- Maeda, H., Maeda, T., & Mizuno, K. (2012). Absorption and Fluorescence Spectroscopic Properties of 1- and 1,4-Silyl-Substituted Naphthalene Derivatives. *Molecules*, 17(5), 5108
- Makin, G., & Dive, C. (2001). Apoptosis and cancer chemotherapy. *Trends in Cell Biology*, 11(11), S22-S26. doi: [http://dx.doi.org/10.1016/S0962-8924\(01\)02124-9](http://dx.doi.org/10.1016/S0962-8924(01)02124-9)
- Meng, H., Mai, W. X., Zhang, H., Xue, M., Xia, T., Lin, S., . . . Nel, A. E. (2013). Codelivery of an Optimal Drug/siRNA Combination Using Mesoporous Silica Nanoparticles To Overcome Drug Resistance in Breast Cancer in Vitro and in Vivo. *ACS Nano*, 7(2), 994-1005. doi: 10.1021/nn3044066
- Meng, H., Wang, M., Liu, H., Liu, X., Situ, A., Wu, B., . . . Nel, A. E. (2015). Use of a Lipid-Coated Mesoporous Silica Nanoparticle Platform for Synergistic Gemcitabine and Paclitaxel Delivery to Human Pancreatic Cancer in Mice. *ACS Nano*, 9(4), 3540-3557. doi: 10.1021/acsnano.5b00510

- Middleton, M. R., Grob, J. J., Aaronson, N., Fierlbeck, G., Tilgen, W., Seiter, S., . . . Thatcher, N. (2000). Randomized Phase III Study of Temozolomide Versus Dacarbazine in the Treatment of Patients With Advanced Metastatic Malignant Melanoma. *Journal of Clinical Oncology*, *18*(1), 158
- Mikhaylov, G., Mikac, U., Magaeva, A. A., Itin, V. I., Naiden, E. P., Psakhye, I., . . . Vasiljeva, O. (2011). Ferri-liposomes as an MRI-visible drug-delivery system for targeting tumours and their microenvironment. *Nat Nano*, *6*(9), 594-602. doi: <http://www.nature.com/nnano/journal/v6/n9/abs/nnano.2011.112.html#supplementary-information>
- Mirabello, V., Calatayud, D. G., Arrowsmith, R. L., Ge, H., & Pascu, S. I. (2015). Metallic nanoparticles as synthetic building blocks for cancer diagnostics: from materials design to molecular imaging applications. *Journal of Materials Chemistry B*, *3*(28), 5657-5672. doi: 10.1039/C5TB00841G
- Moezzi, A., McDonagh, A. M., & Cortie, M. B. (2012). Zinc oxide particles: Synthesis, properties and applications. *Chemical Engineering Journal*, *185-186*, 1-22. doi: <http://dx.doi.org/10.1016/j.cej.2012.01.076>
- Moghimi, S. M., Hunter, A. C., & Andresen, T. L. (2012). Factors Controlling Nanoparticle Pharmacokinetics: An Integrated Analysis and Perspective. *Annual Review of Pharmacology and Toxicology*, *52*(1), 481-503. doi: 10.1146/annurev-pharmtox-010611-134623
- Montalti, M., Prodi, L., Zaccheroni, N., Battistini, G., Marcuz, S., Mancin, F., . . . Tonellato, U. (2006). Size Effect on the Fluorescence Properties of Dansyl-Doped Silica Nanoparticles. *Langmuir*, *22*(13), 5877-5881. doi: 10.1021/la053473y
- Mosmann, T. (1983). Rapid colorimetric assay for cellular growth and survival: Application to proliferation and cytotoxicity assays. *Journal of Immunological Methods*, *65*(1-2), 55-63. doi: [http://dx.doi.org/10.1016/0022-1759\(83\)90303-4](http://dx.doi.org/10.1016/0022-1759(83)90303-4)

N

- Naahidi, S., Jafari, M., Edalat, F., Raymond, K., Khademhosseini, A., & Chen, P. (2013). Biocompatibility of engineered nanoparticles for drug delivery. *Journal of Controlled Release*, *166*(2), 182-194. doi: <http://dx.doi.org/10.1016/j.jconrel.2012.12.013>
- Nakamura, H., Liao, L., Hitaka, Y., Tsukigawa, K., Subr, V., Fang, J., . . . Maeda, H. (2013). Micelles of zinc protoporphyrin conjugated to N-(2-hydroxypropyl)methacrylamide (HPMA) copolymer for imaging and light-induced antitumor effects in vivo. *Journal of Controlled Release*, *165*(3), 191-198. doi: <http://dx.doi.org/10.1016/j.jconrel.2012.11.017>

Nassar, N. N., & Ringsred, A. (2012). Rapid Adsorption of Methylene Blue from Aqueous Solutions by Goethite Nanoadsorbents. *Environmental Engineering Science, 29*(8), 790-797. doi: 10.1089/ees.2011.0263

Noble, G. T., Stefanick, J. F., Ashley, J. D., Kiziltepe, T., & Bilgicer, B. (2014). Ligand-targeted liposome design: challenges and fundamental considerations. *Trends in Biotechnology, 32*(1), 32-45. doi: 10.1016/j.tibtech.2013.09.007

O

Ozpolat, B., Sood, A. K., & Lopez-Berestein, G. (2014). Liposomal siRNA nanocarriers for cancer therapy. *Advanced Drug Delivery Reviews, 66*, 110-116. doi: <http://dx.doi.org/10.1016/j.addr.2013.12.008>

Paszko, E., Ehrhardt, C., Senge, M. O., Kelleher, D. P., & Reynolds, J. V. (2011). Nanodrug applications in photodynamic therapy. *Photodiagnosis and Photodynamic Therapy, 8*(1), 14-29. doi: <http://dx.doi.org/10.1016/j.pdpdt.2010.12.001>

P

Patel, K., Sundara Raj, B., Chen, Y., & Lou, X. (2016). Cytotoxicity of folic acid conjugated hollow silica nanoparticles toward Caco-2 and 3T3 cells, with and without encapsulated DOX. *Colloids and Surfaces B: Biointerfaces, 140*, 213-222. doi: <http://dx.doi.org/10.1016/j.colsurfb.2015.12.046>

Patel, N. R., Pattni, B. S., Abouzeid, A. H., & Torchilin, V. P. (2013). Nanopreparations to overcome multidrug resistance in cancer. *Advanced Drug Delivery Reviews, 65*(13-14), 1748-1762. doi: <http://dx.doi.org/10.1016/j.addr.2013.08.004>

Paukner, S., Kohl, G., & Lubitz, W. (2004). Bacterial ghosts as novel advanced drug delivery systems: antiproliferative activity of loaded doxorubicin in human Caco-2 cells. *Journal of Controlled Release, 94*(1), 63-74. doi: <http://dx.doi.org/10.1016/j.jconrel.2003.09.010>

Peiris, P. M., Bauer, L., Toy, R., Tran, E., Pansky, J., Doolittle, E., . . . Karathanasis, E. (2012). Enhanced Delivery of Chemotherapy to Tumors Using a Multi-Component Nanochain with Radiofrequency-Tunable Drug Release. *ACS Nano, 6*(5), 4157-4168. doi: 10.1021/nn300652p

Pelaz, B., del Pino, P., Maffre, P., Hartmann, R., Gallego, M., Rivera-Fernández, S., . . . Parak, W. J. (2015). Surface Functionalization of Nanoparticles with Polyethylene Glycol: Effects on Protein Adsorption and Cellular Uptake. *ACS Nano, 9*(7), 6996-7008. doi: 10.1021/acsnano.5b01326

- Peng, J., Zhao, L., Zhu, X., Sun, Y., Feng, W., Gao, Y., Wang, L., Li, F. (2013) Hollow silica nanoparticles loaded with hydrophobic phthalocyanine for near-infrared photodynamic and photothermal combination therapy, *Biomaterials*, 34 (2013) 7905-7912
- Perez-Aso, M., Mediero, A., Low, Y. C., Levine, J., & Cronstein, B. N. (2015). Adenosine A2A receptor plays an important role in radiation-induced dermal injury. *The FASEB Journal*. doi: 10.1096/fj.15-280388
- Perry, J. L., Reuter, K. G., Kai, M. P., Herlihy, K. P., Jones, S. W., Luft, J. C., . . . DeSimone, J. M. (2012). PEGylated PRINT Nanoparticles: The Impact of PEG Density on Protein Binding, Macrophage Association, Biodistribution, and Pharmacokinetics. *Nano Letters*, 12(10), 5304-5310. doi: 10.1021/nl302638g
- Pertsin, A. J., & Grunze, M. (2000). Computer Simulation of Water near the Surface of Oligo(ethylene glycol)-Terminated Alkanethiol Self-Assembled Monolayers. *Langmuir*, 16(23), 8829-8841. doi: 10.1021/la000340y
- Pirollo, K. F., & Chang, E. H. (2008). Does a targeting ligand influence nanoparticle tumor localization or uptake? *Trends in Biotechnology*, 26(10), 552-558. doi: <http://dx.doi.org/10.1016/j.tibtech.2008.06.007>
- Pourfallah, G., & Lou, X. (2016). A novel recyclable magnetic nanostructure for highly sensitive, selective and reversible detection of zinc ions in aqueous solutions. *Sensors and Actuators B: Chemical*, 233, 379-387. doi: <http://dx.doi.org/10.1016/j.snb.2016.04.087>
- Prabhu RH, Patravale VB, & MD, J. (2015). Polymeric nanoparticles for targeted treatment in oncology: current insights. *International journal of nanomedicine*, 10, 1001-1018. doi: 10.2147/ijn.s56932

R

- Ramani, M., Ponnusamy, S., Muthamizhchelvan, C., Cullen, J., Krishnamurthy, S., & Marsili, E. (2013). Morphology-directed synthesis of ZnO nanostructures and their antibacterial activity. *Colloids and Surfaces B: Biointerfaces*, 105(0), 24-30. doi: <http://dx.doi.org/10.1016/j.colsurfb.2012.12.056>
- Revia, R. A., & Zhang, M. (2016). Magnetite nanoparticles for cancer diagnosis, treatment, and treatment monitoring: recent advances. *Materials Today*, 19(3), 157-168. doi: <http://dx.doi.org/10.1016/j.mattod.2015.08.022>
- Ritger, P. L., & Peppas, N. A. (1987). A simple equation for description of solute release I. Fickian and non-fickian release from non-swellable devices in the form of slabs, spheres, cylinders or discs. *Journal of Controlled Release*, 5(1), 23-36. doi: 10.1016/0168-3659(87)90034-4
- Robertson, C., Robertson, A. G., Hendry, J. H., Roberts, S. A., Slevin, N. J., Duncan, W. B., . . . Keane, T. J. (1998). Similar decreases in local tumor control are calculated for treatment protraction and for interruptions in the

radiotherapy of carcinoma of the larynx in four centers. *International Journal of Radiation Oncology • Biology • Physics*, 40(2), 319-329. doi: 10.1016/S0360-3016(97)00716-5

Ross, J. F., Chaudhuri, P. K., & Ratnam, M. (1994). Differential regulation of folate receptor isoforms in normal and malignant tissues in vivo and in established cell lines. Physiologic and clinical implications. *Cancer*, 73(9), 2432-2443. doi: 10.1002/1097-0142(19940501)73:9<2432::AID-CNCR2820730929>3.0.CO;2-S

Roy, R., Das, M., & Dwivedi, P. D. (2015). Toxicological mode of action of ZnO nanoparticles: Impact on immune cells. *Molecular Immunology*, 63(2), 184-192. doi: <http://dx.doi.org/10.1016/j.molimm.2014.08.001>

Ryan, J. L. (2012). Ionizing Radiation: The Good, the Bad, and the Ugly. *J Invest Dermatol*, 132(3), 985-993

S

Sahu, S. K., Mallick, S. K., Santra, S., Maiti, T. K., Ghosh, S. K., & Pramanik, P. (2010). In vitro evaluation of folic acid modified carboxymethyl chitosan nanoparticles loaded with doxorubicin for targeted delivery. *Journal of Materials Science : Materials in Medicine* 21(5), 1587-1597

Sailor, M. J., & Park, J.-H. (2012). Hybrid Nanoparticles for Detection and Treatment of Cancer. *Advanced Materials*, 24(28), 3779-3802. doi: 10.1002/adma.201200653

Salvo, N., Barnes, E., van Draanen, J., Stacey, E., Mitera, G., Breen, D., . . . De Angelis, C. (2010). Prophylaxis and management of acute radiation-induced skin reactions: a systematic review of the literature. *Current Oncology*, 17(4), 94-112

Sapsford, K. E., Algar, W. R., Berti, L., Gemmill, K. B., Casey, B. J., Oh, E., . . . Medintz, I. L. (2013). Functionalizing Nanoparticles with Biological Molecules: Developing Chemistries that Facilitate Nanotechnology. *Chemical Reviews*, 113(3), 1904-2074. doi: 10.1021/cr300143v

Saranya, M., Ramachandran, R., Samuel, E. J. J., Jeong, S. K., & Grace, A. N. (2015). Enhanced visible light photocatalytic reduction of organic pollutant and electrochemical properties of CuS catalyst. *Powder Technology*, 279, 209-220. doi: <http://dx.doi.org/10.1016/j.powtec.2015.03.041>

Sawyers, C. (2004). Targeted cancer therapy. *Nature*, 432(7015), 294-297

Schartl, W. (2010). Current directions in core-shell nanoparticle design. *Nanoscale*, 2(6), 829-843. doi: 10.1039/C0NR00028K

- Seelig, E. W., Tang, B., Yamilov, A., Cao, H., & Chang, R. P. H. (2003). Self-assembled 3D photonic crystals from ZnO colloidal spheres. *Materials Chemistry and Physics*, *80*(1), 257-263. doi: 10.1016/s0254-0584(02)00492-3
- Serpone, N., & Emeline, A. V. (2012). Semiconductor Photocatalysis — Past, Present, and Future Outlook. *The Journal of Physical Chemistry Letters*, *3*(5), 673-677. doi: 10.1021/jz300071j
- Sharma, H., Mishra, P. K., Talegaonkar, S., & Vaidya, B. (2015). Metal nanoparticles: a theranostic nanotool against cancer. *Drug Discovery Today*, *20*(9), 1143-1151. doi: <http://dx.doi.org/10.1016/j.drudis.2015.05.009>
- Shekofteh-Gohari, M., & Habibi-Yangjeh, A. (2015). Facile preparation of Fe₃O₄@AgBr-ZnO nanocomposites as novel magnetically separable visible-light-driven photocatalysts. *Ceramics International*, *41*(1, Part B), 1467-1476. doi: <http://dx.doi.org/10.1016/j.ceramint.2014.09.081>
- Shen, J., Song, G., An, M., Li, X., Wu, N., Ruan, K., . . . Hu, R. (2014). The use of hollow mesoporous silica nanospheres to encapsulate bortezomib and improve efficacy for non-small cell lung cancer therapy. *Biomaterials*, *35*(1), 316-326. doi: <http://dx.doi.org/10.1016/j.biomaterials.2013.09.098>
- Silveira, G. Q., da Silva, R. S., Franco, L. P., Vargas, M. D., & Ronconi, C. M. (2015). Redox-responsive nanoreservoirs: The effect of different types of mesoporous silica on the controlled release of doxorubicin in solution and in vitro. *Microporous and Mesoporous Materials*, *206*(0), 226-233. doi: <http://dx.doi.org/10.1016/j.micromeso.2014.12.026>
- Singh Dhakad, R., Kumar Tekade, R., & Kumar Jain, N. (2013). Cancer Targeting Potential of Folate Targeted Nanocarrier under Comparative Influence of Tretinoin and Dexamethasone. *Current Drug Delivery*, *10*(4), 477-491
- Sobczyński, J., Tønnesen, H. H., & Kristensen, S. (2013). Influence of aqueous media properties on aggregation and solubility of four structurally related mesoporphyrin photosensitizers evaluated by spectrophotometric measurements. *Die Pharmazie - An International Journal of Pharmaceutical Sciences*, *68*(2), 100-109. doi: 10.1691/ph.2013.2130
- Society, A. C. (2015). *Cancer Facts & Figures 2015*. Atlanta: American Cancer Society. Retrieved from American Cancer Society, Cancer Facts and Figures 2015.
- Song, E.-Q., Zhang, Z.-L., Luo, Q.-Y., Lu, W., Shi, Y.-B., & Pang, D.-W. (2009). Tumor Cell Targeting Using Folate-Conjugated Fluorescent Quantum Dots and Receptor-Mediated Endocytosis. *Clinical Chemistry*, *55*(5), 955-963. doi: 10.1373/clinchem.2008.113423
- Stöber, W., Fink, A., & Bohn, E. (1968). Controlled growth of monodisperse silica spheres in the micron size range. *Journal of Colloid and Interface Science*, *26*(1), 62-69. doi: 10.1016/0021-9797(68)90272-5

Suen, W.-L. L., & Chau, Y. (2014). Size-dependent internalisation of folate-decorated nanoparticles via the pathways of clathrin and caveolae-mediated endocytosis in ARPE-19 cells. *Journal of Pharmacy and Pharmacology*, *66*(4), 564-573. doi: 10.1111/jphp.12134

T

Tan, J. S., Butterfield, D. E., Voycheck, C. L., Caldwell, K. D., & Li, J. T. (1993). Surface modification of nanoparticles by PEO/PPO block copolymers to minimize interactions with blood components and prolong blood circulation in rats. *Biomaterials*, *14*(11), 823-833. doi: [http://dx.doi.org/10.1016/0142-9612\(93\)90004-L](http://dx.doi.org/10.1016/0142-9612(93)90004-L)

Tan, L., Liu, T., Li, L., Liu, H., Wu, X., Gao, F., . . . Tang, F. (2013). Uniform double-shelled silica hollow spheres: acid/base selective-etching synthesis and their drug delivery application. *RSC Advances*, *3*(16), 5649-5655. doi: 10.1039/C3RA40733K

Tan, Y. H., Goh, P. S., & Ismail, A. F. (2015). Development of photocatalytic coupled zinc-iron oxide nanoparticles via solution combustion for bisphenol-A removal. *International Biodeterioration & Biodegradation*, *102*, 346-352. doi: <http://dx.doi.org/10.1016/j.ibiod.2015.03.010>

Tannock, I. F. (1998). Conventional cancer therapy: promise broken or promise delayed? *The Lancet*, *351*, Supplement 2, SII9-SII16. doi: [http://dx.doi.org/10.1016/S0140-6736\(98\)90327-0](http://dx.doi.org/10.1016/S0140-6736(98)90327-0)

Tharmaraj, V., & Pitchumani, K. (2012). An acyclic, dansyl based colorimetric and fluorescent chemosensor for Hg(II) via twisted intramolecular charge transfer (TICT). *Analytica Chimica Acta*, *751*, 171-175. doi: <http://dx.doi.org/10.1016/j.aca.2012.09.016>

Torchilin, V. (2011). Tumor delivery of macromolecular drugs based on the EPR effect. *Advanced Drug Delivery Reviews*, *63*(3), 131-135. doi: <http://dx.doi.org/10.1016/j.addr.2010.03.011>

Toy, R., Peiris, P. M., Ghaghada, K. B., & Karathanasis, E. (2014). Shaping cancer nanomedicine: The effect of particle shape on the in vivo journey of nanoparticles. *Nanomedicine (London, England)*, *9*(1), 121-134. doi: 10.2217/nnm.13.191

Treuel, L., Brandholt, S., Maffre, P., Wiegele, S., Shang, L., & Nienhaus, G. U. (2014). Impact of Protein Modification on the Protein Corona on Nanoparticles and Nanoparticle-Cell Interactions. *ACS Nano*, *8*(1), 503-513. doi: 10.1021/nn405019v

Tyagi, A., & Penzkofer, A. (2010). Fluorescence spectroscopic behaviour of folic acid. *Chemical Physics*, *367*(2-3), 83-92. doi: <http://dx.doi.org/10.1016/j.chemphys.2009.10.026>

W

- Wagner, P., Hegner, M., Kernen, P., Zaugg, F., & Semenza, G. (1996). Covalent immobilization of native biomolecules onto Au(111) via N-hydroxysuccinimide ester functionalized self-assembled monolayers for scanning probe microscopy. *Biophysical Journal*, *70*(5), 2052-2066. doi: [http://dx.doi.org/10.1016/S0006-3495\(96\)79810-7](http://dx.doi.org/10.1016/S0006-3495(96)79810-7)
- Walkey, C. D., & Chan, W. C. W. (2012). Understanding and controlling the interaction of nanomaterials with proteins in a physiological environment. *Chemical Society Reviews*, *41*(7), 2780-2799. doi: 10.1039/C1CS15233E
- Walkey, C. D., Olsen, J. B., Guo, H., Emili, A., & Chan, W. C. W. (2012). Nanoparticle Size and Surface Chemistry Determine Serum Protein Adsorption and Macrophage Uptake. *Journal of the American Chemical Society*, *134*(4), 2139-2147. doi: 10.1021/ja2084338
- Wang, H., Zhang, L., Chen, Z., Hu, J., Li, S., Wang, Z., . . . Wang, X. (2014). Semiconductor heterojunction photocatalysts: design, construction, and photocatalytic performances. *Chemical Society Reviews*, *43*(15), 5234-5244. doi: 10.1039/C4CS00126E
- Wei, X., Wang, W., & Chen, K. (2013). ZnO:Er,Yb,Gd Particles Designed for Magnetic-Fluorescent Imaging and Near-Infrared Light Triggered Photodynamic Therapy. *The Journal of Physical Chemistry C*, *117*(45), 23716-23729. doi: 10.1021/jp4071696
- Weitman, S. D., Lark, R. H., Coney, L. R., Fort, D. W., Frasca, V., Zurawski, V. R., & Kamen, B. A. (1992). Distribution of the Folate Receptor GP38 in Normal and Malignant Cell Lines and Tissues. *Cancer Research*, *52*(12), 3396-3401
- Welfare, A. I. o. H. a. (2015). Australian Cancer Incidence and Mortality (ACIM) books: All cancers combined Vol. All cancers combined. Retrieved from <http://www.aihw.gov.au/acim-books/>
- Wong, A. D., Ye, M., Ulmschneider, M. B., & Searson, P. C. (2015). Quantitative Analysis of the Enhanced Permeation and Retention (EPR) Effect. *PLoS ONE*, *10*(5), e0123461. doi: 10.1371/journal.pone.0123461
- Wu, C.-H., Chang, H.-W., & Chern, J.-M. (2006). Basic dye decomposition kinetics in a photocatalytic slurry reactor. *Journal of Hazardous Materials*, *137*(1), 336-343. doi: <http://dx.doi.org/10.1016/j.jhazmat.2006.02.002>

X

- Xing, S., Zhou, Z., Ma, Z., & Wu, Y. (2011). Characterization and reactivity of Fe₃O₄/FeMnOx core/shell nanoparticles for methylene blue discoloration with H₂O₂. *Applied Catalysis B: Environmental*, *107*(3-4), 386-392. doi: <http://dx.doi.org/10.1016/j.apcatb.2011.08.002>

- Xiong, G., Pal, U., Serrano, J. G., Ucer, K. B., & Williams, R. T. (2006). Photoluminescence and FTIR study of ZnO nanoparticles: the impurity and defect perspective. *physica status solidi (c)*, 3(10), 3577-3581. doi: 10.1002/pssc.200672164
- Xu, P., Zeng, G. M., Huang, D. L., Feng, C. L., Hu, S., Zhao, M. H., . . . Liu, Z. F. (2012). Use of iron oxide nanomaterials in wastewater treatment: A review. *Science of The Total Environment*, 424, 1-10. doi: <http://dx.doi.org/10.1016/j.scitotenv.2012.02.023>
- Xu, Y.-N., & Ching, W. Y. (1993). Electronic, optical, and structural properties of some wurtzite crystals. *Physical Review B*, 48(7), 4335-4351
- Xuan, D., Sheng-Hua, X., Zhi-Wei, S., & Yan, A. (2010). Effect of the Hydrodynamic Radius of Colloid Microspheres on the Estimation of the Coagulation Rate Constant. *Acta Physico-Chimica Sinica*, 26(10), 2807-2812

Y

- Yang, Q., Jones, S. W., Parker, C. L., Zamboni, W. C., Bear, J. E., & Lai, S. K. (2014). Evading Immune Cell Uptake and Clearance Requires PEG Grafting at Densities Substantially Exceeding the Minimum for Brush Conformation. *Molecular Pharmaceutics*, 11(4), 1250-1258. doi: 10.1021/mp400703d
- Yang, Y., & Yu, C. (2016). Advances in silica based nanoparticles for targeted cancer therapy. *Nanomedicine: Nanotechnology, Biology and Medicine*, 12(2), 317-332. doi: <http://dx.doi.org/10.1016/j.nano.2015.10.018>
- Yarbro, C. H., Wujcik, D., & Gobe, B. H. (Eds.). (2010). *Cancer nursing : principles and practice* (7 ed.). Sudbury, MA, USA: Jones and Bartlett Publishers.
- Yu, Y., Duan, J., Li, Y., Yu, Y., Jin, M., Li, C., . . . Sun, Z. (2015). Combined toxicity of amorphous silica nanoparticles and methylmercury to human lung epithelial cells. *Ecotoxicology and Environmental Safety*, 112, 144-152. doi: <http://dx.doi.org/10.1016/j.ecoenv.2014.10.026>
- Yuan, Q., Hein, S., & Misra, R. D. K. (2010). New generation of chitosan-encapsulated ZnO quantum dots loaded with drug: Synthesis, characterization and in vitro drug delivery response. *Acta Biomaterialia*, 6(7), 2732-2739. doi: <http://dx.doi.org/10.1016/j.actbio.2010.01.025>

Z

- Zhang, H., Chen, B., Jiang, H., Wang, C., Wang, H., & Wang, X. (2011). A strategy for ZnO nanorod mediated multi-mode cancer treatment. *Biomaterials*, *32*(7), 1906-1914. doi: <http://dx.doi.org/10.1016/j.biomaterials.2010.11.027>
- Zhang, J., Rana, S., Srivastava, R. S., & Misra, R. D. K. (2008). On the chemical synthesis and drug delivery response of folate receptor-activated, polyethylene glycol-functionalized magnetite nanoparticles. *Acta Biomaterialia*, *4*(1), 40-48. doi: <http://dx.doi.org/10.1016/j.actbio.2007.06.006>
- Zhao, Z., Zhang, H., Chi, X., Li, H., Yin, Z., Huang, D., . . . Gao, J. (2014). Silica nanovehicles endow arsenic trioxide with an ability to effectively treat cancer cells and solid tumors. *Journal of Materials Chemistry B*, *2*(37), 6313-6323. doi: 10.1039/C4TB00874J
- Zhou, Z., Sun, Y., Shen, J., Wei, J., Yu, C., Kong, B., . . . Wang, W. (2014). Iron/iron oxide core/shell nanoparticles for magnetic targeting MRI and near-infrared photothermal therapy. *Biomaterials*, *35*(26), 7470-7478. doi: <http://dx.doi.org/10.1016/j.biomaterials.2014.04.063>
- Zödl, B., Zeiner, M., Sargazi, M., Roberts, N. B., Marktl, W., Steffan, I., & Ekmekcioglu, C. (2003). Toxic and biochemical effects of zinc in Caco-2 cells. *Journal of Inorganic Biochemistry*, *97*(4), 324-330. doi: [http://dx.doi.org/10.1016/S0162-0134\(03\)00312-X](http://dx.doi.org/10.1016/S0162-0134(03)00312-X)

Every reasonable effort has been made to acknowledge the owners of copyright material. I would be pleased to hear from any copyright owner who has been omitted or incorrectly acknowledged.

APPENDIX 1

Reproducibility of photodegradation experiments

Photodegradation experiments were conducted using a well-established method based on previously published work [1,2,3,4]. The reproducibility of the method was scrutinised in trial experiments using methylene blue (MB) at a concentration of 10 mg.L^{-1} . The results of trial experiments are displayed in Figure A2-1 below and clearly highlight the reliability of the method employed.

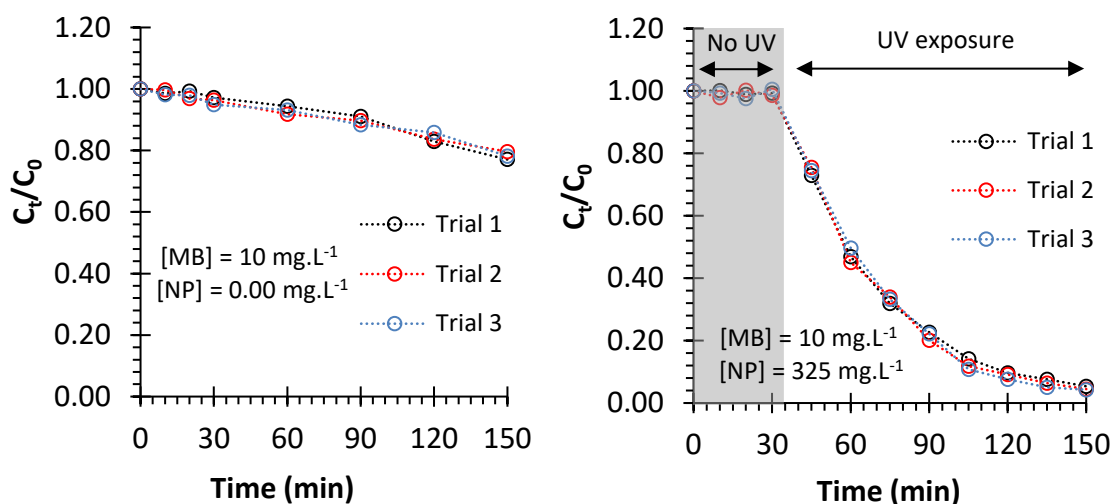


Figure A1-1. Photodegradation experimental trials highlighting the reproducibility of the employed method. Experiments were conducted 3 times with a MB concentration of 10 mg.L^{-1} and a FZ NP concentration of 0.00 mg.L^{-1} (left) and 325 mg.L^{-1} (right).

References

- [1] X. Feng, S. Zhang, X. Lou, Controlling silica coating thickness on TiO_2 nanoparticles for effective photodynamic therapy Colloids and Surfaces B: Biointerfaces, 107 (2013) 220-226.

- [2] X. Feng, S. Zhang, H. Wu, X. Lou, A novel folic acid-conjugated TiO₂-SiO₂ photosensitizer for cancer targeting in photodynamic therapy, *Colloids and Surfaces B: Biointerfaces*, 125 (2015) 197-205.
- [3] X. Feng, H. Guo, K. Patel, H. Zhou, X. Lou, High performance, recoverable Fe₃O₄-ZnO nanoparticles for enhanced photocatalytic degradation of phenol, *Chemical Engineering Journal*, 244 (2014) 327-334.
- [4] X. Feng, X. Lou, The effect of surfactants-bound magnetite (Fe₃O₄) on the photocatalytic properties of the heterogeneous magnetic zinc oxides nanoparticles, *Separation and Purification Technology*, 147 (2015) 266-275.

APPENDIX 2

The following pages contain documents outlining permission granted from copyright owners for use of third party copyright material or published work in which the copyright is held by another party.

Copyright agreement for Figure 1-1 in Chapter 1

ELSEVIER LICENSE TERMS AND CONDITIONS

Dec 07, 2016

This Agreement between Kunal Patel ("You") and Elsevier ("Elsevier") consists of your license details and the terms and conditions provided by Elsevier and Copyright Clearance Center.

License Number	4003980469016
License date	Dec 07, 2016
Licensed Content Publisher	Elsevier
Licensed Content Publication	Trends in Biotechnology
Licensed Content Title	Ligand-targeted liposome design: challenges and fundamental considerations
Licensed Content Author	Gavin T. Noble, Jared F. Stefanick, Jonathan D. Ashley, Tanyel Kiziltepe, Basar Bilgicer
Licensed Content Date	January 2014
Licensed Content Volume Number	32
Licensed Content Issue Number	1
Licensed Content Pages	14
Start Page	32
End Page	45
Type of Use	reuse in a thesis/dissertation
Portion	figures/tables/illustrations
Number of figures/tables/illustrations	1
Format	both print and electronic
Are you the author of this Elsevier article?	No
Will you be translating?	No
Order reference number	
Original figure numbers	Figure 1
Title of your thesis/dissertation	Synthesis and Evaluation of Novel Core-Shell Nanostructured Metal Oxides for Cancer Targeting
Expected completion date	Dec 2016
Estimated size (number of pages)	180
Elsevier VAT number	GB 494 6272 12
Requestor Location	Kunal Patel 3 Mina court Duncraig, 6023 Australia Attn: Kunal Patel
Total	0.00 AUD
Terms and Conditions	

Copyright agreement for Chapter 2

ELSEVIER LICENSE TERMS AND CONDITIONS

Dec 05, 2016

This Agreement between Kunal Patel ("You") and Elsevier ("Elsevier") consists of your license details and the terms and conditions provided by Elsevier and Copyright Clearance Center.

License Number	4002390869517
License date	Dec 05, 2016
Licensed Content Publisher	Elsevier
Licensed Content Publication	Colloids and Surfaces B: Biointerfaces
Licensed Content Title	Cytotoxicity of folic acid conjugated hollow silica nanoparticles toward Caco2 and 3T3 cells, with and without encapsulated DOX
Licensed Content Author	Kunal Patel,Behin Sundara Raj,Yan Chen,Xia Lou
Licensed Content Date	1 April 2016
Licensed Content Volume Number	140
Licensed Content Issue Number	n/a
Licensed Content Pages	10
Start Page	213
End Page	222
Type of Use	reuse in a thesis/dissertation
Portion	full article
Format	both print and electronic
Are you the author of this Elsevier article?	Yes
Will you be translating?	No
Order reference number	
Title of your thesis/dissertation	Synthesis and Evaluation of Novel Core-Shell Nanostructured Metal Oxides for Cancer Targeting
Expected completion date	Dec 2016
Estimated size (number of pages)	180
Elsevier VAT number	GB 494 6272 12
Requestor Location	Kunal Patel 3 Mina court Duncraig, 6023 Australia Attn: Kunal Patel
Total	0.00 AUD
Terms and Conditions	

Copyright agreement for Chapter 3

ELSEVIER LICENSE TERMS AND CONDITIONS

Dec 12, 2016

This Agreement between Kunal Patel ("You") and Elsevier ("Elsevier") consists of your license details and the terms and conditions provided by Elsevier and Copyright Clearance Center.

The publisher has provided special terms related to this request that can be found at the end of the Publisher's Terms and Conditions.

License Number	4006520651818
License date	Dec 05, 2016
Licensed Content Publisher	Elsevier
Licensed Content Publication	Colloids and Surfaces B: Biointerfaces
Licensed Content Title	Novel folic acid conjugated Fe ₃ O ₄ -ZnO hybrid nanoparticles for targeted photodynamic therapy
Licensed Content Author	Kunal Patel,Behin Sundara Raj,Yan Chen,Xia Lou
Licensed Content Date	Available online 29 October 2016
Licensed Content Volume Number	n/a
Licensed Content Issue Number	n/a
Licensed Content Pages	1
Start Page	
End Page	
Type of Use	reuse in a thesis/dissertation
Intended publisher of new work	other
Portion	full article
Format	both print and electronic
Are you the author of this Elsevier article?	Yes
Will you be translating?	No
Order reference number	
Title of your thesis/dissertation	Synthesis and Evaluation of Novel Core-Shell Nanostructured Metal Oxides for Cancer Targeting
Expected completion date	Dec 2016
Estimated size (number of pages)	180
Elsevier VAT number	GB 494 6272 12
Requestor Location	Kunal Patel 3 Mina court Duncraig, 6023 Australia